STUDY ON TEMPORAL GROWTH AND LUMINESCENCE PROPERTIES OF ZnO NANOSTRUCTURES

Thesis Submitted in fulfilment of the requirements for the degree of

DOCTOR OF PHILOSOPHY

BY

PRIYANKA SHARMA

(Enrollment no: 186909)

Under the supervision of

Prof. (Dr.) P.B. Barman & Dr. Sanjiv Kumar Tiwari

DEPARTMENT OF PHYSICS AND MATERIALS SCIENCE
JAYPEE UNIVERSITY OF INFORMATION TECHNOLOGY
WAKNAGHAT, SOLAN, HP-173234, INDIA
APRIL 2024

TABLE OF CONTENTS

JAYPEE UNIVERSITY OF INFORMATION TECHNOLOGY
(Established by H.P. state Legislative vide Act No. 14 of 2002)
Waknaghat, P.O. Dumehar Bani, Kandaghat, Distt. Solan-173234 (H.P.) INDIA
Website: www.juit.ac.in
Phone No. (91) 07192-257999 (30 Lines)
Fax: (91) 01792 245362

DECLARATION

I hereby declare that the work reported in the Ph.D. thesis entitled **"Study on Temporal Growth and Luminescence Properties of ZnO Nanostructures"** submitted at **Jaypee University of Information Technology, Waknaghat, Solan, Himachal Pradesh, India** is an authentic record of my work carried out under the supervision of **Prof. Partha Bir Barman** and **Dr. Sanjiv Kumar Tiwari**. I have not submitted this work elsewhere for any other degree or diploma. I am fully responsible for the contents of my Ph.D. thesis.

(Priyanka Sharma)
Enrollment No. 186909
Department of Physics and Materials Science
Jaypee University of Information Technology
Waknaghat, Solan, H.P. India-173234

JAYPEE UNIVERSITY OF INFORMATION TECHNOLOGY
(Established by H.P. state Legislative vide Act No. 14 of 2002)
Waknaghat, P.O. Dumehar Bani, Kandaghat, Distt. Solan-173234 (H.P.) INDIA
Website: www.juit.ac.in
Phone No. (91) 07192-257999 (30 Lines)
Fax: (91) 01792 245362

CERTIFICATE

This is to certify that the work reported in the Ph.D. thesis entitled "**Study on Temporal Growth and Luminescence Properties of ZnO Nanostructures**", submitted by **Ms. Priyanka Sharma** at **Jaypee University of Information Technology, Waknaghat**, **Solan (HP) India,** is a bonafide record of her original work carried out under our supervision. This work has not been submitted elsewhere for any other degree or diploma.

(Prof. Partha Bir Barman)
Supervisor 1
Department of Physics and Materials Science
Jaypee University of Information Technology
Waknaghat, Solan, H.P. India-173234
Date……

(Dr. Sanjiv Kumar Tiwari)
Supervisor 2
Department of Physics and Materials Science
Jaypee University of Information Technology
Waknaghat, Solan, H.P. India-173234
Date……

Dedicated to my beloved family

Acknowledgement

"*Karmanye Vadhikaraste Ma Phaleshu Kadachana"*- Bhagavad Gita

This shloka which means "You have a right to perform your prescribed duty, but you are not entitled to the fruits of action" has been my guiding principle throughout my academic journey and I firmly believe that with Lord Krishna's blessings, I have been able to achieve what I have today. I am thankful to Lord Krishna for guiding me through the ups and downs of life and helping me stay true to my path. His blessings have been a constant source of strength and inspiration for me.

I am deeply thankful to my family, who has provided me with unconditional love, unwavering support and constant encouragement. Their sacrifices, guidance and wisdom have been the cornerstone of my success, and I am truly blessed to have them in my life.

Success is never achieved alone, and the completion of this Ph.D. thesis would not have been possible without the support, guidance, and assistance of many individuals who stood by me through my journey. I extend my sincere gratitude to each and every one of them for their invaluable contributions.

I pay my sincere thanks to **Mr. Jai Prakash Gaur** (JUIT Founder), JUIT administration, **Prof. (Dr.) Rajendra Kumar Sharma** (Vice Chancellor), **Prof. (Dr.) Ashok Kumar Gupta** (Dean Academics and research) and **Maj. Gen. Rakesh Bassi** (Registrar) for providing essential amenities, research funding and infrastructure for pursuing the research work.

I feel great serenity to express my highest venerations and heartfelt gratitude to my contemplative, prudent and dignified research supervisors, **Prof. Dr. Partha Bir Barman** and **Dr. Sanjiv Kumar Tiwari,** Department of Physics and Materials Science, Jaypee University of Information Technology, Waknaghat, Solan, Himachal Pradesh, India for giving me the opportunity to do research, providing invaluable guidance and freely sharing his knowledge, experience and valuable time for all my endeavors. Their dynamism, vision, sincerity and motivation have deeply inspired me. It was a great privilege and honour to work and study under their guidance. Their invaluable and benevolent guidance with untiring willingness to help, council, and encouragement at very juncture made me complete my work. I will always remain indebted to them for their selfless persuasion and my thesis could not have been completed without their

guidance and support. I also express my deep sense of gratitude towards my DPMC members **Prof. Dr. Vineet Sharma**, **Dr. Surajit Kumar Hazra** and **Dr. R.S. Raja Durai** for their precious suggestions, encouragement and constant support in entire work.

I would also like to extend my gratitude to **Prof. Dr. Partha Bir Barman,** Head Department of Physics and Materials Science for his continuous support and motivation to accomplish current work. I also would like to thank the faculty members of the department **Prof. Dr. Sunil Kumar Khah, Prof. Dr. Vineet Sharma**, **Dr. Ragini Raj Singh**, **Dr. Surajit Kumar Hazra and Dr. Santu Baidya** for their constant motivation and moral support throughout my doctoral journey. I will always appreciate the help I got from our technical and non-technical staff. I am thankful to **Sh. Kamlesh Kumar Mishra**, **Sh. Ravendra Kumar Tiwari, Mr. Baleshwar Shukla**, **Mr. Deepak Kumar, Mr. Ghanshyam, Sh. Mohan Sharma** for valuable contributions in my research period.

My acknowledgement would never be complete without the special mention of my seniors **Dr. Jonny Dhiman, Dr. Deepak Sharma**, **Dr. Prashant Thakur, Dr. Rohit Sharma, Dr. Pooja, Dr. Shammi Rana, Nidhi Sharma,** and **Dr. Kanchan Kumari** for their encouragement and help during the work. Friends are true gems in life that are always there for you in your best and toughest situations. A special thanks to my crazy friends **Sakshi Beri, Achyut Sharma, Dr. Atul Kumar, Kartik Mishra, Anuradha, Shivali Sharma, Sweta, Kalpana, Shivani Thakur, Neha Thakur, Sakshi, Dr. Sanjay Kumar, Rahul Singh, Shikha Sinha, Raj Kumar Prashar, Dr. Prachi Vasistha, Dr. Shiv Kumar, Jyoti Thakur, Dr. Ashwani Kumar, Vishakha and Anjna** who have refreshed and handled my mood swings during the course of study.

I feel a deep sense of gratitude from the core of my heart towards my parents **Mr. Vidya Sagar Sharma, Mrs. Shakuntla Sharma** and to my younger brother **Adv. Ved Bhushan Sharma** for their unconditional love, support and encouragement throughout my academic pursuits.

I am also thankful and respectful towards the individuals not mentioned here for their valued contribution to my journey.

Priyanka Sharma

ABSTRACT

Zinc Oxide (ZnO) has attracted significant attention due to its unique characteristics and promising potential in various fields such as photo-detectors, sensors, LEDs and solar cells *etc*. Optically, ZnO NWs are highly desirable due to their wide energy band gap (approximately 3.27 eV) and large exciton binding energy (approximately 60 meV) at room temperature. These properties, along with their high surface-to-volume ratio, make ZnO NWs ideal for use in optoelectronics. Additionally, its non-toxicity, bio-compatibility and variety of synthesis methods make it more attractive. The objective of this study is to examine the growth and aging of ZnO nanoparticles, as well as the influence of the chemical environment on these phenomena. Additionally, the study explores the correlation between growth duration and temperature and their impact on the optical characteristics of nanowires (NWs).

The scientific community has extensively documented the study of the temporal growth and aging of nanoparticles, with numerous experimental and theoretical models available. However, these studies often necessitate the use of intricate equipment, highlighting the importance of proper handling. In this study, we employed a simple chemical approach to synthesize colloidal nanoparticles (NPs) and examined their temporal growth and aging in the growth solution using experimental and theoretical models. Our experimental procedures involved UV-vis and TEM spectroscopy techniques to investigate the in situ growth of NPs. The results from both methods demonstrate that nucleation occurs within 2 minutes in the growth solution, followed by the growth of particles. Additionally, we also studied atomically balanced and unbalanced precursors and discovered that atomically balanced reactions lead to the growth and aging of NPs, while atomically unbalanced reactions result in the decoupling of growth due to the presence of excess Zn environment around ZnO nuclei. Subsequently, we understood and modelled the growth of NPs using a phase field model (PFM) for different sets of parameters at various time steps.

In addition, we investigated the impact of temperature variations on the morphological and optical properties of ZnO nanowires. Our results indicate that even small changes in growth temperature can result in significant modifications in the morphology of ZnO nanostructures. For instance, a growth temperature of 70°C produced non-uniform structures, while broken and hollow tips of NWs were achieved at a temperature of 120°C, and the formation of hexagonal

NWs was observed at 90°C. We also discovered that changes in morphology or growth temperature can alter the optical band gap, while still leading to the same number of defect states at the same energy position within the band gap. Despite the same defect energy states at the same energy position, they show a shift in their NBE emission peak.

Following the optimization of the growth temperature, we studied the impact of growth time. Our findings indicate that perfect hexagonal nanowires were obtained at 90°C for up to 20 hours, after which the cross-section of the nanowires began to show modifications from hexagonal to cylindrical. Additionally, we observed bright boundaries of the nanowires and identified the reason for their presence by recording their EDX spectra. The growth time at a specific growth temperature had a negligible effect on the optical band gap, differing from the effect of growth temperature, but demonstrated a significant effect on the NBE emission peak in PL-emission spectra. Despite this, all the defect states remained pinned. Therefore, in conclusion, our study highlights the significant impact of growth temperature and time on the morphological and optical properties of ZnO nanowires along with the temporal growth and aging study of colloidal NPs.

LIST OF UNITS, SYMBOLS & ABBREVIATIONS

ZnO	Zinc Oxide
°C	Degree Celsius
NPs	Nanoparticles
NWs	Nanowires
NSs	Nanostructures
NTs	Nanotubes
RT	Room Temperature
SAXS	Small Angle X-Ray Scattering
WAXS	Wide Angle X-Ray Scattering
FESEM	Field Emission Scanning electron microscopy
TEM	Transmission electron microscopy
UV-vis	Ultraviolet-visible spectroscopy
PL	Photoluminescence spectroscopy
XRD	X-ray diffraction
mg	Milligrams
ml	Milliliter
mM	Millimolar
min	Minutes
nm	Nanometer
EDX	Energy dispersive X-Ray

LIST OF FIGURES

LIST OF TABLES

CHAPTER 1

INTRODUCTION

1.1 NANOTECHNOLOGY

Nanotechnology refers to the scientific and engineering discipline that deals with the synthesis, manipulation and modification of materials at the nanoscale level. The prefix "nano" denotes a scale of one billionth of a meter (10^{-9} m), and so nanotechnology deals with materials that possess a dimension ranging from 1 to 100 nanometers. In addition to this, the size at which the properties of materials start differing from the bulk one can be called as nanomaterials. For example, a material with a dimension of 350 nm can also be classified as a nanomaterial if its properties differ from those of its bulk counterpart at that very size value.

In 1958, physicist Richard Feynman presented a lecture titled "There's Plenty of Room at the Bottom," in which he introduced the concept of nanotechnology. He explored the potential for manipulating and organizing individual atoms and molecules to produce novel materials and devices. Since then, the field of nanotechnology has advanced significantly and has numerous applications in medicine, electronics, energy and other areas [1]. Further, the term "nanotechnology" was first coined by the renowned scientist Professor Norio Taniguchi in 1981. Moreover, the invention of scanning tunneling microscope (STM) in 1981 enables the visibility of atoms and molecules in the materials.

Nanotechnology relies heavily on nanomaterials, which possess desirable features such as high surface area, distinctive optical, electronic and mechanical properties, and their potential for functionalization. These characteristics render nanomaterials appealing for various applications. There are variety of semiconductor nanomaterials such as ZnO, GaN, CdS, TiO_2, ZnS *etc.* [2]. Their structural, electronic and elastic properties were successfully discussed by Hanada and by many others [3]. Among all, ZnO is found to be more attractive due to its distinctive properties *viz*.

a) Broad energy band gap (~3.37eV).
b) High exciton binding energy of around ~ 60 meV.
c) Property of synthesizing in a diverse range of nanostructures, such as nanosheets, nanowires (NWs), nanorods (NRs), nanotubes (NTs), nanoflowers, nanocombs, nanobelts, nano rings and nano plates *etc.* [4][5].

d) ZnO is piezoelectric and pyro electric in nature due to its non-centrosymmetry crystal structure.

Then, these properties makes ZnO highly attractive option for various optoelectronic applications, such as AFM tip, FETs, LEDs, solar cells and energy harvesting devices [6]–[9].

1.2 ZINC OXIDE (ZnO)

Zinc oxide (ZnO) belongs to the II-VI group of n-type compound semiconductors and has numerous applications in the field of optoelectronics. Among various existing semiconductor materials, zinc oxide (ZnO) has attracted a special attention from last three decades [10]. Despite that, ZnO has a wide range of applications, ranging from cosmetics to the fabrication of electrical devices, including photo voltaic, photo detectors, sensors, LEDs, solar cells, and devices that required good transport properties of electrons [11]. The main reason for their extensive use lies in its abundant availability, easy and low cost synthesis, bio compatibility and non-toxic nature as cumulated in Figure 1.1. Nowadays, various exciting nanostructures (NSs) of ZnO such as nanowires (NWs), nanorods (NRs), nanotubes (NTs), nanoflowers (NFs), nanoflakes (NFs) and nanocombs (NCs) *etc.* are well known and have application in various optoelectronic device fabrications. From all the listed nanostructures (NSs), researchers have their special interest on 1-D NSs such as NRs, NWs because of their superior charge collection and transport properties [12]. The high surface to volume ratio, non-toxic nature, easy synthesis and bio-compatibility of the 1-D ZnO makes it more attractive. Furthermore, ZnO is a piezoelectric in nature due to its non-centrosymmetric structure and due to this it has wide applications in the piezoelectric sensors and mechanical actuators [13], [14]. Despite being a topic of discussion for years, there are still numerous unexplained phenomena. One such example is the shifts observed in absorbance and emission spectra within the bulk regime. Thus, this study aims to examine ZnO nanoparticles (NPs) and nanowires (NWs) with diameters larger than their quantum regime to ensure consistency and gain a better understanding of these phenomena.

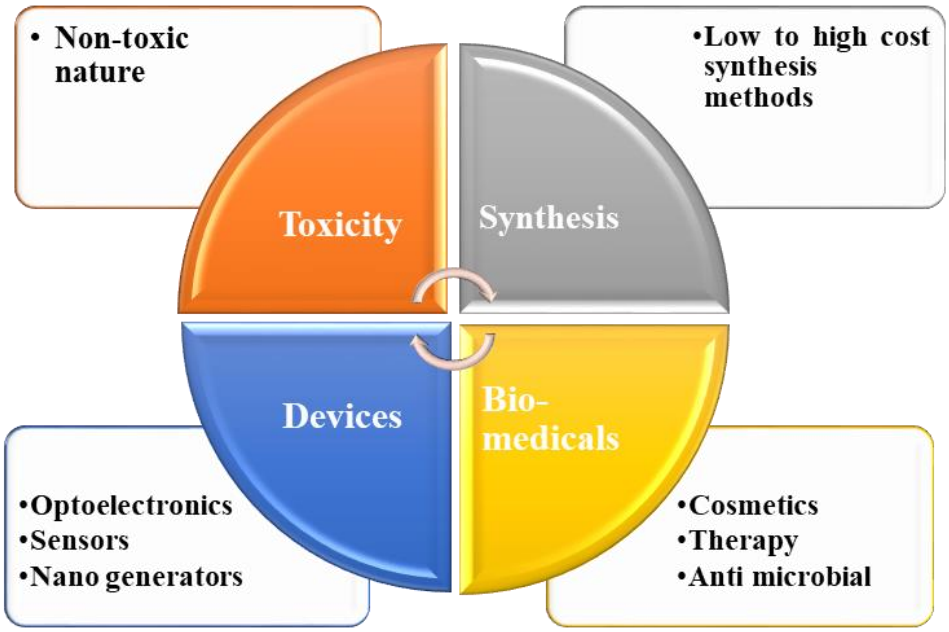

Figure 1.1: Zinc Oxide: Properties and Applications.

1.3 BAND STRUCTURE OF ZINC OXIDE (ZnO)

Figure 1.2 illustrates the electronic band structure of ZnO NWs and NPs, which was determined using a density functional theory approach [15], [16]. ZnO has direct band gap, as seen from its electronic band structure *i.e.* valance band maxima and conduction band minima occurs at the same value of *'k'* for both NWs and NPs. The literature indicates that the band gap energy of Zinc Oxide Nanowires (ZnO NWs) is slightly lower (3.26 eV) than that of nanoparticles (3.37 eV) [17]. The lower band gap energy in ZnO NWs is due to the relaxed structure that is generated during the calculation of the electronic structure in the theoretical treatment. This structure reveals that the surface atoms of ZnO NWs contract inwards in the x-y plane, resulting in a decreased distance between the center and the outermost atom. This decrease causes an increase in repulsion along the z-direction, ultimately leading to a decrease in the band gap energy of the ZnO NWs [18], [19].

Nowadays, there are various theories that describe the energy band diagram of ZnO such as LDA, LDA+U, GGA, greens functional method and first principles *etc.* [20], [21]. These theories were developed to provide the accurate values of the band gap. The significance of calculating the band structure provides us the information of various parameters such as: band gap, lattice parameters, electron-hole masses, bulk modulus and elastic tensor of the materials *etc*. There are numerous

experimental methods to find the energy band structure of the materials such as: photo-emission spectroscopy, LEED and X-ray induced photo absorption *etc*. To find the correct value of band gap from the theoretical models are still a big issue.

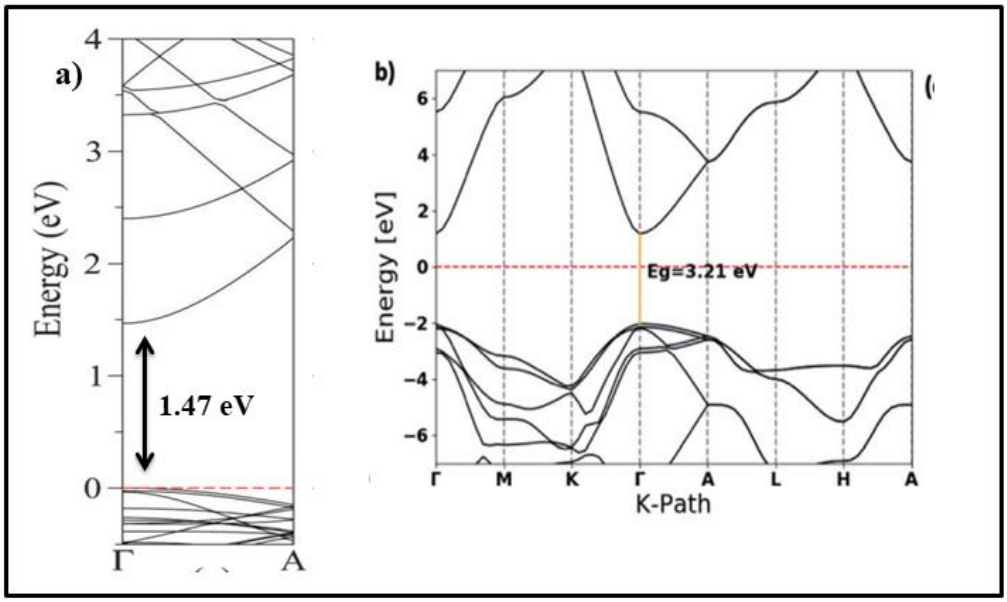

Figure 1.2: The electronic band structure of ZnO (a) nanowires and (b) nanoparticles [15], [16].

1.4 SYNTHESIS METHODS

1.4.1 Synthesis methods for ZnO NWs/ NRs

There are several ways to synthesize ZnO NWs/NRs on the variety of substrates [22]. To grow NWs/NRs, the initial stage always involves the preparation of nucleus centers (nanoseeds) on the substrate, followed by the growth of NWs/NRs. The seed layer is composed of a uniform coating of ZnO NPs on the substrate, which can be produced using the sol-gel method [23], magnetron sputter deposition [24] or thermal decomposition of Zinc Acetate in Ethanol [25]. The aim of this layer is to act as a site for nucleation and facilitate the growth of NWs/NRs. The second step is to grow NWs/NRs on the seeded layer. As depicted in Figure 1.3, various techniques for growing NWs on the seed layer have been documented in the literature. These techniques can primarily be

divided into two categories: vapour phase and chemical phase synthesis techniques. Vapour phase synthesis technique leads to the growth of NWs in closed chambers maintained at high temperatures whereas chemical phase synthesis leads the growth at low temperature conditions. Vapour phase deposition techniques involves the Physical vapour deposition (PVD) [26], Chemical vapour deposition (CVD), Pulsed laser deposition (PLD) [27], Plasma assisted thermal evaporation [23] Molecular beam Epitaxy (MBE), Template assisted growth [28] and Vapour liquid solid (VLS) *etc*. whereas chemical phase technique consists the solution based methods, sol gel methods and hydrothermal methods[29], [30], [31]. Below is a brief description of the provided methods:

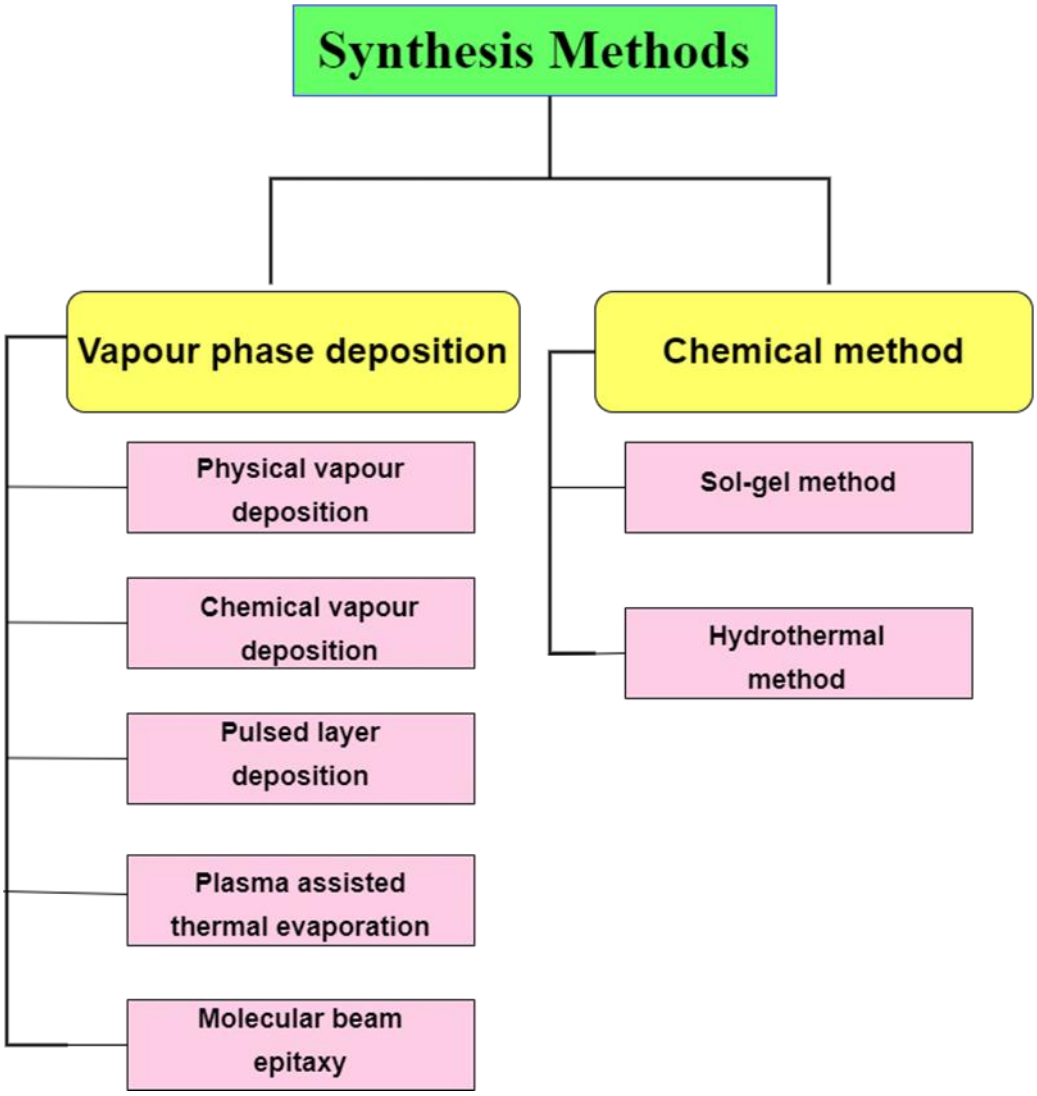

Figure 1.3: Synthesis methods for ZnO NWs.

(i) Physical vapour deposition (PVD)

Physical Vapour Deposition (PVD) is a method used for growing nanostructures that is based on the Vapour Solid (VS) growth mechanism. In this method, source materials can be sublimated without the use of any catalyst. PVD includes several techniques, such as thermal evaporation, Rf-magnetron sputtering, ion plating and electron beam evaporation, all of which involve depositing a thin film on a substrate at high deposition temperatures and under vacuum conditions. During PVD, argon gas is commonly used as a sputter gas and a mixture of oxygen and argon is used as the carrier gas at optimized ratios [32]. The PVD technique is particularly useful for preparing pure ZnO NWs without using any catalyst [32]–[34]. One significant advantage of PVD is its ability to provide a high level of control over the deposition process. This control enabling precise adjustment of the size, shape and orientation of the nanostructures.

(ii) Chemical vapour deposition (CVD)

Chemical vapour deposition (CVD) technique is preferable to prepare high quality 1-D NRs/NWs on the substrate. In this method, a constant flow of carrier gas (Argon + Oxygen) is used to grow ZnO nanowires in a chamber. Some studies in the literature have used gold catalysts to grow ZnO NWs [35]–[37], while others have reported growth without the use of any catalyst [38], [39]. This technique allows for precise control of the shape and size of the ZnO NWs, and it follows the Vapour Liquid Solid (VLS) mechanism for growth. Here the reactants are present in the vapour phase so it is quite easy to organize and rearrange the obtained NSs [40]. This technique requires high growth temperature (> 500ºC) along with constant carrier gas flow to produce less contaminated products with well aligned morphologies. Li et al. discussed the synthesis of ZnO 1D NSs using catalyst such as gold and copper metals [31]. It was concluded that the choice of catalyst affects the properties of the synthesized products. Additionally, this method can be used to synthesize vertically aligned [36]–[38] and doped NWs [41][12].

(iii) Pulsed laser deposition (PLD)

This is widely used technique for the deposition of various NSs thin films without the requirement of any metal catalysts. The process involves high-energy pulsed laser to ablate a rotating target material and deposit it onto a substrate maintained at a high temperature, under low base pressure

(10^{-7} Torr). The mechanism lying behind this is the photon interaction to the matter to generate the plume (contains ions, atoms and molecules). According to literature reports, the growth of ZnO nanowires (NWs) can only occur after the deposition of a thin layer of ZnO, which serves as the nucleation center for the subsequent NW growth [27], [42], [43]. Choopun et al. deposited the vertically aligned ZnO NRs in presence of argon gas environments [44]. Additionally, the literature reports on the impact of background pressure and temperature on the growth and characteristics of ZnO nanowires [45].

(iv) Molecular beam Epitaxy

The process of depositing high quality single crystals can also be achieved through an epitaxy method. This method involves the deposition of thin films in an ultra-high vacuum (UHV) environment, typically between 10^{-8} to 10^{-9} Torr. There are number of studies are reported in the literature on the synthesis of ZnO NWs by using MBE technique. Heo et al. employed a site-selected molecular beam epitaxy technique to deposit pure single crystalline ZnO NWs, which are applicable for solar-blind UV detection applications [46]. Another approach to growing site-specific ZnO NWs is through catalyst-driven molecular beam epitaxy [47]. Catalyst such as gold can be used in synthesis of ZnO and ZnMgO NWs on the Silion substrate [48]. Additionally, electron beam sputtering and magnetron sputtering can also utilized for sample preparation [49] [50] [51].

(v) Hydrothermal method

A low-cost and straightforward technique for large-scale production of various nanostructures (NSs) such as nanowires (NWs), nanotubes (NTs), and hollow nanospheres at low temperatures is the hydrothermal method, which is known for its reliability. The term “hydrothermal” means the geology and initially this terminology was used to study the formation of minerals and rocks in mid-19^{th} century, but later this was started using for the growth of single crystalline NSs. This method involves the aqueous solution in a closed vessel for the growth of different NSs. In this method high temperature and pressure is maintained in the growth solution via heating the solution to the optimized value. This condition in this method is necessary to have control on the final morphology of the growing species. This kind of synthesis method is important for regulating the composition of the synthesized materials. To facilitate the growth of ZnO NWs, two separate

solutions, each containing an aqueous solution of either zinc nitrate or hexamethylenetetramine in vessel was prepared. There are various factors that can affect the morphology, dimensions and growth rate of the synthesized NWs/NRs such as pH, temperature, reactants concentration, growth time, stirring rate and position of seeded substrate in the growth solution *etc.* [52]. Nanowires with desired morphology and dimensions can be easily prepared by this method even at under low temperature conditions as compared to other reported methods [40][44].

To fully comprehend the behavior of NSs in a growth solution, it is necessary to conduct extensive research on their formation, including the processes of nucleation, growth and aging. Understanding these mechanisms is of utmost importance to ensure the desired outcomes from the synthesis. Consequently, in the following section, an investigation into the nucleation and growth models has been conducted in detail.

1.5 NUCLEATION, GROWTH AND AGING MODELS

The study of the nucleation, growth and aging process has been an ongoing topic of research in current years. Numerous theories have been proposed by scientists and researchers to better understand and explain these processes. Thus in this section, brief introduction to the various existing theories is being discussed. Nucleation, growth and aging models can be explained as described in the flow chart in Figure 1.4.

1.5.1 Significance of study nucleation and growth

Nucleation and growth helps us to understand how new phases or nanostructures form, and how they grow and evolve over time. This information is useful in fields such as crystal growth, protein folding and in the formation of atmospheric clouds and nanoparticles, among others. The various theoretical as well as experimental models that explain the nucleation, growth and aging are listed below:

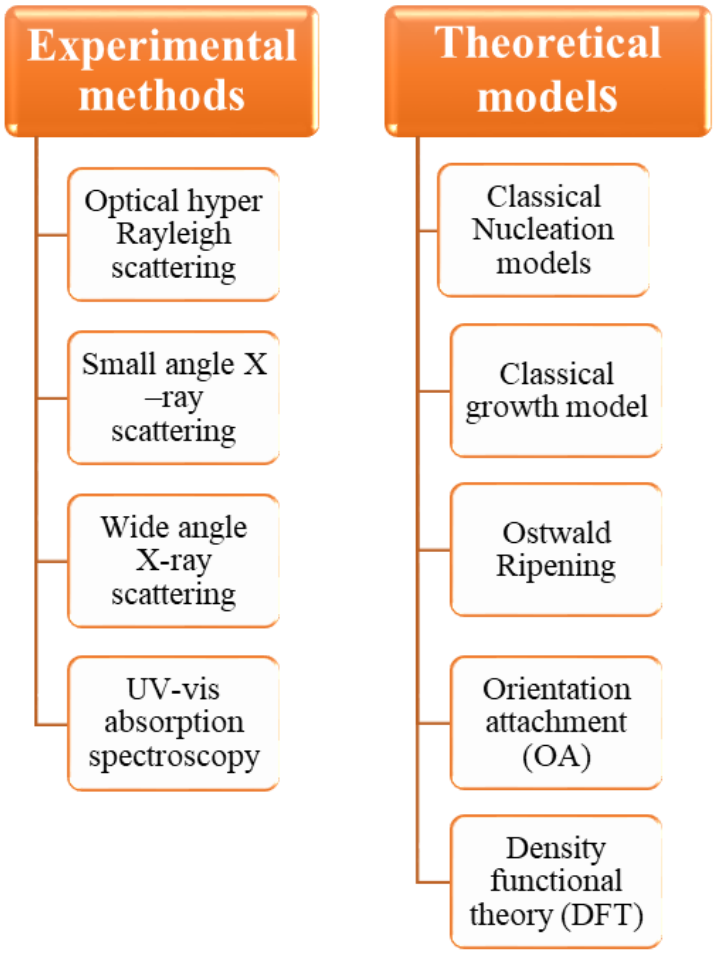

Figure 1.4: Classification of experimental and theoretical models of nucleation, growth and aging.

1.5.2 THEORETICAL MODELS

1.5.2.1 Classical model

The most widely used theoretical model for investigating nucleation kinetics is classical nucleation theory. This was widely accepted model for explaining the formation of new thermodynamic phases such as solids or liquids. [53]. This theory comes into existence about 90 years ago and successfully explains the nucleation process for many solutions. This theory based on the principle of super saturation of the growth solution. The supersaturated solution leads to the formation of small nuclei, which achieve the critical size and favors the further growth of nuclei. This theory is

based on the approximate reasons of the nucleation rates of new phases. The classical nucleation and growth models are briefly described below:

(i) Classical nucleation model

The term "nucleation" refers to the formation of thermodynamically stable phase, which further has tendency to grow into large sized particle within the parent supersaturated solution. This theory consists the formation of nucleus by two ways - homogeneous and heterogeneous nucleation. Homogeneous nucleation represents the occurrence of thermodynamically new stable phase from the supersaturated solution of same phase whereas the heterogeneous nucleation represents the occurrence of phase at the surface of foreign particles such as walls of container, impurities and grain boundaries *etc*. It is very fast and easy occurring nucleation because of the availability of stable nucleating surface. Super saturation of the solutions affects the nucleation rates to a larger extent. In the literature, Ludi et al. outlined the classical nucleation and progression of ZnO nanostructures (NSs) [54]. Additionally, Sounart et al. examined the secondary nucleation and expansion of ZnO nanostructures (NSs) and demonstrated that the growth kinetics of ZnO are consistent with classical nucleation and growth models [55]. The classical formation and growth of the critical nuclei is as shown in Figure 1.5.

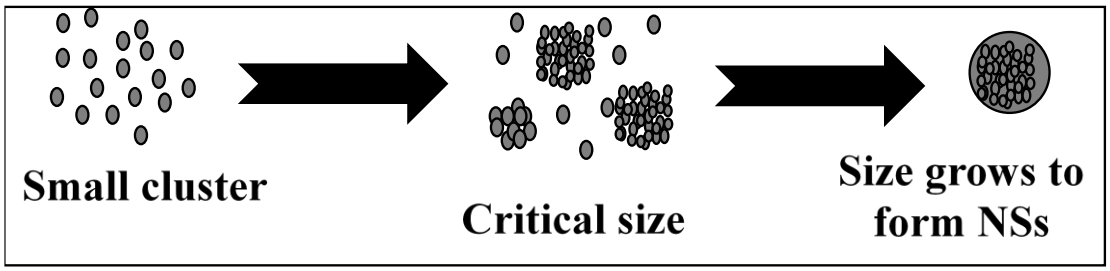

Figure 1.5: Classical model for homogenous nucleation.

Moreover, the process of homogeneous nucleation in the solution can be characterized by the Gibbs free energy equation, which incorporates both surface and volume terms [53]. The Gibbs free energy relation is given below:

$$\Delta G = 4\pi r^2\gamma + \frac{4}{3}\pi r^3 \Delta G_v \quad (1)$$

where ‘γ’ is the surface free energy term, having a positive value, ‘r’ being the size of the particle and ΔG_v is the volume free energy term which has negative value. By differentiating eq. (5) with respect to the ‘r’($\frac{d\Delta G}{dr} = 0$), the size of critical nuclei can be estimated. Here critical nuclei term refers to the minimum size of nuclei, which is able to grow into larger particle without being dissolved into the solution.

(iii) Classical growth model

In the classical model, growth of critical nuclei can occur via diffusion of species at the surface of nuclei or reaction mediated growth at the surface. Fick’s law explains the growth mediated by the diffusion of species at the surface of growing particle and is given by:

$$J = 4\pi x^2 D \frac{dC}{dx} \quad (2)$$

where ‘*D’* is the Diffusion coefficient, ‘*C’* is the concentration and represents the overall flux of monomers that pass through a spherical plane of radius *‘x’*.

The two main assumptions of the CNT are the spherical shape of particle and sharp interface between nuclei and liquid [53]. But these two assumptions can never work in every situation, as sometimes nucleation and growth can occur at diffused interface boundaries. Also spherical shape assumption is denied in case of NaCl and many others, where nucleus is cubic or having other structure. Another flaw in the idea is that it can't explain why the nucleation barrier vanishes at high super saturations.

1.5.2.2 Non-classical models

Nucleation and growth models presented by the CNT successfully explains the nucleation and growth mechanisms for many supersaturated solutions but still the theory failed to elaborate many other systems because of its over simplicity and assumptions of spherical particle. The theory failed to describe the nucleation rates and metastable intermediate states for the systems. Further the experiments, theories and computer simulations reveal the non-classical nature of nucleation. As per the non-classical theory of nucleation, the process is comprised of two steps. The first step involves the formation of a metastable intermediate phase alongside the formation of super

saturation, and the growth of nuclei are then occurred in the subsequent step. The various non-classical theories reported in literature are discussed below:

(i) Ostwald Ripening

This theory was put forward by the Wilhelm Ostwald in 1896. According to Ostwald ripening theory, very small sized nuclei formed in the solution undergoes dissolution and redeposit on the surface of bigger crystal *i.e.* larger crystals will be formed at the cost of smaller nuclei (Figure 1.6). Further the mathematical investigations of Ostwald ripening theory were conducted by the Lifshitz, Slyozov and Wagner (LSW) in 1958. The mathematical model was described for the systems where diffusion is the slowest process. The mathematical relation is given as:

$$\langle R^3 \rangle - \langle R^3 \rangle_0 = \frac{8 c_\infty v^2 D \gamma}{9 R_g T} t \qquad (3)$$

where $\langle R \rangle, \gamma, D, v, c_\infty$ and t is the average radius, surface energy term, diffusion coefficient, solubility and time respectively. It has been reported that the growth mechanism of ZnO nanostructures involves the Ostwald ripening process, which allows for the formation of a variety of nanostructures [56]. The main drawback of Ostwald ripening is that they have stability problem at high duration growth times. Hence, this model cannot be employed to investigate the growth mechanism of nanowires (NWs) in further studies.

Figure 1.6: Diagrammatic illustration depicting the Ostwald ripening phenomenon.

(ii) La Mer Mechanism

Studies on the mono disperse particles were developed in 1950s. La Mer and co-authors in orders to understand the growth mechanism has developed the nucleation and growth models. Thus La Mer curve describes the whole nucleation and growth process in three stages [57]. The first stage include the formation of small nuclei in the colloidal solution, in the second stage these small nuclei aggregates via self-nucleation to form a bigger nuclei and leads to decreases in the concentration of small nuclei. At the final stage the growth of these larger nuclei starts occurring with the addition of small nuclei (growth units).

(iii) Orientation attachment (OA)

Orientation attachment was the new concept to explain the growth mechanism of NPs into a specific structure, which comes into existence in 1990s. Orientation attachment is defined as the process of attachment of two growth units (colloidal particles) along a particular crystallographic direction in order to give a unique morphology to the NPs (Figure 1.7). OA reduces the total free energy of the growing particle while attaching and results in a stable structure. It was depicted from literature survey that variety of studies on the nanostructure growth of the ZnO NPs were observed to follow the orientation attachment phenomenon [58]–[60].

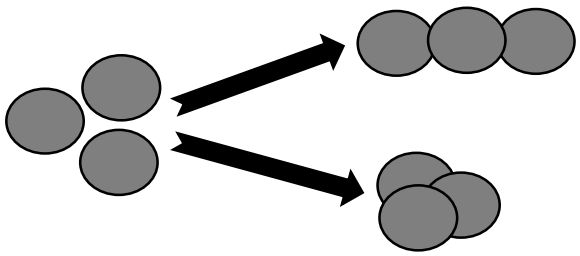

Figure 1.7: Schematic representation of Orientational attachments.

(iv) Molecular dynamics (MD) and Monte Carlo (MC) simulation

MD and MC are the simulation techniques to study the dynamics for variety of atoms and molecules. The fundamental concept behind Monte Carlo (MC) simulations is about the interactive forces between atoms and molecules; they utilize Newtonian mechanics to examine the changes in molecular systems. The simulations can be conducted under constant temperature and pressure conditions, taking into account only the interactions between atoms and molecules. As a result, comparing the simulation outcomes with experimental data became more straightforward. Moreover, in the molecular dynamic (MD) studies the system is described by the ball and spring model. In these simulations, force field parameters play an important role. They can be either determined from the experimental data or from calculations. The accuracy of these parameters determines the accuracy of the simulations. The main limitations of these simulations is the computational time, which is quite high [61].

(vi) Density functional theory (DFT)

DFT is a computational approach for analyzing the electronic structure of materials that gained popularity in the 1970s. It is a robust tool for investigating a wide range of nucleation processes. In contrast to classical nucleation theory (CNT), density functional theory (DFT) views free energy as a dependent variable of the average spherical density profile. It characterizes the changes in density within the center and bulk of the newly formed phase. By calculating the functional through DFT, various material properties can be deduced. The formation of nuclei per unit volume is expressed as follows:

$$J = Aexp(\frac{\Delta G_{DFT}}{KT}) \tag{4}$$

where 'ΔG_{DFT}' can be evaluated through DFT, 'J' represents the rate at which critical droplets are formed per unit volume. The pre-factor was taken same as that from CNT to calculate nucleation rate.

The above formula has similarities with the CNT, the only difference arise with the Gibbs free energy term (ΔG_{DFT}). Literature reveals the study of nucleation and thereafter growth of gold NPs on the modified surface of the ZnO using DFT [62]. Studies on various other metals (metal clusters) by using DFT were reported in the literature. Wang et al. reported the nucleation and growth of

Platinum clusters on the alumina substrate whereas Saidi et al. demonstrated Platinum NPs nucleation and growth on the MoS_2 substrate [63], [64]. Niranjan et al. demonstrated the ferromagnetic properties by combining the experimental characteristics with the theoretical DFT [65]. Despite of various approximations and assumptions, this theory failed to accurately measure the band gap, intermolecular interaction and ferromagnetism in the semiconductor materials.

(v) Phase field model (PFM)

The Phase field model is typically employed to address problems associated with interfaces through the use of a mathematical model. In PFM, only one parameter is used to define the boundary conditions, known as order parameter and represented by symbol '**φ**'. It is considered as a conserved quantity for Cahn-Hilliard equation (C-H), which solves the problems related to the temporal variation of the nucleate in the solution. While applying PFM, the assumption of diffused interface is considered rather than a sharp boundary. Local state of the system is defined by the order parameter, which tells the transition between disordered to ordered phase. For the 'n' ordered phases, the 'n' is the numbers of phase field parameters required to describe the system, which is also known as multiphase field theory. Further, PFM is nothing but the modified form of the Fick's law, with an additional interfacial term along with concentration term in their mathematical formula.

PF theory can be formulized by the free energy functional, which further depends upon the interfacial conditions and some other parameters such as spatial variation of phase field order parameter, interfacial width, temperature, orientations and field variables *etc*. and is given by: [66]

$$F(\phi,T)=\int_V\left\{\frac{1}{2}\left|W_0\nabla\phi\right|^2+f(\phi(x),T(x))\right\}d^3x \tag{5}$$

where $f(\phi,x)=\frac{\varepsilon}{2a^3}\phi(1-\phi)+\frac{k_BT}{a^3}\phi(x)\ln\phi+(1-\phi)\ln(1-\phi)$,

Here 'a' represents the distance between two distinct points and The coefficient 'W_0' has units of $(J/m)^{1/2}$.

The PF theory was reported in literature to depict various microstructure evolution phenomenon's. PFM was reported to study the grain growth, effect of thickness and orientation of the grain boundaries in polycrystalline materials [67]. Wang et al. demonstrated the growth mechanism and morphological transition of NW through multiphase field theory, which were experimentally prepared by the vapor liquid solid growth method [68], [69]. Thereafter, Wu et al. modeled the microstructure evolution of nano-scale materials using lattice phase field theory [70]. Moreover, literature also reveals the incorporation of higher order term to the free energy functional to demonstrate the morphological transformation in the microstructures [71]–[73].

1.5.3 EXPERIMENTAL METHODS

1.5.3.1 Optical Hyper Rayleigh Scattering (OHRS)

Optical Hyper-Rayleigh Scattering (OHRS) is a non-linear optical event that takes place when a sample is exposed to high-intensity light. Resulting in an elevation of the intensity of the scattered light at a frequency greater than that of the incoming light. OHRS can be utilized to investigate nucleation and growth processes in materials [74]. OHRS provides information about the size, shape, and distribution of nanoscale structures that are formed during nucleation and growth processes by measuring the scattered light's intensity and frequency. While studying material growth, OHRS can track the evolution of the nanoscale structures over time, offering insights into the underlying growth mechanisms and factors that determine the final structure and properties of a material. The primary drawback of OHRS is that it requires highly sensitive detector and a high-intensity fundamental light source. Nevertheless, using high-intensity light can sometimes cause optical effects such as stimulated Raman or Brillouin scattering, self-focusing, or dielectric breakdown, which may negatively influence the results of the experiment. [75].

1.5.3.2 Small angle X–ray scattering (SAXS) and Wide angle X–ray scattering (WAXS)

Small-angle X-ray scattering (SAXS) and wide-angle X-ray scattering (WAXS) are two complementary scattering techniques utilized to investigate the structure of materials. SAXS provides information about the arrangement of atoms, molecules, and nanostructures on a length scale of to nanometers to several microns, while WAXS provides information on a length scale of a few nanometers to a few microns. Both SAXS and WAXS are valuable in analyzing the formation

and growth of crystalline materials in real-time and determining the impact of growth conditions (*viz.* temperature and composition), on the crystallization process. During nucleation, small clusters of atoms begin to form the crystal structure, while during growth, these clusters grow and merge to form the final crystal structure. Small-angle X-ray scattering (SAXS) and wide-angle X-ray scattering (WAXS) can provide valuable information about the size, shape, and distribution of clusters, leading to a better understanding of the mechanisms involved in their formation and growth. Such insights can be crucial in optimizing growth conditions and developing novel materials [76][77]. However, there are some limitations and drawbacks to using SAXS and WAXS for studying nucleation and growth. For example, the methods may not be able to accurately determine the structure of very small or highly disordered systems. In addition to this they have very complex/expensive instrumentation.

1.5.3.3 UV-vis absorbance studies

UV-vis spectroscopy is a valuable technique for studying the nucleation and growth process of materials. The absorption of light in the UV-vis range can provide information about the electronic structure of molecules. During the nucleation process, the formation of new particles or crystals can be monitored by observing changes in the absorbance spectrum. As the size and number of particles increase, the absorbance can shift to longer wavelengths, indicating the formation of larger particles. In the growth stage, UV-vis spectroscopy can be used to monitor the kinetics of crystal growth by measuring the increase in absorbance over time. By analyzing the absorption spectra at different time intervals, the growth rate of the crystals can be calculated. Real time monitoring of nucleation and growth of silver sulfide NPs were reported to carried out using UV-vis data analysis [78]. Nucleation and growth of $CoPt_3$ nanocrystals were also studies using the same technique [79]. UV-vis spectroscopy can also be used to study the surface plasmon resonance (SPR) of nanoparticles [80]. By measuring the absorbance at different wavelengths, information about the size and shape of the nanoparticles can be obtained.

1.5.3.4 Transmission electron microscopy (TEM)

TEM works by transmitting a beam of electrons through a thin sample, allowing for high-resolution imaging of the sample's structure. In the case of NPs, TEM can provide information on the size, shape, distribution and crystal structure of the particles. It can also provide information on the

nucleation and growth process, which is important for understanding how the particles form and how their properties can be tuned [81]. To use TEM for studying nucleation and growth of NPs, the first step is to prepare a thin sample. This can be done by dispersing the NPs in a liquid and then dropping a small amount onto a carbon-coated grid. The liquid is then allowed to evaporate, leaving a thin layer of NPs on the grid. Once the sample is prepared, it is loaded into the TEM and imaged using a high-resolution electron beam. By analyzing the images, researchers can track the evolution of the NPs over time and gain insights into the mechanisms of nucleation and growth. For example, researchers can use TEM to observe the formation of small clusters of atoms or molecules, which then grow into larger NPs over time. Lee and colleagues conducted a study on the nucleation and growth of nanoparticles (NPs), utilizing several transmission electron microscopy (TEM) images. They then performed a detailed analysis of these images, incorporating machine learning techniques for image analysis [82]. They can also observe the formation of defects and dislocations in the crystal structure of the NPs, which can affect their properties.

1.6 RESEARCH GAP

The study of growth and aging of NPs has been an important topic in the field of nanotechnology. Literature reports both experimental and theoretical approaches to study growth and aging of nanoparticles (NPs). Experimental methods include optical hyper Rayleigh scattering (OHRS), small-angle X-ray scattering (SAXS), and wide-angle X-ray scattering (WAXS) *etc*. While these techniques offer high resolution (ranging from a few hundred milliseconds to a thousand milliseconds), they are primarily restricted to metal nanoparticles (NPs). Moreover, their sophisticated instruments require proper handling. Theoretical models include Classical Nucleation Theory (CNT), Lifshitz-Slyozov-Wagner (LSW), Ostwald Ripening, Density Functional Theory (DFT) and Dynamical Density Functional Theory (DDFT). However, these models have many disadvantages when applied to study growth dynamics. Classical nucleation theory (CNT) is inadequate in explaining both the nucleation rate and interfacial energy, while Lifshitz-Slyozov-Wagner (LSW) theory is restricted to diffusion-limited growth. On the other hand, density functional theory (DFT) and dynamic density functional theory (DDFT) are purely quantum mechanical and do not incorporate thermal fluctuations during nucleation and growth. Moreover, the literature lacks the incorporation of the effect of aging on the cross-sectional transformations

of ZnO NWs, and is unable to provide proper explanations for the shifts in the absorbance and emission spectra for materials having dimensions in the bulk regime. However, there are a number of studies on the shifts in optical properties in the quantum regime. This highlights the need for further research to understand the effect of aging on the morphology and optical properties of NSs.

1.7 MOTIVATION AND OBJECTIVES

1.7.1 Motivation

Our motivation is to understand the fundamentals of the growth and aging in NPs, as well as the to study the effect of growth conditions (i.e. time and temperature) on the morphological and on the optical properties of ZnO NWs.

1.7.2 Objectives

Based on the motivation, the objectives of the work were structured, which are given as:

Objective 1. Studies on temporal growth and aging of ZnO NPs.

Objective 2. Effect of temperature on the morphological and optical properties of ZnO NWs.

Objective 3. Effect of growth time on the morphological and optical properties of ZnO NWs.

1.8 THESIS ORGANIZATION

The thesis is organized into five chapters in accordance with the objectives:

Chapter 1: "Introduction". This chapter contains the brief introduction to the ZnO material, reason for choosing ZnO, nucleation and growth models, various existing synthesis methods and the applications of the ZnO in various fields of nanotechnology.

Chapter 2: "Studies on temporal growth and aging of ZnO nanoparticles**".** This chapter introduces the synthesis of ZnO NPs and understanding of the nucleation and growth processes by both experimental as well as by theoretical approach.

Chapter 3: "Effect of temperature on the morphological and optical properties of ZnO NWs". This chapter includes the synthesis of nanoseeds and NWs. The effect of different temperatures (70℃,

90℃ an 120℃) at constant growth time (8h) on the optical properties and morphology of the NWs were incorporated and analysed.

Chapter 4: "Effect of growth time on the morphological and optical properties of ZnO NWs". This chapter describes the optical properties of the ZnO NSs obtained at different growth times at constant growth temperature. The core importance of this chapter is the red shift in the near band edge emission peak of the PL-emission spectra, which shows the red shift with the effect of increase in the growth time. The concept of band bending in the NWs were introduced and explained.

Chapter 5: "Conclusion and Future scope". This chapter includes the overall conclusion and future proposal of the present thesis.

CHAPTER-2

STUDIES ON TEMPORAL GROWTH AND AGING OF COLLOIDAL NANOPARTICLES

2.1 INTRODUCTION

The formation and evolution of NPs is a complex and dynamic process that is governed by the interplay of various physical and chemical phenomena. Nucleation, growth and aging are the three essential stages in the process that depicts the morphology, dimensions and properties of the NPs. Nucleation, in general, refers to the process where small clusters of atoms or molecules aggregate to form a critical nucleus and create a new thermodynamic stable phase with a lower free energy from an previous phase with a higher free energy [83]. The phase transition phenomena, *i.e.* crystallization conducted by evaporation or anti solvent agent, have been addressed by nucleation. Phase transition phenomenon was reported to occurred by secondary nucleation or by crystal growth [84]. As nucleation phenomenon deals with the molecular levels (nanometer scale), it is extremely difficult to comprehend the process in the simplest manner. However, it is quite challenging to obtain the nucleation time and nuclei size from experimental data and computer simulations *etc*. Thereafter, growth is the process by which the nucleus increases in size and transforms into a stable particle. Additionally, aging refers to the gradual change in the properties and behavior of the particle over time, as a result of exposure to external conditions and internal interactions. The understanding and control on these processes can help us to achieve desired morphology with desired dimensions and properties [85]. Moreover, by having simple control over the morphology and size of the NPs, various devices can be created with desired properties. However, the exact phenomenon behind these processes is still unknown. Despite there are many ideas, both classical and non-classical, that have been developed since the beginning of studies to explain the nucleation, growth and aging phenomenon [86]–[88]. The classical models include classical nucleation theory (CNT), which consist classical nucleation and growth models. Furthermore, non-classical models include Ostwald ripening, La Mer mechanism [57], Orientation attachment, density functional theory (DFT), and phase field (PF) model [89] and others [90]. The Phase field model (PFM) is currently been one of the most effective theoretical model to understand the phase transformation processes such as evolution of microstructure and solidification dynamics *etc.* already discussed in the chapter-1 (Section-1.6.2).

It was also observed from literature that the aging of NPs (which was found to be the slowest step) has been widely reported in comparison to the nucleation and growth processes. Experimental techniques that were recently proposed to study nucleation, growth and aging are OHRS, SAXS

and WAXS. The main drawback of these experiments while applying to the current study is that they are only appropriate for metallic NPs [91], [92]. The coupling of these experimental techniques with the UV-vis spectroscopies was also widely reported in the literature. Maria et. al. demonstrated that the nucleation is temperature dependent and is a very slow phenomenon [91]. Galloway employed the UV-vis technique to examine the nucleation and growth of CdSe NPs and showed that the nucleation begins in the growth solution within 30 sec. [93]. Therefore, it can be inferred from literature that the UV-vis spectroscopy studies can be used to study growth and aging dynamics in the growth solution.

According to reports, numerous environmental factors, including precursor concentration, temperature, growth time, pH and capping agent *etc*. , cause ZnO nuclei to grow to different NSs [94], [95]. Research indicates that increasing the concentration of precursors leads to higher density and larger size of ZnO structures [96]. Temperature can affect the decomposition, mobility and diffusion of precursors, resulting in different morphologies [97]. The extension of growth periods may lead to coagulation or an increase in the dimensions of the resulting structures. Additionally, the morphology of these structures is largely determined by the pH, as it affects the environment surrounding the nuclei [98], [99]. Additionally, capping agents such as Hexamethylenetetramine (HMTA), triethanolamine (TEA), oleic acid, and thioglycero can be employed to prepare nanowires/nanorods and stabilize nanoparticles [100].

In this chapter, experimental as well as theoretical approaches were employed to investigate the growth and aging of colloidal NPs. The growth and aging process of NPs were studied experimentally by using the in situ UV-vis absorption spectroscopy and Transmission electron microscopy images. Moreover, a mathematical framework was put on to explain the temporal evolution of NPs and to support the experimental observations.

2.2 MATERIALS AND METHODS

The process of sample preparation involves a straight forward chemical synthesis using $ZnCl_2$, NaOH as initial salts and ethanol and water as the solvents. These compounds were utilized in their pure form. Firstly, two separate solutions of (i) $ZnCl_2$ (1 mM) and NaOH (2 mM) and (ii) $ZnCl_2$ (1.25 mM) and NaOH (2 mM) were prepared. Ethanol was used as a solvent to prepare the solution, with a small quantity of water with continuously stirring at RT. Finally a uniform colloidal

suspension of $Zn_n^{2+}(OH^-)_m(H_2O)_lCl_k^-$ or Zn-complexes such Zn^{2+}, $Zn(OH)^+$, $Zn(OH)_2$, $Zn(OH)_3^{2-}$ and $Zn(OH)_4^{4-}$ were achieved [101][102] . The chemical reaction involved in the formation of products by this process is given by:

$$\begin{aligned} &\boldsymbol{nZnCl_2 + 2nNaOH + lH_2O} \\ &\qquad \rightarrow \boldsymbol{Zn_n^{2+}(OH^-)_m(H_2O)_lCl_k^- + (2n-m)OH^- + 2nNa^+ + (2n-k)Cl^-} \\ &\qquad \rightarrow \boldsymbol{nZnO + (l+n)H_2O + 2nNaCl} \end{aligned} \quad (1)$$

where *'**n**'* and ***'l'*** signifies the number of moles for $ZnCl_2$ and H_2O respectively, here $\boldsymbol{m + k = 2n}$ for zero charge precursor (homogeneous nucleation) precursor.

2.2.1 Balanced and unbalanced chemical reactions

Two distinct samples, S1 (atomically balanced precursor concentration, 1 mM of $ZnCl_2$ and 2 mM of *NaOH*) and S2 (atomically unbalanced precursor concentration, 1.25 mM of $ZnCl_2$ and 2 mM of *NaOH*), were selected for the present work. Sample S1 was chosen according to the balanced precursor concentrations whereas sample S2 according to the unbalanced precursor concentration. However, sample S2 has a slightly higher concentration of Zn^{2+} ions compared to sample S1. This sample (S2) was selected to study the impact of excess Zn^{2+} ions environment near Zn complex nuclei on its growth and aging processes. Only 25% additional Zn precursor was utilized in this case. If a greater amount were employed *i.e.* 50% or 70%, the subsequent effects could manifest:

(i) A burst of nuclei might occur due to the easy availability of Zn^{2+} ions in the growth solution.

(ii) An excess of Zn precursor can lead to steric hindrance around the Zn complex nuclei, which may result in the retardation of nuclei growth.

2.2.2 Characterization

The UV-vis absorption spectra of samples S1 and S2 were measured using a UV-visible-NIR spectrophotometer (Perkin Elmer Lambda 750, USA) at 0, 6, 12, 18, 24, 30 and 36 minute intervals to study the temporal evolution of the NPs. The spectral range was set between 280-450 nm and each scan lasted approximately for 2 minutes. Additionally, TEM images were captured at the same

time intervals to monitor the evolution of NPs with time. Phase Field (PF) modeling was used to simulate the growth of the NPs. All experiments were carried out at Room temperature (RT).

2.3 REACTION-DIFFUSION MEDIATED NUCLEATION

Before the study of growth dynamics, the formation of nuclei should be understood first. The formation of nuclei and growth process begins with diffusion and proceeds with the reaction of the precursors. Equation (1) depicts the chemical reaction between '***n'*** number of moles of $ZnCl_2$ and '***2n'*** number of moles of NaOH for the synthesis of ZnO NPs.

Thereafter, consider a drop of 2 ml NaOH (2 mM) into the homogeneous solution of $ZnCl_2$ (1 mM). Due to the gradient in precursor concentrations, NaOH diffuses into the $ZnCl_2$ solution, leading to a chemical reaction and formation of final products. The start of a chemical reaction is closely linked to the initial diffusion process. In the current scenario, the ions need to diffuse over a distance equivalent to the radius of the NaOH droplet for the reaction to be considered complete. Hence by using following relation, diffusion time can be calculated by:

$$r_{droplet} = (6Dt)^{1/2} \qquad (2)$$

where ***'$r_{droplet}$'*** is the radius of a droplet, '***D'*** is the diffusion constant (***D*** = 1.3 x 10^{-5} cm^2-sec^{-1}), and '***t'*** is the time in seconds.

A droplet of *NaOH* with volume of 2 ml and with a radius of about 0.7 mm (*4/3 π r3* droplet = 2 ml) takes roughly 10 seconds to fully diffuse. Based on this calculation, the ions are expected to diffuse completely into the $ZnCl_2$ solution in approximately 10 seconds. This will result in the interaction/ reaction of OH^- ions at the surface of Zn^{2+} ions, leading to the formation of $Zn(OH)_2$, which acts as a nucleus for further growth. However, the diffusion of *NaOH* into $ZnCl_2$ is slow compared to its chemical reaction at the surface. Thereafter, in order to understand the effect of reaction term onto the diffusion coefficient, when both diffusion and reaction is involved in the same system, a mathematical treatment is required.

In the present case, mathematical treatment can be carried out by assuming the concentration of nuclei $Zn(OH)_2$ be directly related to the concentration of *NaOH*, which is given as:

$$C_{Zn(OH)_2} = R\, C^n{}_{NaOH}$$

where ***n = 1, 2, 3*** and so on, '***R'*** is a constant and $C_{Zn(OH)_2}$, $C^n{}_{NaOH}$ represents concentrations of *Zn(OH)₂* and *NaOH* respectively. In case of chemical diffusion reactions, '***R'*** physically represents the nucleation rate.

Therefore, if '***R'*** is very large, the production of $Zn(OH)_2$ will be higher. The equation for diffusion is given as follows [103]:

$$\frac{dC}{dt} = D\frac{d^2C}{dx^2} - \frac{dS}{dt}, \textbf{ for linear equilibrium} \quad (3)$$

for *n = 1, S = R C* (where $C_{Zn(OH)_2} = S$).

$$R\frac{dC}{dt} = D\frac{d^2C}{dx^2} - \frac{dC}{dt} \quad (4)$$

$$\frac{dC}{dt} = \frac{D}{R+1}\frac{d^2C}{dx^2} \quad (5)$$

This means that if the '***R'*** participates in equation (5), the diffusion constant '***D'*** will slow down the entire process of diffusion by a factor of ***'(R+1)'***. Likewise, the diffusion equation (6) with ***n = 2*** becomes:

$$\frac{dC}{dt} = \frac{D}{2R+1}\frac{d^2C}{dx^2} \quad (6)$$

(The value of ***'D'*** will decrease by a factor of ***'2R+1'***). This implies that the optimal approach for continued growth is to consider the presence of a large number of nuclei in the solution. Since diffusion and reaction are interdependent events, the effective diffusion constants are represented by $D(R+1)^{-1}$ and $D(2R+1)^{-1}$ for ***n = 1*** and ***2***, respectively. These values lead to the formation of *Zn(OH)₂* nano-colloids that are suspended in the solution. Further to note that in equation (5), local reactions or any nonlinear combinations of C_{NaOH} are not accounted for. Moreover, the varying forms of *R(C)* lead to various equations, such as the 'Newell-Whitehead Segel' equation and 'the Zeldovich' equations, which substitute *R(C)* with *R(C) = C(1-C)*, *R(C) = C(1-C²)*, and *R(C) = C(1-C)(C-α),* respectively [104] [105].

2.4 COUPLING AND DECOUPLING OF GROWTH AND AGING

2.4.1 Experimental analysis and concept of coupling and decoupling

In order to study growth dynamics, the absorbance spectra of samples S1 and S2 for the different growth time intervals were recorded (Figure 2.1). Absorbance spectra show completely different nature of the curve for both of the samples S1 and S2. This dissimilarity is attributed to the excess Zn^{2+} ions present in sample S2, which results in a prevalence of scattering rather than absorbance in this sample. From the absorbance spectra of S1, it was observed that the half of the absorbance maximum intensity ($I_{max}/2$) remains constant (Figure 2.1a) whereas the absorbance maxima show the red shift with the growth time. This indicates that over time, the distribution of particle sizes remains constant, but the overall size of the particles steadily increases. Therefore, the time derivative of the absorbance maximum '$\boldsymbol{\alpha_{max}}$' ($\boldsymbol{\alpha_{max}}$ corresponds to the maximum absorbance value) for S1 and S2 is carried out and shown in Figure 2.2. Furthermore, for the dynamic case, (non-equilibrium state) the absorption can be represented by:

$$\boldsymbol{\alpha(t) = \frac{dC_{Zn(OH)_2}}{dt} = k_{rea} C_{ZnCl_2}^{n_1} C_{H_2O/ethanol}^{n_2}} \tag{7}$$

and time derivative of equation (7) is given by:

$$\boldsymbol{\frac{d\alpha(t)}{dt} = \frac{d^2 C_{Zn(OH)_2}}{dt^2} = \frac{dk_{rea}}{dt} C_{ZnCl_2}^{n_1} C_{H_2O/ethanol}^{n_2} + k_{rea} \frac{d(C_{ZnCl_2}^{n_1} C_{H_2O/ethanol}^{n_2})}{dt}} \tag{8}$$

where $\boldsymbol{C_{Zn(OH)_2}}$, $\boldsymbol{C_{ZnCl_2}^{n_1}, C_{H_2O/ethanol}^{n_2}}$ indicate the concentrations of *Zn(OH)₂* NPs, *ZnCl₂*, *H₂O/ethanol*, $\boldsymbol{k_{rea}}$ represents the reaction rate, and $\boldsymbol{n_1}$ and $\boldsymbol{n_2}$ are the reaction orders respectively. Moreover, $\boldsymbol{k_{rea}}$ is temperature dependent and given by Arrhenius equation (9) [106]. The Arrhenius equation's time derivative is represented by:

$$\frac{dk_{rea}}{dt} = \frac{E_A}{RT^2}\exp(-\frac{E_A}{RT})\frac{dT}{dt} \quad (9)$$

where 'E_A' represents the activation energy, 'RT' represents the thermal energy.

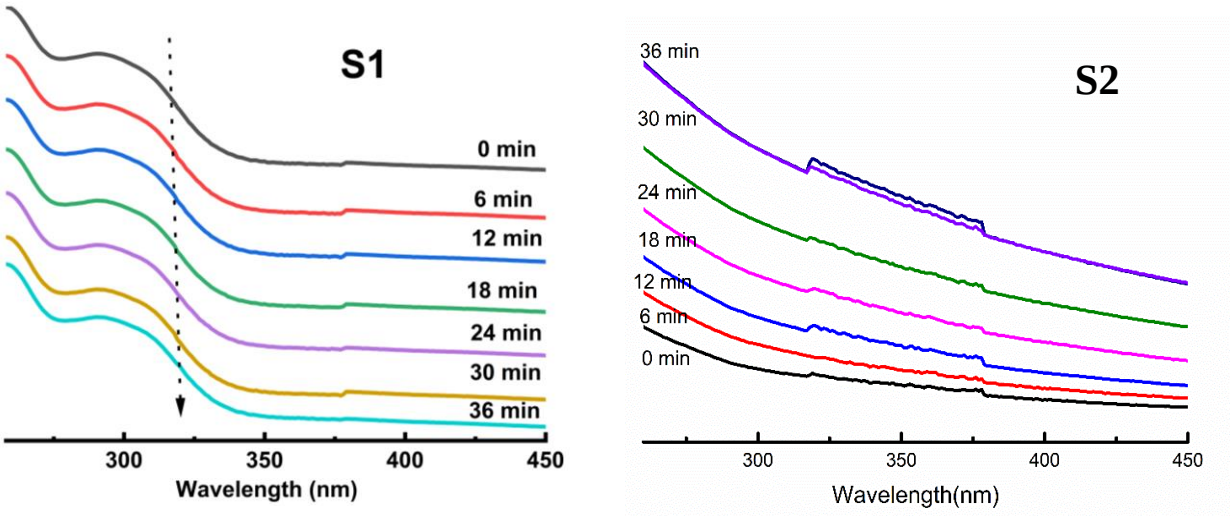

Figure 2.1: UV-vis spectra of ZnO colloidal NPs for samples S1 and S2 (0, 6, 12, 18, 24 and 24 minutes).

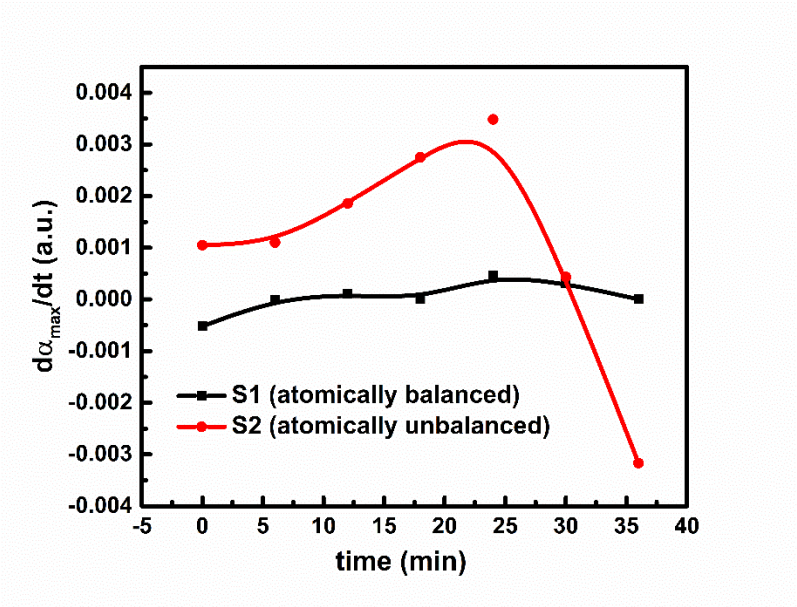

Figure 2.2: Variation of rate of change of absorption maximum with growth time for S1 and S2.

Additionally, Equation (8) highlights that changes in absorption maxima can provide valuable information about the temporal progression of both the reaction rate and reactant concentration. Figure 2.2 depicts how the rate of change in $\boldsymbol{\alpha_{max}(t)}$ varies over time for samples S1 and S2. For S1, the value of $\boldsymbol{d\alpha_{max}(t)/dt}$ remains nearly constant, indicating a consistent growth and aging for the NPs in the samples. Conversely, for S2, the $\boldsymbol{d\alpha_{max}(t)/dt}$ value initially increases up to 20 min, followed by a sudden drop to a negative value. This could be attributed to the excessive concentration of Zn^{2+} ions in the solution, which left behind after the complete reaction between Zn^{2+} and OH^- ions. It renders the nucleation unstable by retarding their growth process. Presence of excess Zn ions in the solution also leads to modify the electrostatic interaction between NPs and solvent, which therefore contributes to significant changes in surface energy. This demonstrates a decoupling of growth grown species after 20 minutes of growth time.

Thereafter, the direct or indirect band gap energy between the two electronic states (VB maximum and CB minimum) can be determined by using the Tauc plot, which is provided by the equation. 10 [107], [108]. The equation 10 a is given by:

$$\alpha h\upsilon = A^*(h\upsilon - E_g)^{\mathbf{1/2}} \qquad \text{If } h\upsilon \geq E_g \qquad (10\text{ a})$$

Here, '$\boldsymbol{A'}$' is a constant which shown an inverse relation to the refraction index ($\boldsymbol{\mu}$) of the sample and given by [109]:

$$A = \frac{e^2 E_K (2m_\tau)^{3/2}}{3\lambda_o \hbar m_e \in_o \mu E_g^2} \qquad (10\text{ b})$$

where 'E_K' is the Kane energy, 'e' is charge on an electron, 'm_τ' is the effective mass, 'λ_o' is the photon wavelength, '$\in_o$' is the permittivity of free space and 'μ' is the refractive index. However, till the steady-state is not established, '$\boldsymbol{\mu'}$ is not constant. As the time proceed in the case of transient growth of NPs, the value of '$\boldsymbol{\mu'}$ changes. But under the assumption that nuclei formed within 10 sec., and NPs size and aggregation occurs over a very short time scale compared to the time scale of measurement, it can be presumed that particle density remains constant throughout the process and the refractive index '$\boldsymbol{\mu'}$ of the NPs remains unchanged over transient growth Hence, Tauc plot can be utilized to find band gap value in the present case (equation 10).

Therefore, Figure 2.3 depicts the variation of the band gap for sample S1 and S2 with respect to the growth time. The variation of time derivative of the band gap with respect to time is shown in Figure 2.4. The particle size was determined using the Brus equation, and is represented by: [110], [111].

$$E = E_g^{bulk} + \frac{h}{8e}\left(\frac{1}{m_o m_e} + \frac{1}{m_o m_h}\right)\frac{1}{r^2} - \frac{1.8e}{4\pi\varepsilon\varepsilon_o}\frac{1}{r} \qquad (11)$$

where 'E_g^{bulk}' is the band gap of bulk ZnO NPs, 'ε_0' represents the permittivity of free space (8.85×10^{-12} F/m), 'm_0' = 9.1×10^{-31} kg, 'r' is the size of the NPs, 'm_e' and 'm_h' are the effective masses of the electrons and holes (0.26 and 0.59), and 'ε' is the relative permittivity of *ZnO* (ε ~ 8.5).

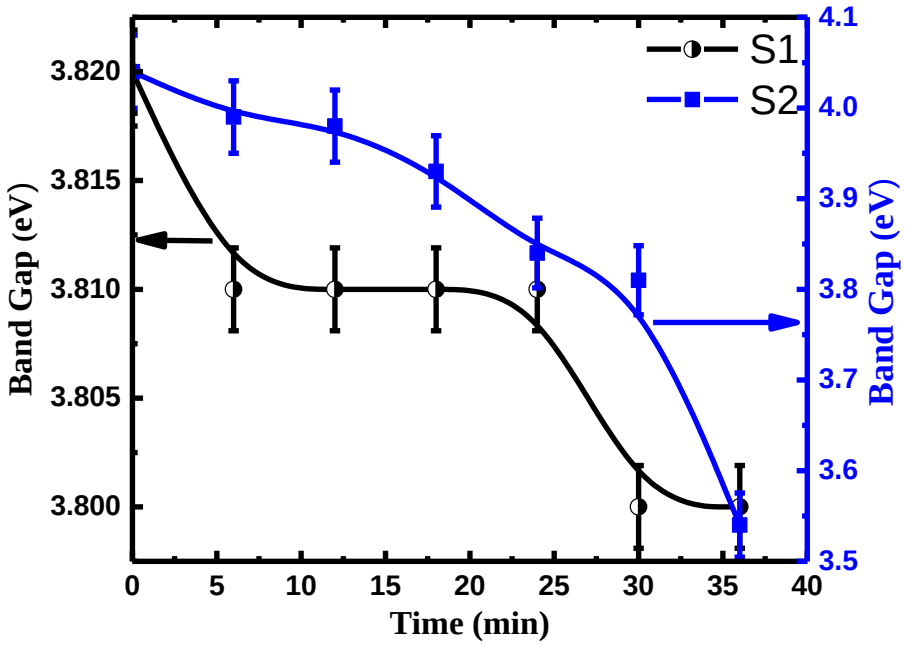

Figure 2.3: Variation of band gap with growth time.

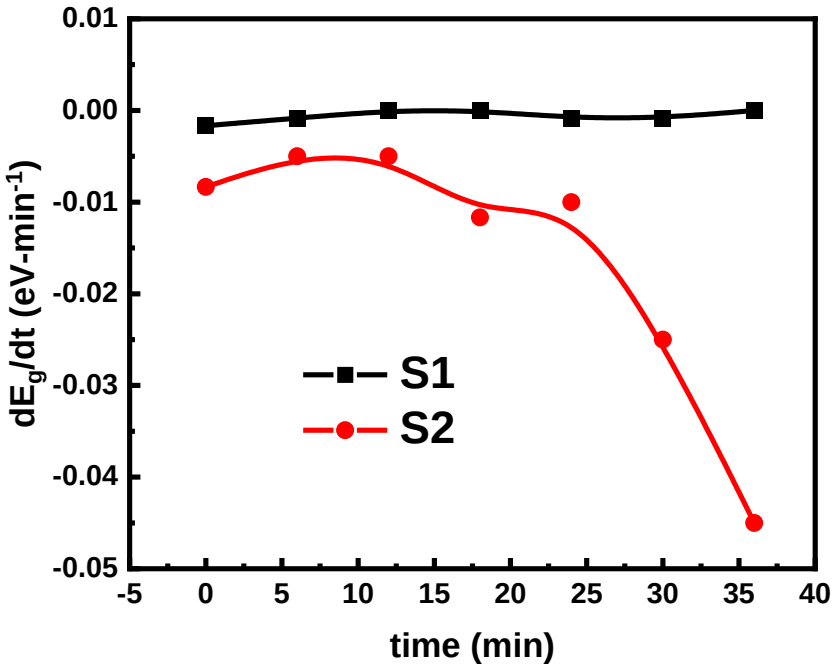

Figure 2.4: Rate of change of band gap with respect to growth time.

Here, particle size varies with changes in the growth time, means that the particle size is a function of time *i.e.* ***r (t)***. Therefore, time derivative of Eqn. (11) is carried out and given by:

$$\frac{dE_g}{dt} = -\underbrace{\frac{h\pi}{3e}\left(\frac{1}{m_o m_e}+\frac{1}{m_o m_h}\right)\left(\frac{1}{\frac{4}{3}\pi r^3}\frac{dr}{dt}\right)}_{\text{Ist}} + \underbrace{\frac{1.8e}{\varepsilon\varepsilon_o}\left(\frac{1}{4\pi r^2}\frac{dr}{dt}\right)}_{\text{IInd}} \qquad (12)$$

In the above mentioned equation, the Ist term implies volume dependency and the IInd term reflects surface dependency. For steady-state, where $\boldsymbol{dE_g/dt = 0}$ depicts the constant surface to volume ratio when solved using equation (12). Furthermore, Figure 2.4 illustrates the constant value of slope ($\boldsymbol{dE_g/dt = 0}$) for S1, depicting the continuous aging or constant surface to volume (S/V) ratio. During the first 20 minutes of S2, the slope of $\boldsymbol{dE_g/dt}$ shows a positive trend, which is followed by a decrease to a negative value. When $\boldsymbol{dE_g/dt}$ is positive, the IInd term takes precedence, indicating volumetric dominance, as it is inversely related to the surface term. This suggests volumetric growth of NPs is occurring. However, when $\boldsymbol{dE_g/dt}$ becomes negative, surface dominance occurs, indicating surface-mediated growth in the solution.

Subsequently, the particle size was determined using Brus equation. Figures 2.5 and 2.6 provide graphical representations of how particle size changes over time for samples S1 and S2, respectively. The experimental data was fitted to the equation for modeling purposes:

$$\mathbf{d = d_0 + kt^p} \quad (13)$$

where '***d'*** represents the particle size**,** ***'d_0'*** stands for the initial particles size and '***k'*** indicates the proportionality constant which physically stands interface energy. For uniformly dispersed colloidal nanoparticles, the parameter ***'p = 1/3'*** denotes completely diffusion-controlled growth. The function plot of equation 13 is shown in Figures 2.5 and 2.6 for ***p*** = 1/3 and 1/2 respectively. With a fitting accuracy of 98 percent, the fitting parameters for S1 are $\boldsymbol{d_0}$ = 1.61± 0.06 nm, ***p*** = 0.37 ± 0.06, and ***k*** = 0.11 ± 0.03, whereas for sample S2 the parameters are $\boldsymbol{d_0}$ = 1.78±0.05 nm, ***p*** = 9.99±1.72, and ***k*** = 6.28 x 10^{-16}. Sample S1 and S2 show a completely opposite behavior in curvature in the functional plots (Figure 2.5 and 2.6). The value of constant '***k'*** for S2 is very low which signifies the weak interaction between the particles. This leads to dispersion of NPs away from each other and clearly describes the decoupling. Additionally, the constant '***k'*** influenced by the local curvature of interfacial energy. In S2, the local thermodynamic fluctuations result in a significant variation in the curvature of the interfacial energy, which leads to the decoupling of nanoparticles.

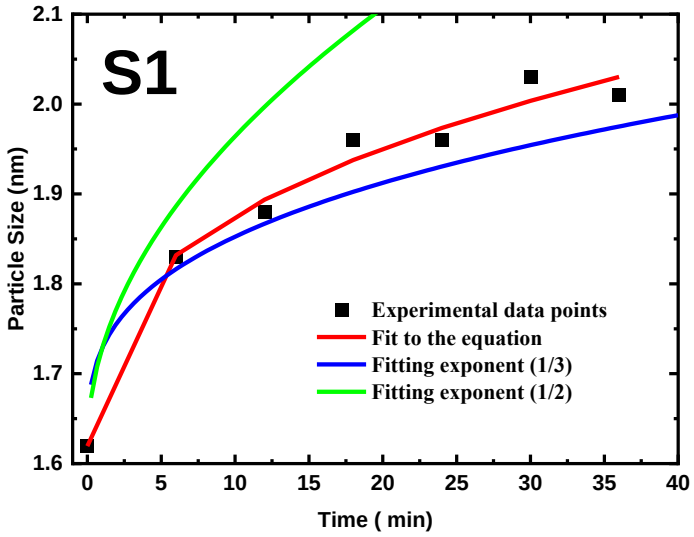

Figure 2.5: Particle size variation with the growth time (for S1) fitted using two fitting exponents of 1/3 and 1/2.

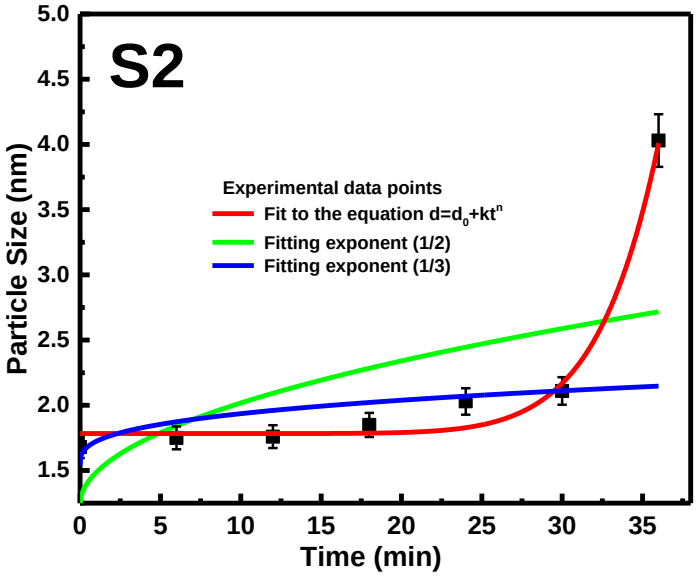

Figure 2.6: Particle size variation with the growth time (for S2) fitted using two fitting exponents of 1/3 and 1/2.

In order to investigate how the shape of colloidal S2 nanoparticles is affected in sample, NPs were put on the TEM grid after sonication for their imaging purpose. Figure 2.7 displays the TEM images for the sample S2 for various growth times. Figure 2.7 (a→e) shows a clear cluster formation of the NPs. The log-normal particle size distribution was fitted for the histogram plots and is depicted in the inset of Figure 2.7. Figure 2.7(f) displays an extremely narrow log-normal distribution, which serves as a visual confirmation of the decoupling phenomenon.

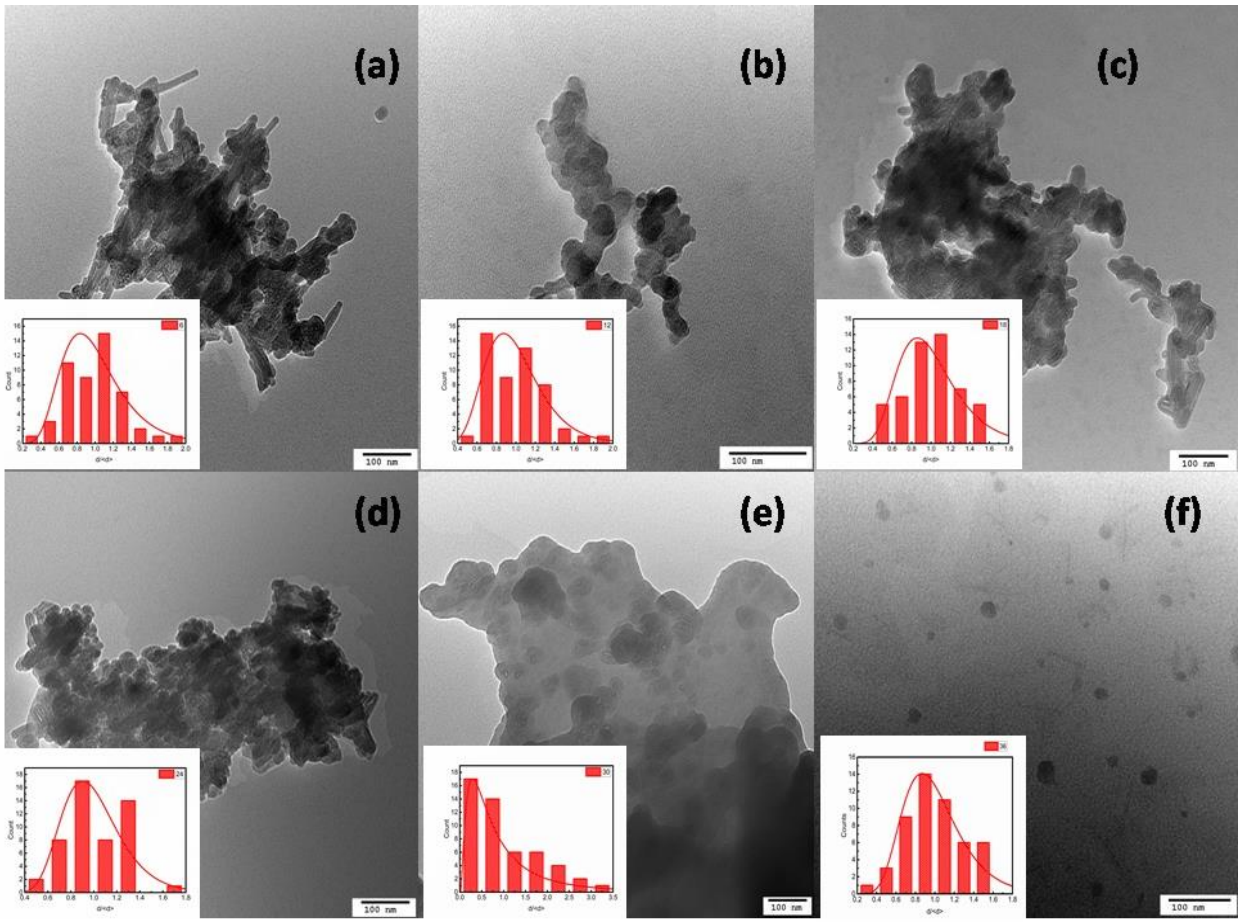

Figure 2.7: TEM images of the NPs for sample S2 (a→0 min, b→6 min, c→12 min, d→18 min, e→24 min, f→36 min) and inset represents the respective histogram plots with log normal curve fitting.

2.5 THEORETICAL MODEL FOR GROWTH

2.5.1 Phase-Field Modeling (PFM)

Theoretical approach is required to comprehend the growth mechanisms of NPs. For, the theoretical method it is being assumed that all nucleation centres have developed and are ready for the subsequent growth. Therefore, to study growth of NPs theoretically, PF theory is being used which characterize the whole state of system with the conserved structural order parameter ***φ (r,t).***

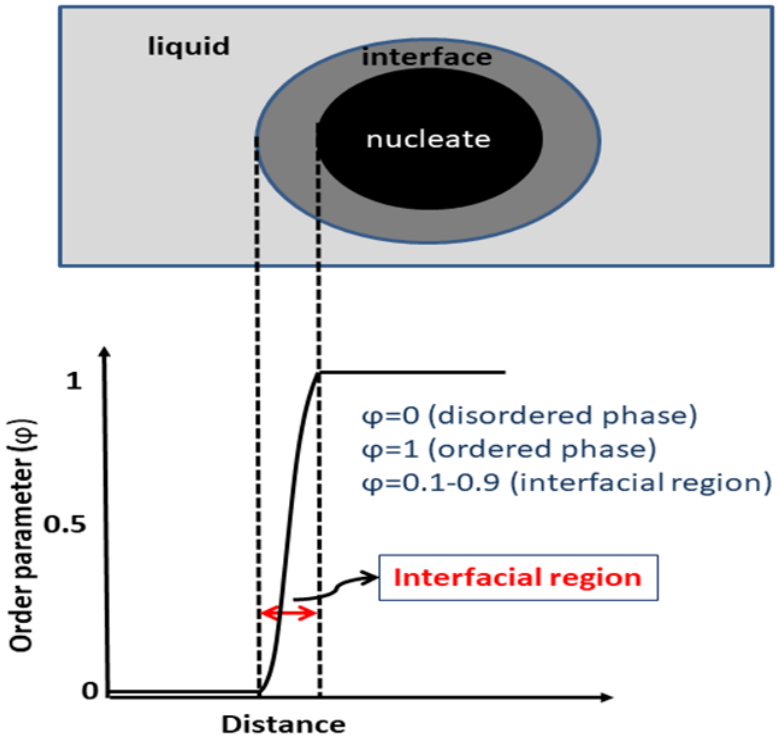

Figure 2.8: The disorder -order transformation of the growing nano-colloids.

A potential solution involves nucleation centers that consist of ordered phases, liquid phases and a boundary between the nucleation centers and the liquid. It is assumed that the phase transition between the two phases will occur over a considerable distance, surpassing the width of the interfacial region. A constant interfacial energy value was assumed for the present case. This is an important assumption since a constant interfacial energy will probably result in spherical particles. whereas a spatially variable interfacial energy ($\nabla\varphi$) will yield diverse morphologies, such as nano-

flowers, nano-flakes, NWs and NRs *etc.* [112], [113]. In the present case, no involvement of latent heat was assumed. Therefore, in this scenario, Phase Field Modeling (PFM) is implemented to describe the time-dependent evolution of the phase field. Additionally, phase dynamics gives a clear visualization of ongoing phase transformation in the system. In this case, the order parameter (***φ***) remains conserved. The values of ***φ*** = 0 and 1 signifies the disordered and ordered phases, respectively whereas values between 0 to 1 represents the diffusive interface as shown in Figure 2.8.

The C-H (Cahn –Hilliard) equation can be written as [34,35]:

$$\frac{\partial \varphi}{\partial t} = -\nabla.\left(-M\nabla\frac{\delta F}{\delta \varphi}\right), \text{ or } \frac{\partial \varphi}{\partial t} = \nabla.M\nabla\mu \tag{14}$$

$$\frac{\partial \varphi}{\partial t} = -\nabla.\vec{J} \tag{15}$$

where $\vec{J} = -M\frac{\delta F}{\delta \varphi} = -M\mu$ and $\mu = \frac{\delta F}{\delta \varphi}$. (16)

The phase, solute mobility, chemical potential, and total free energy functional are represented by ***φ, M, μ*** and ***F*** respectively. General expression for free energy is given by:

$$f(\varphi, x) = \frac{\varepsilon}{2a^3}\varphi(1-\varphi) + \frac{k_B T}{a^3}\varphi(x) ln\varphi + (1-\varphi)\ln(1-\varphi) \tag{17}$$

Here, the generalized expression of free energy does not contain the gradient term ($\nabla\varphi$), which is important to explain the diffused interface boundaries in the phase separation processes. Therefore, in order to incorporate the gradient term in the free energy, the general free energy needs to be modified. Thus free energy can be expanded using Taylor series expansion as given by:

$$F\left(x, y, z, , \frac{\partial \varphi}{\partial x}, \frac{\partial \varphi}{\partial y}, \frac{\partial \varphi}{\partial z}, \frac{\partial^2 \varphi}{\partial x^2}, \frac{\partial^2 \varphi}{\partial y^2}, \frac{\partial^2 \varphi}{\partial z^2}\right) = \int f dV \tag{a}$$

Tailor expansion of the terms given as:

$$f = f(c) + \underbrace{\frac{\partial f}{\partial \nabla \varphi_i}}_{\alpha_i} (\nabla\varphi)_i + \underbrace{\frac{\partial f}{\partial (\nabla^2\varphi)_{ij}}}_{\beta_{ij}} (\nabla^2\varphi)_{ij} + \frac{1}{2!} \underbrace{\frac{\partial^2 f}{\partial (\nabla\varphi)_i \partial (\nabla\varphi)_j}}_{\gamma_{ij}} (\nabla\varphi)_i (\nabla\varphi)_j \dots\dots\dots\dots\dots\dots\dots$$

$$f = f(\varphi) + \alpha_i (\nabla\varphi)_i + \beta_{ij} (\nabla^2\varphi)_{ij} + \frac{\gamma_{ij}}{2} (\nabla\varphi)_i (\nabla\varphi)_j \dots\dots\dots\dots \quad \text{(b)}$$

The total free energy (F) is given by:

$$F = \int f dV \quad \text{(c)}$$

Here, total free energy can be named as free energy functional (as it is function of a function). Thereafter, let the odd rank tensors $\alpha_i = 0$ (equation b), because of inversion symmetry (all α_i values does not gives us the minima).

Further, $\int \beta_{ij} (\nabla^2\varphi)_{ij} dV = \int \beta_{ij} \frac{\partial^2 \varphi}{\partial x_i \partial x_j} dV$

$$= \int \beta_{ij} \frac{\partial}{\partial x_i} \left(\frac{\partial \varphi}{\partial x_j} \right) dV$$

$$= \int \beta_{ij} \frac{\partial}{\partial x_i} (\nabla\varphi)_j dV$$

$$= \beta_{ij} (\nabla\varphi)_j \Big]_s - \int \frac{\partial \beta_{ij}}{\partial x_i} (\nabla\varphi)_j dV \quad \text{(d)}$$

Let first term of the equation (d) to be equal to zero as we are interested in volume term only. Thus the modified equation (d) becomes:

$$\int \beta_{ij} (\nabla^2\varphi)_{ij} dV = - \int \frac{\partial \beta_{ij}}{\partial x_i} (\nabla\varphi)_j dV$$

Further, total free energy can be written as:

$$F = \int \left[f(\varphi) + \left[\frac{\gamma_{ij}}{2} - \frac{\partial \beta_{ij}}{\partial \varphi} \right] (\nabla\varphi)_i (\nabla\varphi)_j \right] dV$$

$$F = \int \left[f(\varphi) + \kappa_{ij} (\nabla\varphi)_i (\nabla\varphi)_j \right] dV$$

For cubic system $\kappa_{ij} = \kappa_{ji}$ and by introducing Kronecker delta function to the above equation

$$F = \int \left[f(\varphi) + \kappa \delta_{ij} (\nabla\varphi)_i (\nabla\varphi)_j \right] dV$$

For i=j, we have

$$F = \int [f(\varphi) + \kappa (\nabla\varphi)^2] dV \tag{18}$$

Equation (18) is known as total free energy or free energy functional. Above mentioned function "***F***" depends upon the order parameter $\boldsymbol{\varphi}$ and its gradient ($\nabla\boldsymbol{\varphi}$). Thus this gradient term can help to explain problem related to the diffused interface boundaries.

Further, taking derivative of equation (18) w.r.t. φ given as:

$$\frac{\partial F}{\partial \varphi} = \frac{\partial f(\varphi)}{\partial \varphi} - \nabla . 2\kappa (\nabla\varphi)$$

$$\mu N = \frac{\partial f(\varphi)}{\partial \varphi} - 2\kappa (\nabla^2 \varphi) \tag{19}$$

Here, $\mu = \frac{1}{N} \frac{\partial F}{\partial \varphi}$

(μ represents the chemical potential)

Furthermore, diffusion equation can also be written as:

$$\frac{\partial \varphi}{\partial t} = -\nabla . J \qquad \text{where, } J = -M\nabla\mu$$

$$\frac{\partial \varphi}{\partial t} = -\nabla.(-M\nabla\mu)$$

$$\frac{\partial \varphi}{\partial t} = M\nabla^2\mu$$

$$N\frac{\partial \varphi}{\partial t} = M\nabla^2\left[\frac{\partial f(\varphi)}{\partial \varphi} - 2\kappa(\nabla^2\varphi)\right] \quad \text{(using equation 19)}$$

$$N\frac{\partial \varphi}{\partial t} = M\nabla^2\frac{\partial f(\varphi)}{\partial \varphi} - [2\kappa M(\nabla^4\varphi)] \quad (20)$$

where J and M represents the flux and mobility respectively. For per atom free energy (N=1), the aforementioned expression can be expanded in the following manner:

$$\frac{\partial \varphi}{\partial t} = M\nabla^2\frac{\partial f(\varphi)}{\partial \varphi} - [2\kappa M(\nabla^4\varphi)] \quad (21)$$

Thus, Equation (21) is commonly referred to as the Cahn-Hilliard equation. In this expression ***'f'*** represents the free energy given by equation (17). Further this free energy (equation 17) contains the logarithmic terms which are very difficult to incorporate for numerical implementations. Therefore, simple free energy function ***f (φ)*** was chosen which is given by:

$f(\varphi) = A\varphi^2(1-\varphi)^2$, where A is the free energy constant (22)

This free energy formula is simple and represent the double well potential type function *i.e*. two minima's and one maxima, which is required for phase separating systems. The variation of the free energy function with the order parameter is depicted in Figure 2.9, with '***A'*** symbolizing the barrier height that must be overcome to move from one phase to the other. In the present case, barrier height was chosen to be ***A*** = ***1*** and ***2*** as shown in Figure 2.9.

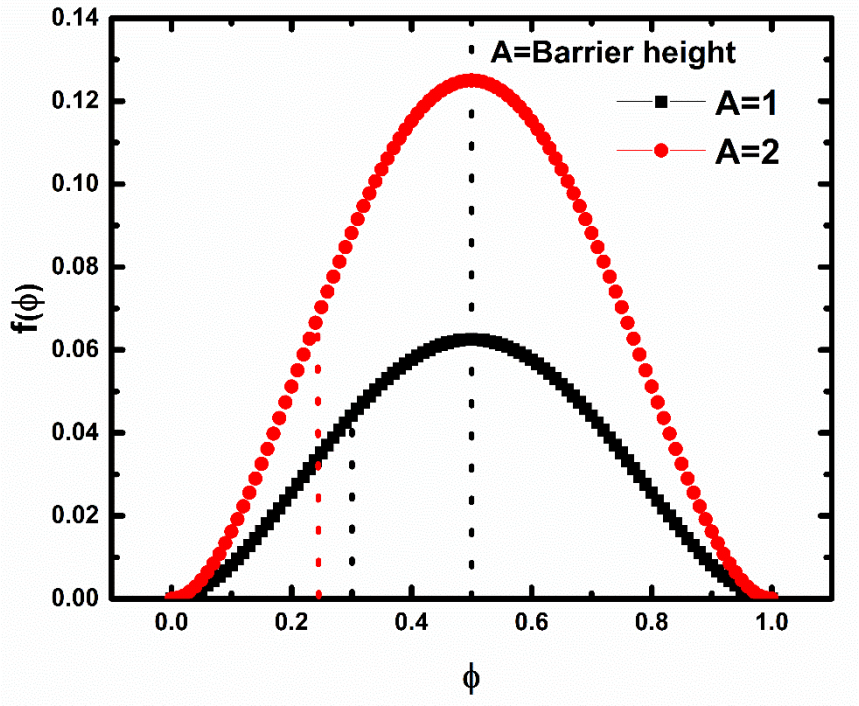

Figure 2.9: Variation of the free energy verses the order parameter.

2.5.2 Numerical Implementations

Equation (21) can be rewritten in simple form as:

$$\frac{\partial \varphi}{\partial t} = \nabla . M \nabla (\mathrm{h} - 2\kappa \nabla^2 \varphi) \tag{23}$$

$$\text{Also, } \frac{\partial \varphi}{\partial t} = M\nabla^2 (\mathrm{h} - 2\kappa \nabla^2 \varphi)$$

Here, $\boldsymbol{h} = \frac{\partial f(\varphi)}{\partial \varphi} = 2A\varphi(\varphi - 1)(2\varphi - 1)$,

'κ' represents the gradient energy coefficient which depicts interfacial energy.

The equation (23) is simulated using the Fourier transformation method and expanded as:

$$\frac{\partial \{\varphi\}_k}{\partial t} = -Mk^2(\{h\}_k + 2k^2 \kappa \{\varphi\}_k) \tag{24}$$

where '$\boldsymbol{k}$' is the Fourier vector and $\{.\}_k$ denotes the spatial Fourier transform of quantity{.}. Semi-implicit discretization of Equation (24)and is provided by:

$$\frac{\varphi(k,t+\Delta t)-\varphi(k,t)}{\Delta t} = -Mk^2\{h\}_k - 2k^4 M\kappa\,\varphi(k,t+\Delta t)$$

$$\varphi(k,t+\Delta t) = \frac{\varphi(k,t) - Mk^2\{h\}_k\Delta t}{1+2\Delta t\,\kappa\,\mathrm{Mk}^4} \qquad (25)$$

The symbol **'Δt'** signifies the temporal resolution used in numerical approximation. Scaled parameters are employed in the simulation, with the grid size being scaled to the interfacial width ***(W)***, the time step being scaled to ***(τ)*** and the free energy functional being scaled to $\boldsymbol{k_BT}$. In this case, both the free energy constant (*A*) and gradient energy are dimensionless quantities. Consequently, the crucial scaled parameters for computation are the initial concentration/order parameter of nucleates (***φ***), the free energy constant (***A***), the solute mobility (***M***), and the interfacial energy (***κ***). However, to provide spatial fluctuation to ***φ***, a very modest noise term (0.002) was included. At two separate time steps ***t***, the size evolution of two different sets of parameters, ***(φ = 0.25, A = 2, M = 0.5, κ = 0.5 and φ = 0.30, A = 1, M = 1, κ = 0.5)*** were observed as shown in Figure 2.10 and 2.11. It was clear from the simulated images that at Δt **= *100,*** there are no occurrence of nuclei formation. However, as the growth time proceeds, nuclei formation starts to occurs and follows $\boldsymbol{d = d_0 + kt^{1/3}}$ relation, where '***d'*** represents the particle size.

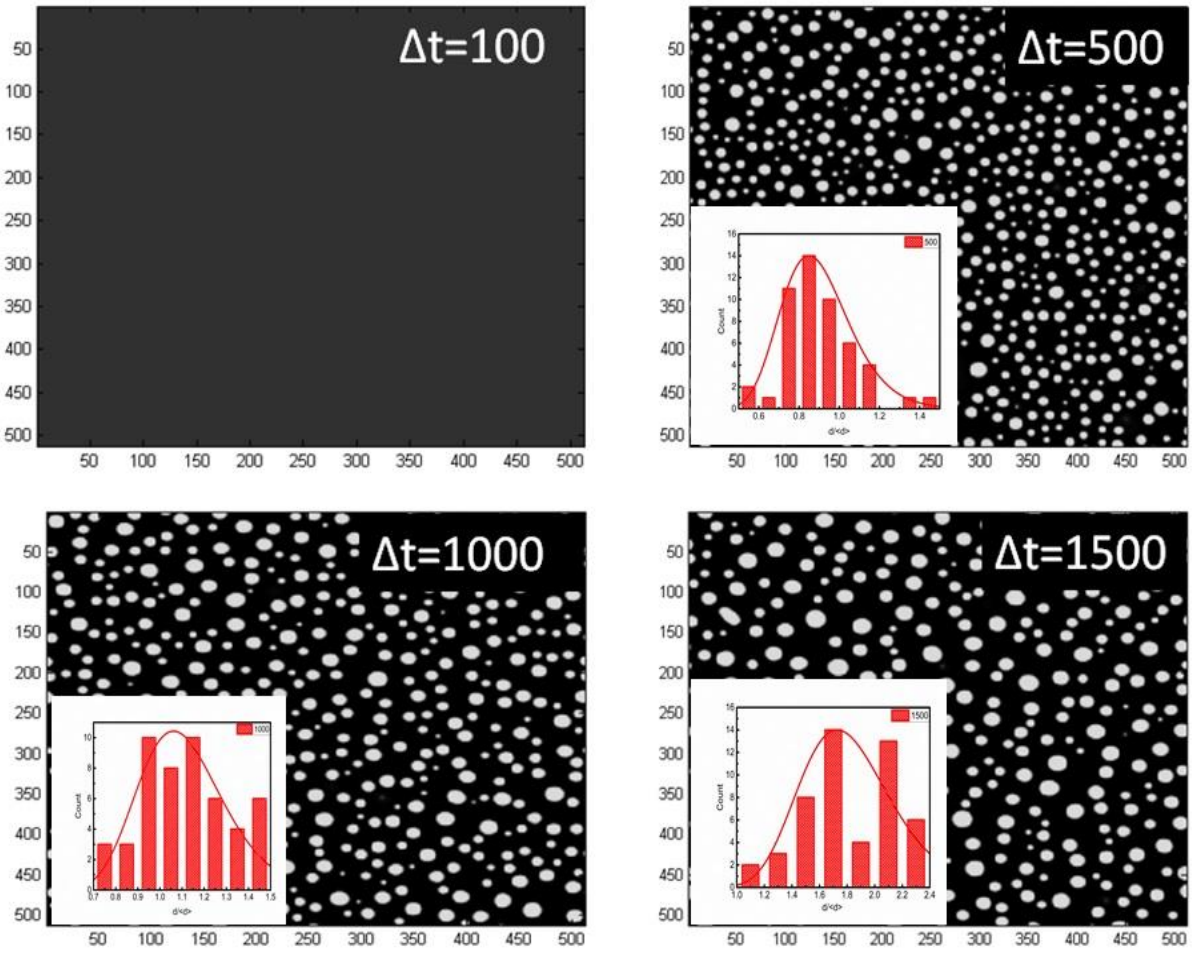

Figure 2.10: Visualizing the Temporal Evolution of Nano-Particles: Simulated Images and Log-Normal Distributions with Varying Time Steps ($\varphi = 0.25$, $A = 2$, $M = 0.5$, $\kappa = 0.5$).

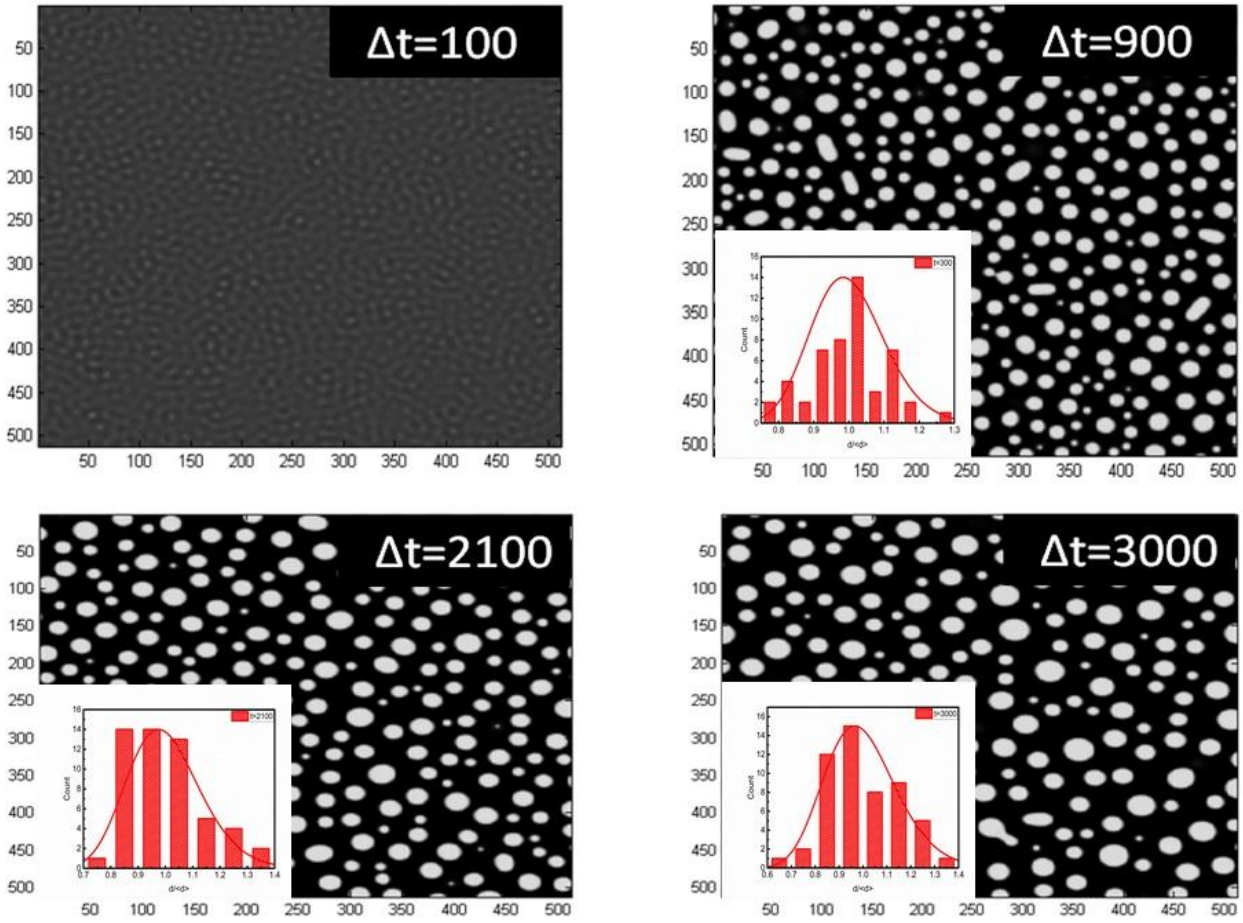

Figure 2.11: Visualizing the Temporal Evolution of Nano-Particles: Simulated Images and Log-Normal Distributions with Varying Time Steps (***φ*** *= 0.30, A = 1, M = 1, κ = 0.5).*

2.6 CONCLUSIONS

The current study investigated the evolution and aging of ZnO NPs in colloidal suspensions using both experimental and theoretical approaches. The objective of this chapter was to develop a thorough understanding of the growth and aging of nanoparticles (NPs). Based on the study, the following conclusions were drawn:

- Experimental investigations using UV-vis spectroscopy and TEM, demonstrate that nucleation and growth occur within 2 minutes in the growth solution.
- It was found that atomically balanced reactions (S1) result in growth and aging of NPs, while atomically unbalanced reactions (S2) results in decoupling of growth due to the existence of an excessive amount of Zn ions environment around nuclei.
- The outcome of the absorbance spectroscopy experiment indicates that the change in $d\alpha_{max}(t)/dt$ over time remains constant for sample S1, indicating continuous aging of the NPs in the sample. Moreover, for S2, the variation in $d\alpha_{max}(t)/dt$ rises up to 20 minutes and then falls, indicating decoupling of growth due to the presence of an excess of Zn ions.
- Thereafter, the rate of change of band gap energy *i.e.* dE_g/dt for sample S1 maintains constant value, indicating a constant S/V ratio of the NPs. However, dE_g/dt for sample S2 firstly shows an increase up to 20 minutes and then a sudden decrease to a negative value, implying surface-mediated growth of the NPs in the sample.
- The variation in particle size with growth time for both the samples displays a change in radius of curvature. The positive curvature for sample S1 indicates the consistent growth and aging whereas negative curvature observed in sample S2 is attributed to thermodynamics fluctuations and decoupling.
- The evolution of phase or size of NPs was understood and modeled using a phase field model (PFM).

CHAPTER-3

EFFECT OF TEMPERATURE ON THE MORPHOLOGICAL AND OPTICAL PROPERTIES OF ZnO NWs

3.1 INTRODUCTION

From the preceding chapter, the effect of atomically balanced and unbalanced precursor concentrations on the growth and aging of the NPs were evaluated. It was determined that nucleation occurs rapidly in the solution, followed by growth and aging of the NPs. It was also observed from TEM images that $ZnCl_2$ precursor leads to the formation of aggregated NPs, which cannot be further utilized as seeds to grow ZnO NWs. Even $ZnCl_2$ precursor cannot be used to prepare NWs because it contains Cl^- ions, which promotes the plate like morphological of NSs [116]. This is because $ZnCl_2$ precursor leads to the formation of stable layered zinc hydroxyl salt (LZHS) *i.e.* $(Zn_n^{2+}(OH^-)_m(H_2O)_lCl_k^-)$, which was also mentioned in equation no. 1 of Chapter-2, which gives the plate like morphology [117]. Therefore, requirement of other precursors as well as suitable method is much needed for the NPs and NWs growth.

Additionally, the morphological features such as the diameter, length and shape, significantly affect the ZnO NSs properties and performance [118]. Concentration of dopants were also reported to impact the morphological features [119]. Subsequently, the growth time and temperature are significant factors that can influence the morphology of ZnO NWs during their growth processes [52], [120]. By tuning the duration of growth and the temperature conditions, researchers have succeeded in producing desired morphological structures, such as uniform diameter and high aspect ratio NWs [3]. Recently, various studies have explored the impact of growth duration at different temperature conditions on transformation of the shape and diameters of ZnO NWs. In a study conducted by Amin et al., the impact of growth time on the morphological changes of hydrothermally grown ZnO NWs was investigated. The results revealed that an increase in growth time led to an increase in the length to diameter ratio (aspect ratio) of the NWs. [52]. Similarly, Cesar et al. reported that by increasing the growth time, the diameter and length of ZnO NWs increases which were grown by a hydrothermal method [121].

As a result, this chapter examines the effect of growth temperature on the shape, diameters and optical absorption and emission of ZnO NWs. This was done by recording their FESEM images, UV-vis absorbance and PL-emission spectra at various growth temperatures (70°C, 90°C and 120°C) conditions (Growth time ~ 8h).

3.2 SYNTHESIS METHOD

There are numerous approaches to prepare ZnO NWs on the variety of substrates. However, the chemical approach stands out as the most advantageous due to its simplicity, reliability and low cost for large-scale production [122]. This approach also enables precise control of the NWs' morphology and dimensions. To initiate the process of growing ZnO NWs, seeded layer must first be prepared on the substrate. This step is crucial for achieving good adhesion and lattice matching to minimize strain in the sample. However, if the NWs are obtained in powder form from the growth solution, this step can be omitted. This section provides a detailed discussion of the chemical approach utilized for the synthesis of ZnO NWs.

3.2.1 ZnO seeds preparation

The seed layer is synthesized by depositing a uniform layer of ZnO NPs onto the required substrate using solution of zinc acetate prepared in ethanol. The solution is prepared by mixing 5 mM zinc acetate with ethanol and stirring for 15 minutes at room temperature. The solution is then drop-wise dispersed onto a cleaned substrate and dried for a few seconds on a hot plate before being rinsed with ethanol. This process is repeated 2-3 times to ensure a uniform seed layer. The final step is to dry the seeded substrate for twenty minutes at 350°C in a muffle furnace. The schematic representation of ZnO seed layer formation is represented in Figure 3.1. The advantage of this layer is to reduce stress and strain in the prepared NWs.

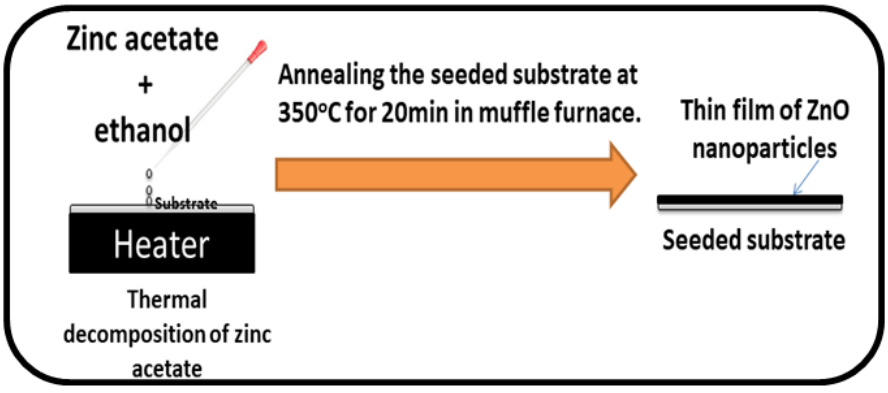

Figure 3.1: Schematic representation of ZnO seed layer formation.

3.2.2 Preparations of ZnO Nanowires

In the present case, ZnO nanowires were synthesized via simple chemical approach. Two separate solutions of equimolar concentrations (40 mM) of zinc nitrate hexahydrate and hexamethylenetetramine (HMTA) were prepared in Milli-Q water. Thereafter, both the solutions were properly mixed for 1 hour at varied temperature conditions by using magnetic stirrer. Afterward, the substrates that had been seeded in stage-1 were immersed in a growth solution and allowed to undergo growth for various durations (2, 4, 8, 16, 20, and 24 hours) under various growth temperatures (70ºC, 90ºC, and 120ºC). Thereafter, the obtained samples were in oven. Figure 3.2 illustrates the growth process of ZnO NWs. The resulting ZnO nanowires typically ranged in diameter from 170 nm to 560 nm and in length from 0.516 µm to 4.476 µm. The chemical reaction that facilitated the growth of the NWs in the solution can be expressed as follows [123]:

$$Zn(NO_3)_2.6H_2O \rightarrow Zn(NO_3)_2 + 6H_2O \quad (1)$$

$$Zn(NO_3)_2 \rightarrow Zn^{2+} + 2NO_3^- \quad (2)$$

$$NO_3^- + H_2O \rightarrow NO_2^- + 2OH^- \quad (3)$$

The decomposition of HMTA is given below:

$$(CH_2)_6N_4 + 6H_2O \rightarrow 6HCHO + 4NH_3 \quad (4)$$

$$4NH_3 + 4H_2O \rightarrow 4NH_4^+ + 4OH^- \quad (5)$$

$$2OH^- + Zn^{2+} \rightarrow Zn(OH)_2(s) \quad (6)$$

$$\xrightarrow{70^0C,\ 8h} ZnO\ (chain\ like\ NWs) + H_2O \quad (7)$$

$$\xrightarrow{90^0C,\ 8h} ZnO(\ hexgonal\ NWs) + H_2O \quad (8)$$

$$\xrightarrow{120^0C,\ 8h} ZnO(broken\ NWs) + H_2O \quad (9)$$

Here, zinc nitrate was used to provide the suitable amount of Zn^{2+} ions supply in the growth solution, while HMTA was used to produce well-defined hexagonal ZnO NWs. HMTA decomposes to ammonia and formaldehyde as given by the equations (3) and (4). Studies have shown that due to its non-polar nature, the chelating agent HMTA tends to preferentially bind to the non-polar facets of the ZnO NWs. As a result, it blocks the growth in the radial direction and permits growth of only one preferred direction [95]. Despite the use of HMTA, the diameters of NWs are continually increasing with increase in growth time. This is because as growth time progresses, the ammonium and hydroxide ions get consumed, resulting in weak bonding of HMTA at the lateral surface and corresponding increase in diameters. In another studies HMTA was believed to behave as a pH buffer in the growth solution by slowly decomposing into ammonia, to provide a continues and controlled supply of NH_3 and OH^- ions to the solution [8], [9]. As the growth temperature increases, there is a corresponding increase in the release and consumption of ammonia and hydroxide ions in the growth solution. This has a direct impact on the reaction kinetics and consequently, the final morphology of the NWs gets affected. Therefore, HMTA plays a crucial role in shaping the morphology of the NWs [125]. The other factors that affect the growth and growth rate will be studied further in next sections.

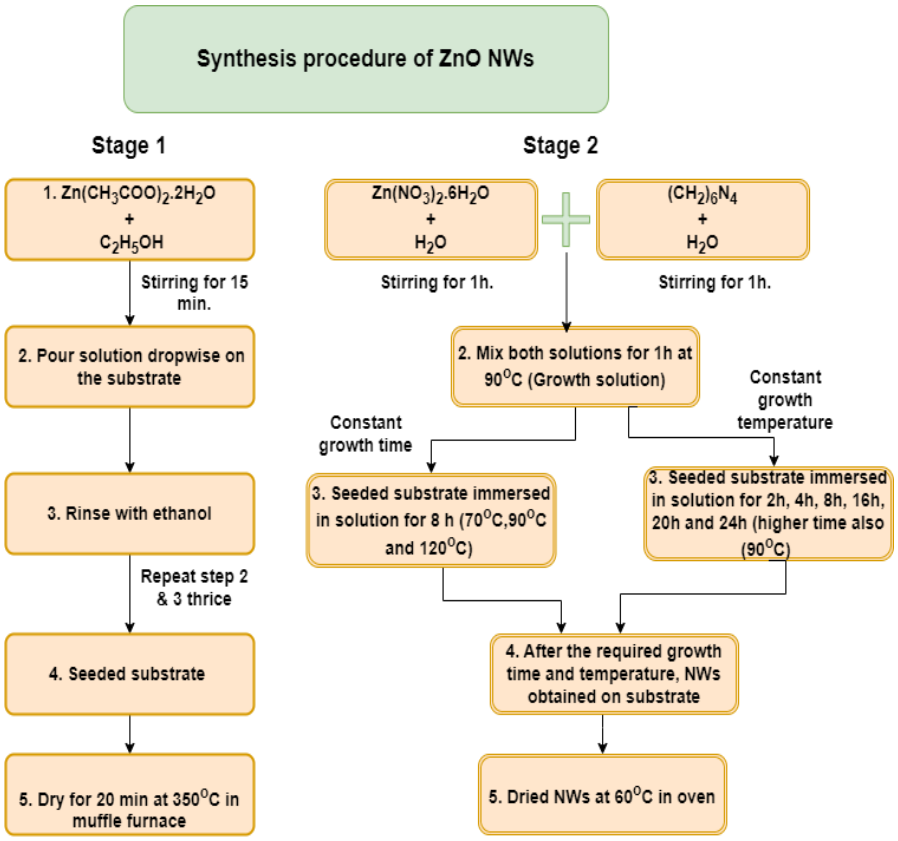

Figure 3.2: Diagrammatic representation for the synthesis of Nanowires.

3.2.3 Characterizations

The X-ray diffraction spectroscopy technique was utilized to determine the crystallographic structure of the obtained NSs, using X'Pert PRO PANalytical instrument with Cu-Kα source (λ=1.54056 Å) to generate X-rays. The Field Emission Scanning Electron Microscopy (FESEM-Supra 55, Carl Zeiss, Germany) technique was employed to visualize the size distribution and shape of the synthesized ZnO NWs. The absorbance spectra of the samples were obtained using a Perkin Elmer Lambda 750 UV-visible-NIR spectrophotometer, over the wavelength range of 300 nm to 550 nm. Following this, photoluminescence (PL) measurements were conducted with a Perkin Elmer LS-55 spectrophotometer, using a Xenon lamp as the excitation source. The sample was excited with energies lower than their band gap energies, and the corresponding emission spectra were recorded using the same instrument over a range of 350-700 nm wavelengths.

3.3 RESULTS AND DISCUSSION

3.3.1 X-ray diffraction studies

To confirm the crystalline structure of the prepared samples, X-ray diffraction data were recorded and displayed in Figure 3.3. The X-Ray diffraction spectra indicate that the ZnO nano seeds have a preferred orientation along the (002) plane and exhibit the wurtzite hexagonal structure, confirmed by the diffraction peaks (100), (002), (101), (102), (110), (103), and (201) matching with the standard JCPDS (JCPDS - 36-1451, a = b = 3.24982, c = 5.20661, $\alpha = \beta = 90^0$, $\gamma = 120^0$). The XRD spectra of samples prepared at various temperatures with a constant growth time of 8 hours are depicted in Figure 3.4. which also displays the same number of peaks and confirms wurtzite hexagonal structure. The peaks below 30 degree represented by asterisk belong to the quartz substrate. Further, Table 3.1 displays the intensity ratio of (002) plane with (100), (102) and (110) planes for ZnO nano seeds and NWs. Table 3.1 signify the following main points:

(i) The intensity ratio of (002) - plane is higher than other planes ((100), (102) and (110)-planes) for ZnO nano seeds, which shows that grans in seeds have preferred direction along c-plane.

(ii) As randomly aligned NWs were grown on nano seeds at different growth temperatures the polycrystalline growth in the sample enhances, which is confirmed from their intensity ratios of XRD peaks.

(iii) Thereafter, the intensity ratio of I_{002}/I_{110} and I_{002}/I_{100} were found to increase with the growth temperature. This increase in intensity with the growth temperature signifies the improvement of crystal quality with the application of growth temperature.

(iv) The intensity ratio of I_{002}/I_{102} shows maximum value for 90ºC, which signifies the growth along z-plane compared to the xz-plane for this particular temperature.

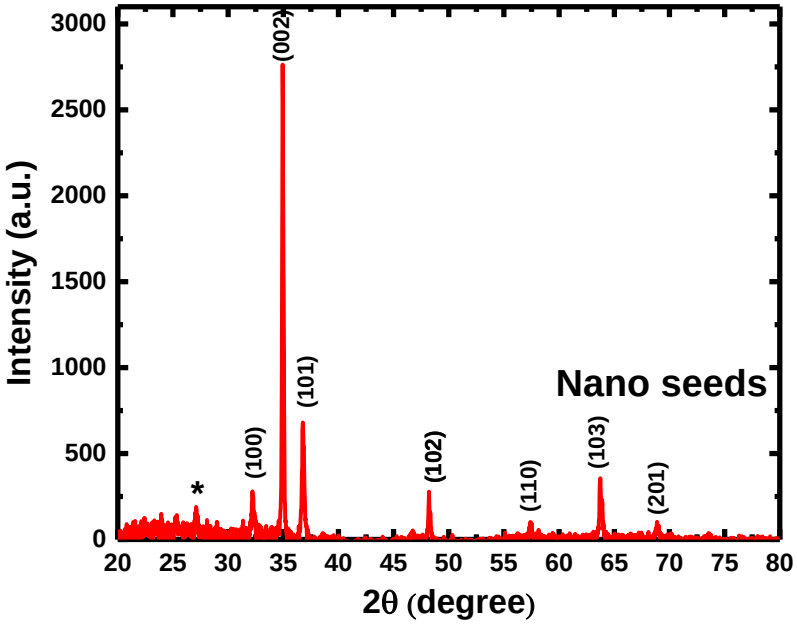

Figure 3.3: X-ray diffraction pattern for ZnO NPs.

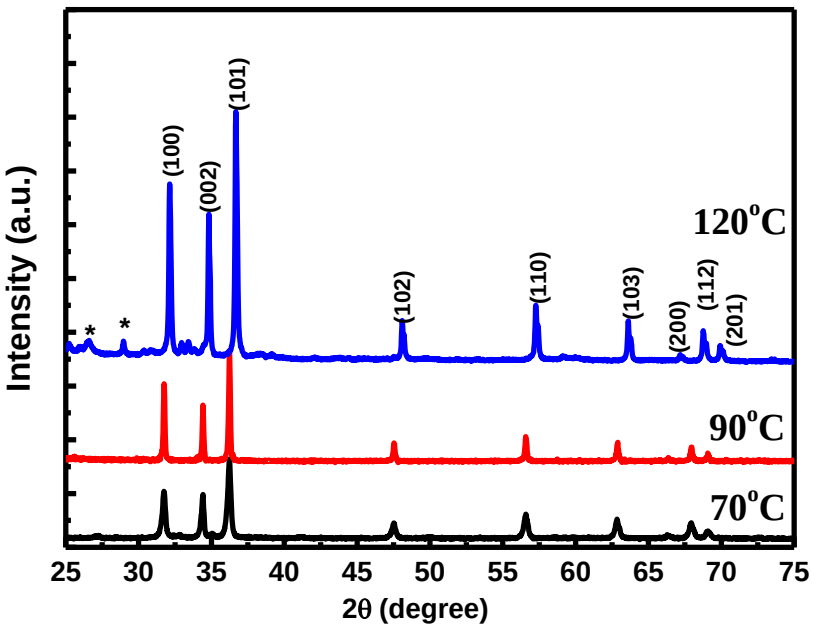

Figure 3.4: X- Ray Spectra for the samples grown at 8 h at different temperatures.

Thereafter, Scherrer equation was applied to find the crystallite size as given by:

$$\text{Crystallite Size} = \frac{0.9\lambda}{\beta\cos(\theta)} \tag{10}$$

where 'β' represents the FWHM of peak in radians, 'λ' represents the wavelength of Cu X-ray source and 'θ' represents the Braggs diffraction angle.

As the growth temperature rises, the intensity of the diffraction peaks increases, indicating an enhancement in the crystallinity of the sample. It was observed that the crystallite size increases as the temperature was raised from 70ºC to 120ºC. Because with increasing the temperature to higher value could result in a faster rate of grain growth due to the greater thermal energy accessible to the atoms in the solution. This would result in larger crystal grains in the final material. Figure 3.5 represents the variation of crystallite size with the growth temperature and it was observed that firstly the curve shows an increase, and then a saturation value to ~49 nm.

As ZnO nano seeds were utilized to reduce the strain in sample. Therefore, to estimate the values of strain, the following formula was employed:

$$\text{Strain} = \frac{\beta}{4\tan(\theta)} \tag{11}$$

Thus, it was observed that samples had very small value of strain and it reduces with subsequent increase in growth temperature from 70ºC to 90ºC and 120ºC as shown in Table 3.2. Therefore, it was deduced that proper growth of NWs on the sample helps in reduction of strain and after a particular value it gets saturated.

Table 3.1: The intensity ratio of different planes with increase in growth temperature at constant growth time.

Sr. no.	**Growth temp.**	**Growth time**	**I_{002}/I_{100}**	**I_{002}/I_{102}**	**I_{002}/I_{110}**

1	350 ºC	15 min	9.72	10.06	10.12
2	70ºC	8h	0.76	2.48	2.00
3	90ºC	8h	0.79	3.03	2.20
4	120 ºC	8h	0.84	2.48	2.55

Table 3.2: The grain size and strain for samples prepared at 70ºC, 90ºC and 120ºC.

Sr. no.	Growth temp.	Sample growth time (ZnO NW's)	Crystallite Size (nm)	Strain (x 10^{-3})
1	Seeds	15 min	28.39	0.49
2	70 ºC	8 h	28.96	0.50
3	90 ºC	8 h	49.07	0.36
4	120 ºC	8 h	49.73	0.37

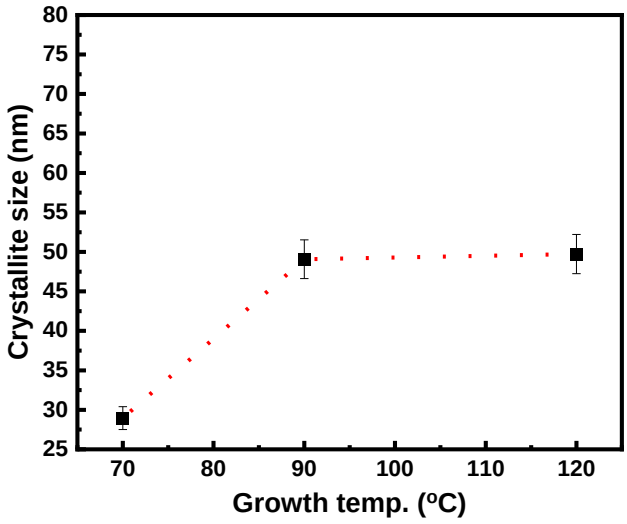

Figure 3.5: Variation of crystallite size w.r.t the growth temperature.

3.3.2 Field Emission Scanning Electron Microscopy (FESEM) images

In order to confirm the formation of NPs and NWs, the FESEM images of the samples were recorded. The FESEM images of NPs and NWs prepared through the previously described method are depicted in Figures 3.6 (a) and 3.7 (a), respectively. FESEM images clearly depicts the morphology of the synthesized samples. The dimensions of the NPs and NWs (Figures 3.6 b and 3.7 b) were estimated by using image j software. Here, the Gaussian peak fitting to the data points was used as compared to the log-normal distribution; fitted in previous chapter (Chapter-2) for NPs growth study. This is because in the former case dynamical growth of NPs were recorded within the growth solution where NPs were not in stable position. But in latter case, stable NPs/NWs were obtained from growth solution and dried for a particular time period, which therefore shows the natural distribution of particles, that is why Gaussian distribution were chosen for latter case. The Gaussian peak fitting reveals an average diameter of 26.2 nm and 367 nm for the NPs and NWs (8 h, 90ºC) respectively. The crystallite size (~ 28.36 nm) of the ZnO nano seeds is equivalent to its particle size (~ 26.2 nm). Reason for this can also be estimated from the XRD data, where it was seen that all the grains in the NPs have preferred direction along c-plane.

The broad Gaussian distribution of the NWs compared to NPs samples indicates that in the case of nano seeds sample, the uniform diameter NPs were there, but when it comes to the NWs, there is heterogeneity in diameters in the sample due to presence of both small and large sized NWs.

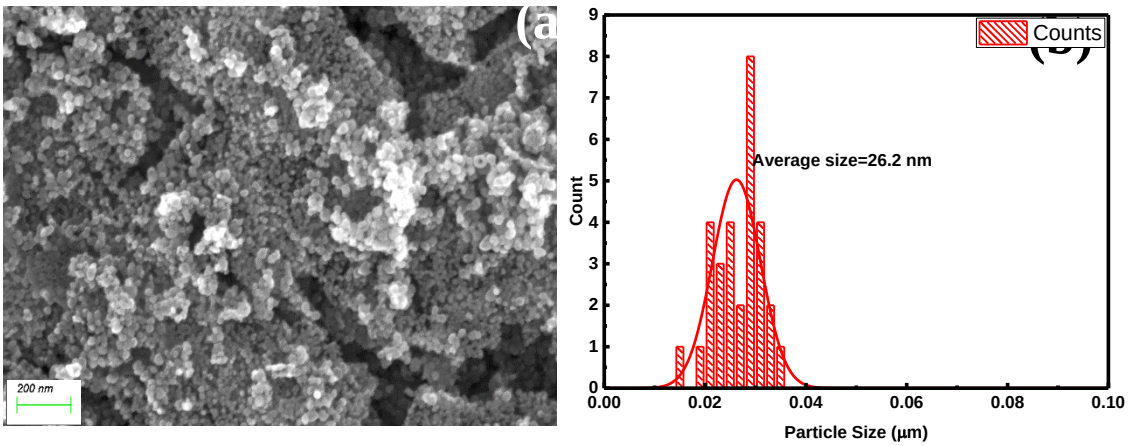

Figure 3.6: (a) FESEM image of the sample, and (b) a corresponding histogram plot with Gaussian fitting for the NPs.

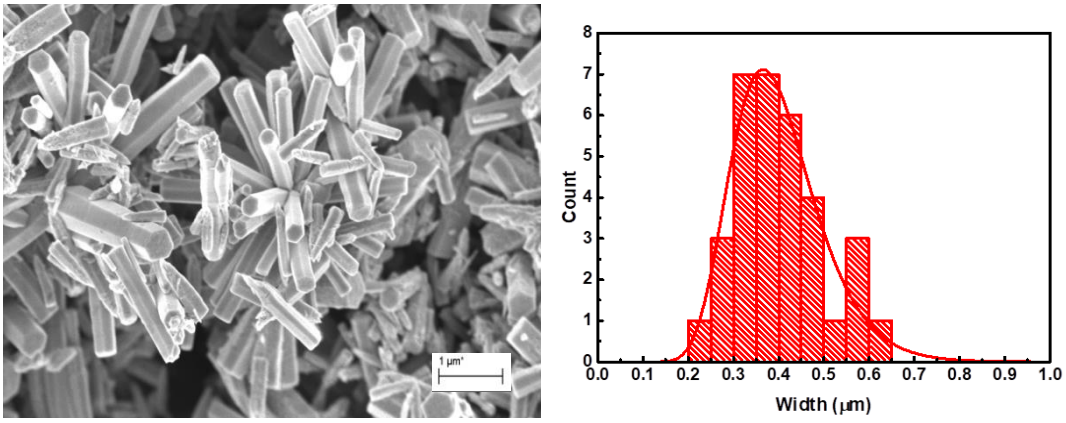

Figure 3.7: (a) FESEM image of the sample, and (b) a corresponding histogram plot with Gaussian fitting for the NWs prepared at constant growth time and temperature of 24 h and 90°C respectively.

3.3.3 Effect of temperature on the ZnO morphology

3.3.3.1 Effect of temperature on the growth of Zinc Oxide NWs

The growth rate and precursor's decomposition in a chemical reaction are noticeably influenced by the growth temperature. The correlation between the reaction rate and growth temperature can be expressed as follows:

$$k_{rea} = A \exp(-\frac{E_A}{RT}) \tag{12}$$

where 'k_{rea} represents the reaction rate, 'E_A' denotes the activation energy, 'R' represents the gas constant and 'T' signifies the growth temperature. As the 'T' increase then, reaction rate will increase exponentially. Further rate of change of reaction rate was given by equation no.-9 of Chapter-2, which signifies that the rate of change of reaction rate is the function of rate of change of growth temperature along with the exponent function. Therefore, if the temperature of the oven reaches the required temperature (70ºC, 90ºC and 120ºC) at same time interval then the reaction rate will be higher for the sample prepared at 120ºC (70ºC < 90ºC < 120ºC). Thus, the morphology of the NWs can be affected by this parameter (rate of change of reaction rate). Moreover, at low

temperature (≤70ºC), HMTA undergoes slow decomposition and thus create comparatively less concentration of OH^- ions in the solution. Therefore, slow growth along lateral and longitudinal direction takes place. But as the growth temperature increases (≥ 90ºC), the instant decomposition of HMTA occurs and fast growth of NWs take place. When the temperature is low (70°C), the HMTA precursor decomposes slowly, resulting in a slow growth rate and the formation of mixed nanostructures such as NPs and NWs in the sample. The FESEM images of the NSs are shown in Figure 3.8 (a) for 8 h. In such conditions, the mechanism of NWs growth is attributed to the orientation attachment of NPs in a specific direction, which gives rise to a chain-like morphology [126]. The orientation attachment has been occurred only along a specific direction because of the presence of capping agent (HMTA), which gives rise to growth of NWs type morphology in growth solution. The hexagonal cross-sections of the NWs are missing, possibly due to insufficient energy for decomposition and a slow growth rate of the NWs. Additionally, chemical reactions speed up if the growth solution's temperature is raised to 90º C. This particular growth temperature (90º C) provides sufficient thermal energy for the decomposition of HMTA to provide ammonia (NH_3) and hydroxide (OH^-) ions in the solution for short time interval (equation 3 and 4). This facilitates quick nucleation and growth of the NWs in both the longitudinal and transverse directions. As a result, compared to low temperature (70º C) growth, the length and width of the resultant NWs shows a uniform growth. The FESEM images of respective samples are shown in Figure 3.8 (b) at growth time of 8 h. The FESEM images depict the formation of hexagonal cross sections and somewhere flower like morphologies in the sample. The growth mechanism behind the formation of flower like morphology is the attachment of the numerous NWs to the same ZnO nucleus (Figure 3.8 b). Further, with increasing the temperature to 120º C, instant decomposition of HMTA occurs and faster consumption of ions takes place to form ZnO. This led to rapid decrease in the OH^- ions concentration and preferential attachment of the ZnO to the top of NW, which lead to the growth of broad base and sharp tip of the NW or pencil tip type morphology of the NWs: Figure 3.9. However, the NWs begin to become hollow with broken ends at this elevated temperature (Figure 3.9). The broken structure of the NWs near the tips (Figure 3.8 marked in yellow circle) causes the interior of the NWs to become hollow. Therefore, Figure 3.8 was shown to demonstrate that the NW starts getting hollow after this particular growth time. This might be due to dissolution effects, which begin to predominate and the growth of the NWs reaches its equilibrium stage [127].

3.3.3.2 Impact of temperature variations on diameter distributions of NWs

The distribution of nanowires (NWs) becomes narrower as the growth solution temperature rises from 70°C to 120°C shown in Figure 3.8. Additionally, it has been reported in the literature that an increase in the growth temperature results in a narrower distribution of NW's diameters [128]. This is because, an increase in temperature leads to faster growth of smaller NWs to their saturation value, resulting in a narrower distribution. The diameter of the NWs at varied temperature conditions and at fixed growth times is shown in Table 3.3. The average diameter of the NWs was approximately same for the samples prepared under 70ºC and 90ºC growth temperatures, but shows a mild decrease when temperature further increases to 120 ºC. No significant change in the diameter of 70ºC and 90ºC was observed, because here OH^- ions uniformly attaches at the lateral and longitudinal surfaces of NWs and growth temperature here leads to control the cross section of the NWs. But a decrease in the average diameter of the NW was observed with further increase in the growth temperature. Because at higher temperature pencil tip type morphology formed with broad base and sharp tip and average length of NW increases at higher rate compared to its diameter, which leads to decrease the overall/average diameter of the NWs.

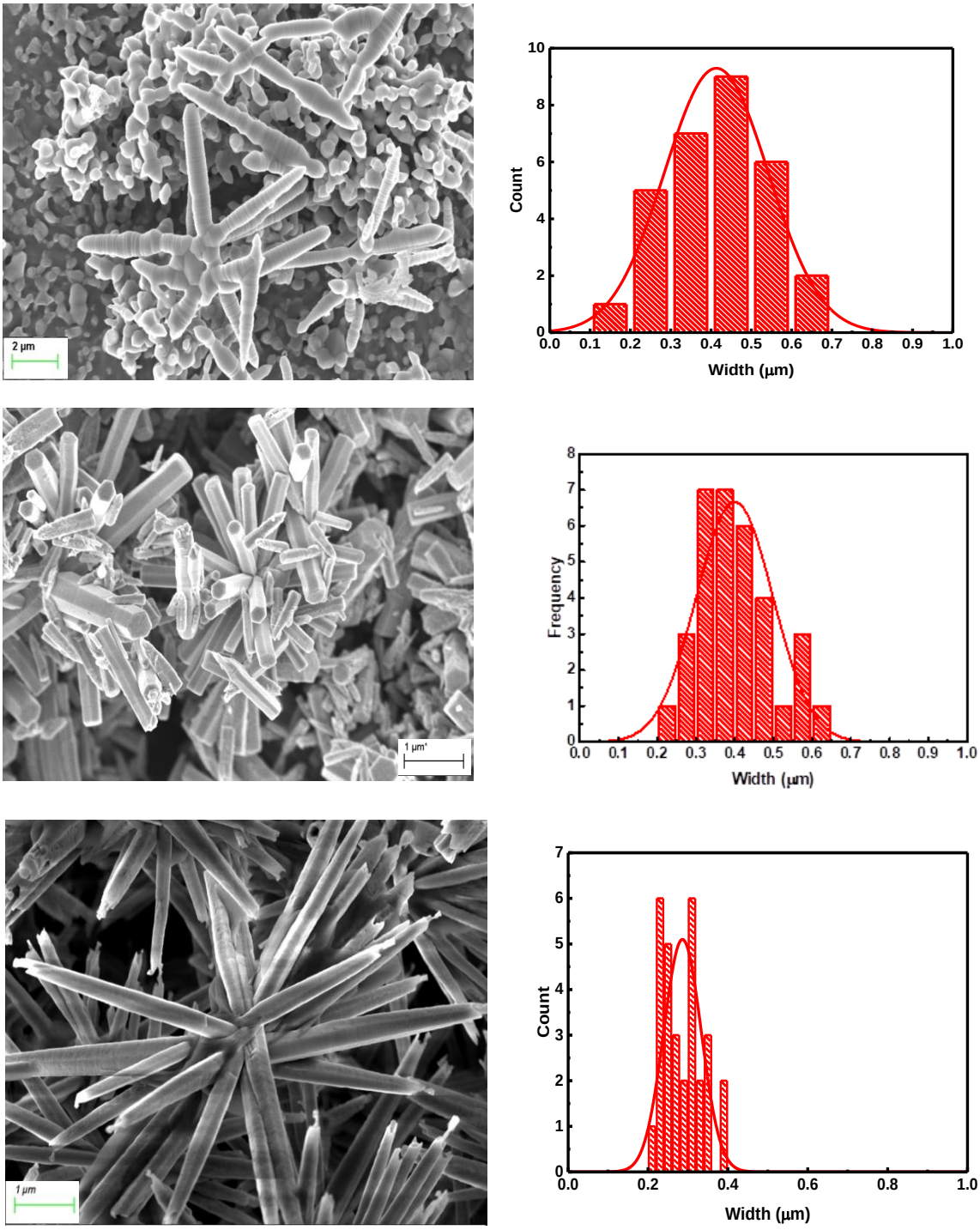

Figure 3.8: FESEM images of nanowires along with their diameter distributions growth temperature of 70℃, 90℃ and 120℃ for growth time of 8 hours.

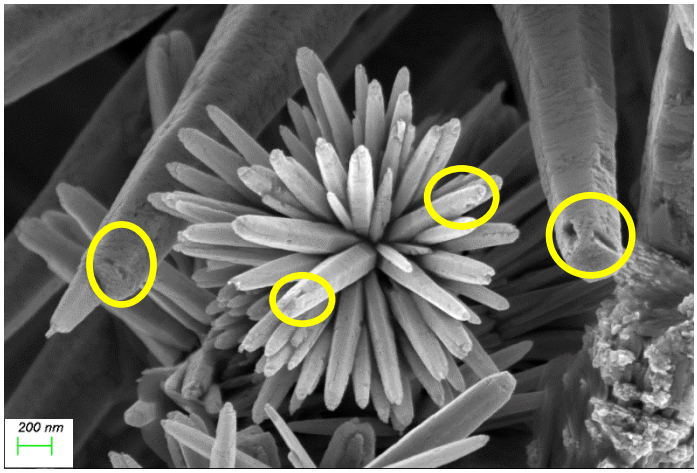

Figure 3.9: ZnO flower type morphology prepared at growth time 4 h by maintaining growth temperature of 120℃.

Table 3.3: Impact of growth temperature on the diameters of the NWs.

Sr. no.	Sample	Width (nm)
1	Particles + NWs (70ºC, 8 h)	364 nm
2	Hexagonal NWs (90ºC, 8 h)	367 nm
3	Broken NWs (120ºC, 8 h)	278 nm

3.3.4 UV-vis spectroscopy

3.3.4.1 ZnO Nanoparticles (NPs)

Figure 3.10 represents the absorbance spectra and corresponding Tauc plot for ZnO nano seeds. The calculation of the band gap was performed using Equations (13) and provided below:

$$\alpha h\upsilon = A(h\upsilon - E_g)^{1/2} \qquad \text{if } h\upsilon \geq E_g \tag{13}$$

The symbols used in Equations (8) have their standard meanings.

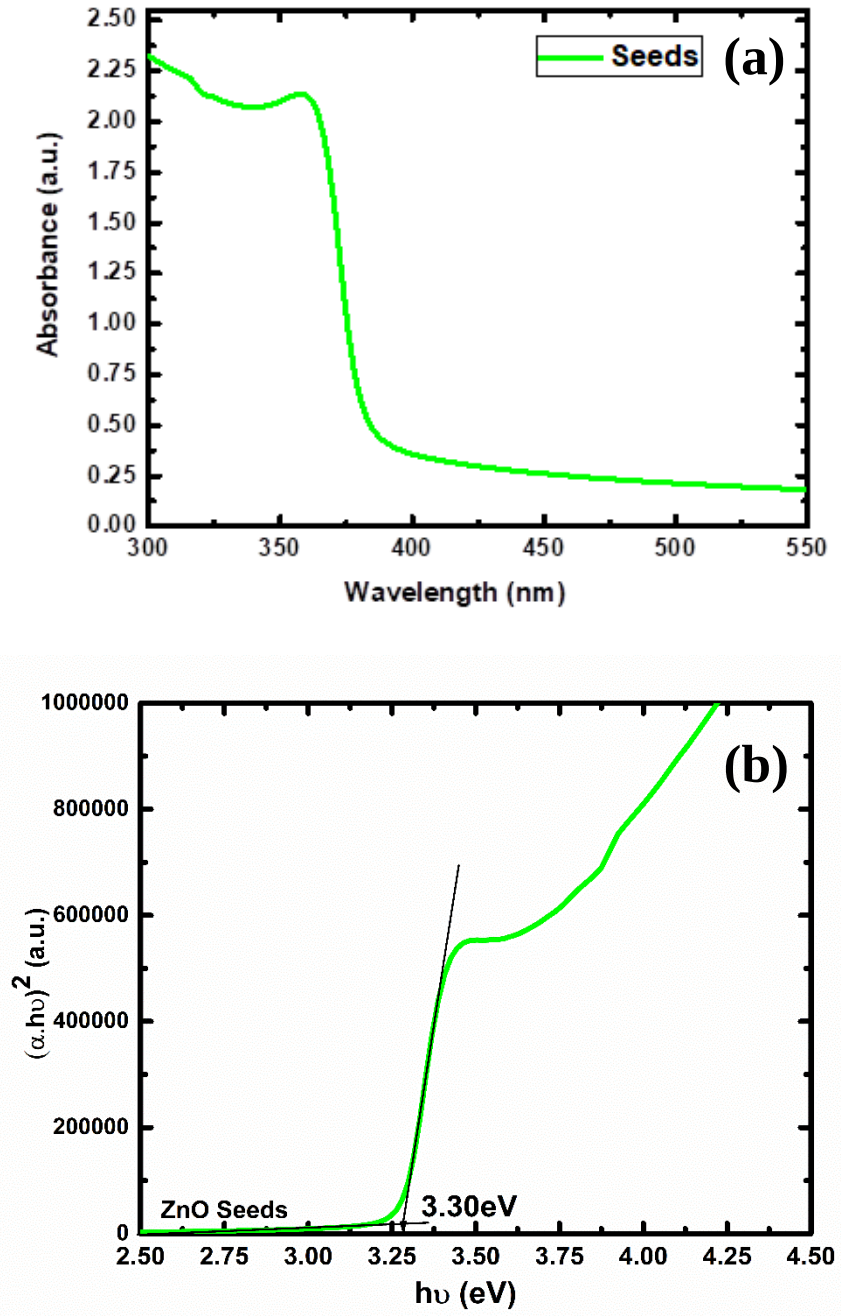

Figure 3.10: (a) Absorbance spectra and Tauc plot (b) representation for the ZnO nano seeds.

The optical band gap value obtained for the nano seeds is 3.30 eV. Thereafter, the broadening of the energy gap in semiconductors is often caused by the presence of defects and impurities within the crystal structure of the material [129].

3.3.4.2 ZnO Nanowires (NWs)

Figure 3.11 displays the absorbance spectra of the NWs synthesized for 8 hours at various growth temperatures, namely 70°C, 90°C, and 120°C. The absorbance offset curve of the absorbance spectra was found to be significantly affected by temperature. Specifically, the sample prepared at a temperature of 90°C displayed the steepest slope on the offset side of its absorbance curve, suggesting that it possessed superior crystal quality compared to samples prepared at other temperatures. Additionally, it does not contain any broad distribution. Optical band gap values were determined for all samples using Tauc plots and shown in Table 3.4. From Table 3.4, it was observed that band gap values show an increase in band gap values with increase in the growth temperature from 3.11 to 3.28 eV. Further Figure 3.12 represents cumulative plot.

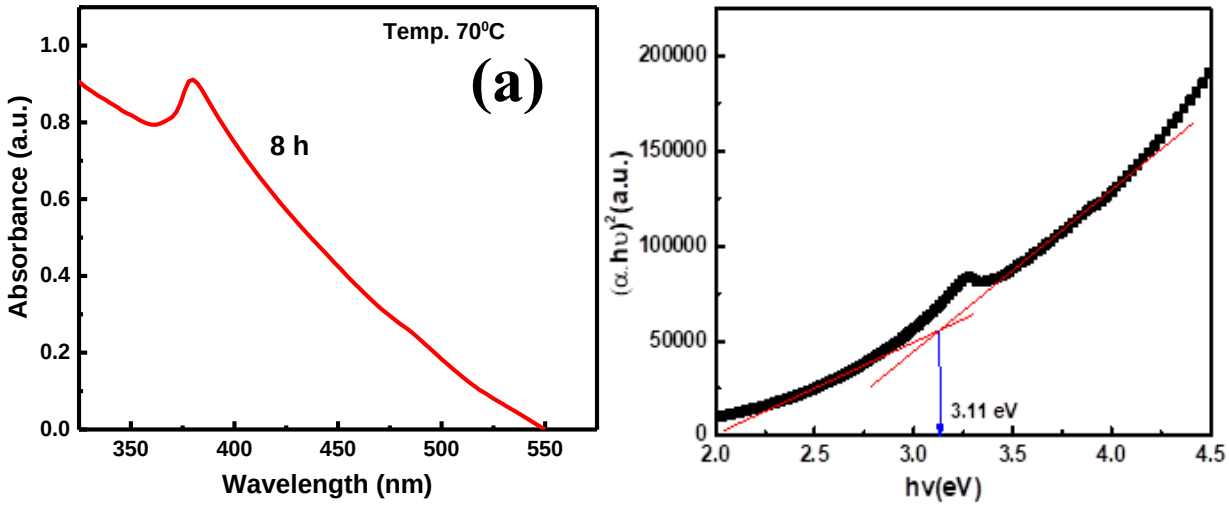

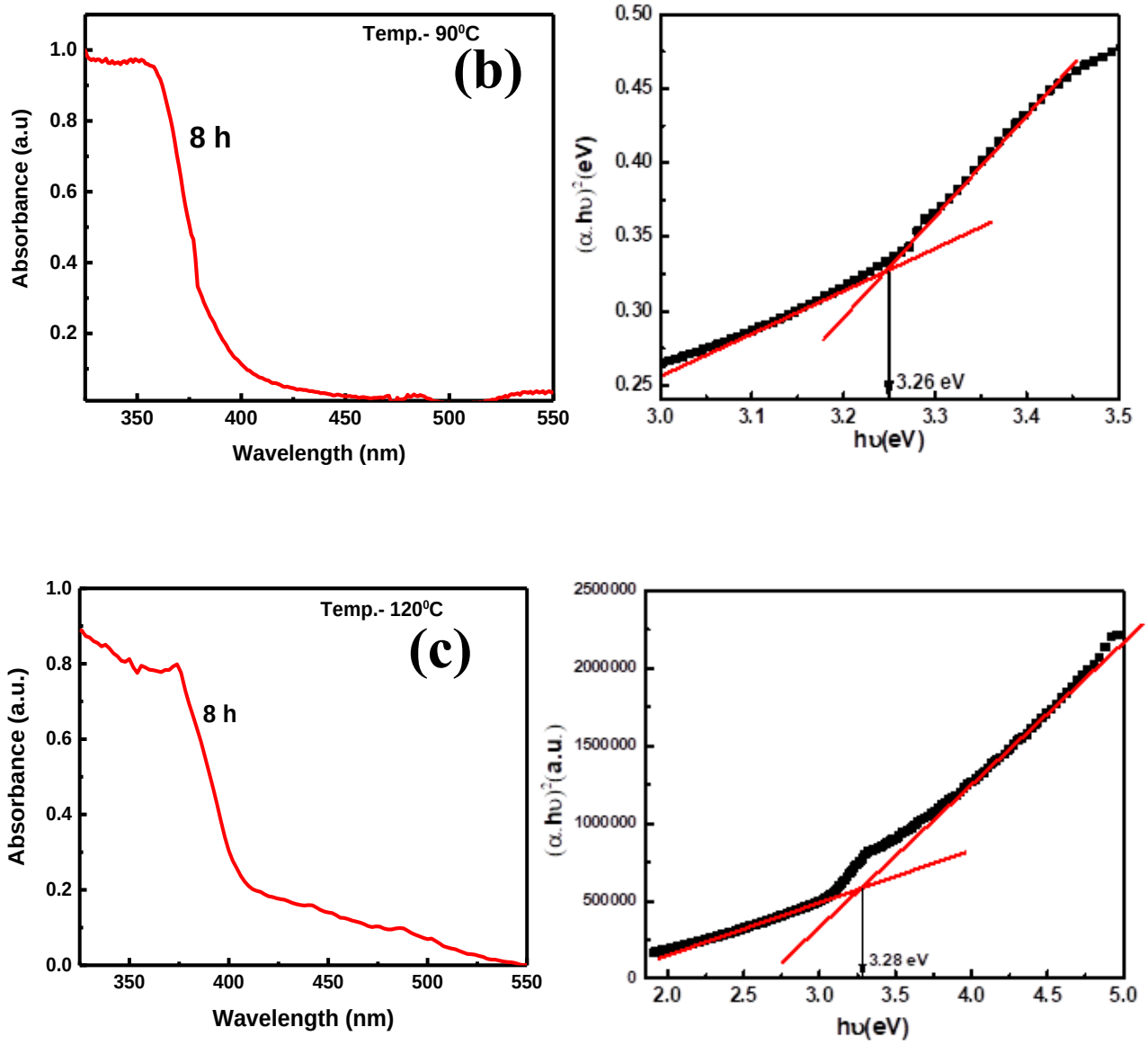

Figure 3.11: Absorbance spectra for the ZnO NSs at (a) 70º, (b) 90ºC and (c) 120ºC.

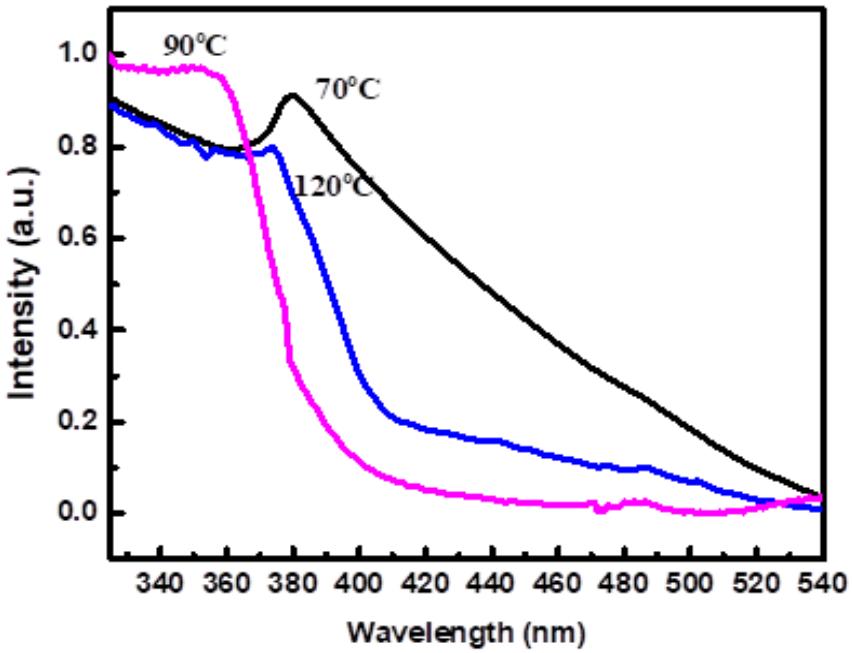

Figure 3.12: A comparison of the absorbance spectra for samples synthesized at varying growth temperatures.

Table 3.4: Band gap values as function of growth temperature.

Sr. no.	Growth temp. (ºC)	Growth time (h)	Band gap (eV)
1	70	8	3.11
2	90	8	3.26
3	120	8	3.28

3.3.4.3 PL-emission studies ($h\nu \geq E_g$)

PL-emission spectra of the samples were recorded to identify various defect states within the band gap. Figures 3.13 a, 3.13 b1, 3.13 b2, and 3.13 b3 show the PL-emission spectra for the nano seeds and NWs prepared at 70º C, 90º C, and 120º C, respectively (growth time 8 h). The emission spectra tend to exhibit emissions in both the ultra-violet and visible spectral region for excitation energies greater than the band gap energy **($h\nu \geq E_g$)**. When excited with a wavelength of 350 nm, the emission spectral peaks were detected at ~400 nm, ~425.09 nm, ~450.30 nm, ~470.16 nm, ~492.26 nm and ~536.87 nm. Thereafter, it was also observed that the UV defect related emission is significantly stronger than visible defect related emissions. The emission in the UV region is referred to as the Near Band Edge (NBE) emission. The de convolution of the spectra was carried out for clear visualization of the peaks. Schematic representation of the various possible defect states present within the band gap are represented in Figure 3.13 (c). In the schematic representation, energies of Zn interstitial, Zn interstitial complexes with oxygen vacancy and oxygen vacancy within energy band gap were shown, as the peaks of respective defects were observed in all the samples.

Additionally, it was noted that all of the samples prepared at different growth temperatures (70ºC, 90ºC and 120ºC) exhibited the same number of defect states within their band gap. The only difference among them was the intensity ratio of the defect states *w.r.t* their NBE emission peak. Table 3.5 shows the intensity ratios for all the prepared samples. The intensity ratio of the Zn_i defect peak was found to be maximum in the sample synthesized at 120ºC, whereas the sample prepared at 70ºC exhibited the highest intensity for the Zn complex/cluster peak. The sample prepared at 90ºC exhibits comparatively less defect intensity ratios and shows better crystal quality. Therefore, the subsequent section of this study provides a comprehensive analysis of the sample prepared at 90ºC, and results are compared with those of samples prepared at other temperatures.

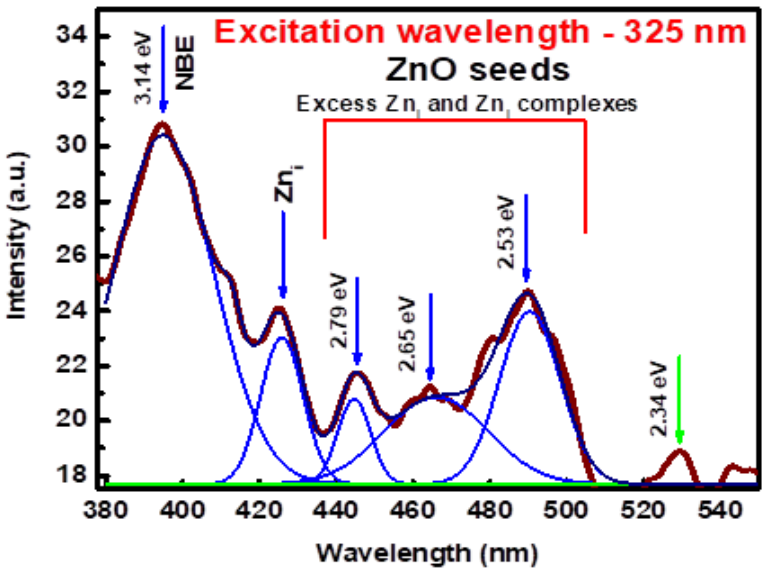

Figure 3.13a: PL-emission spectra for ZnO nano seeds.

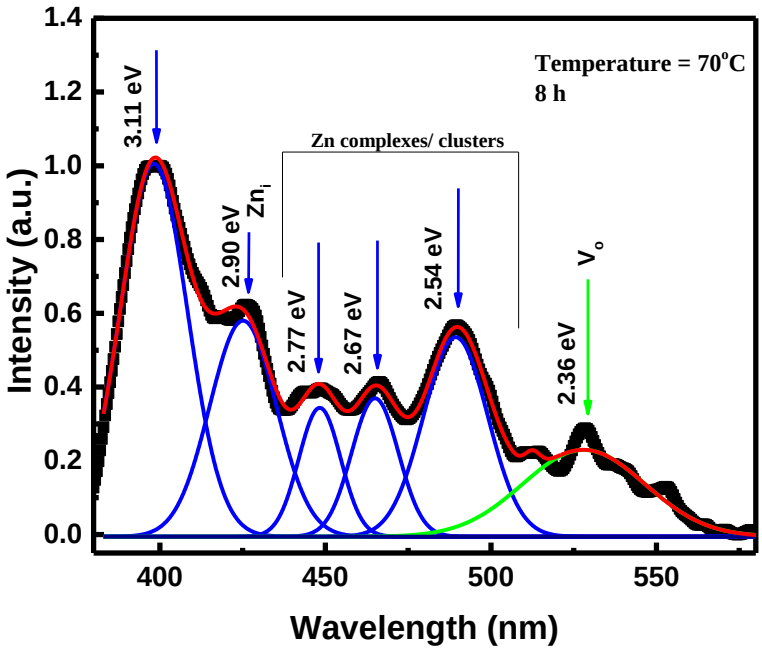

Figure 3.13b1: PL-emission spectra of ZnO NSs produced at 70ºC growth temperature.

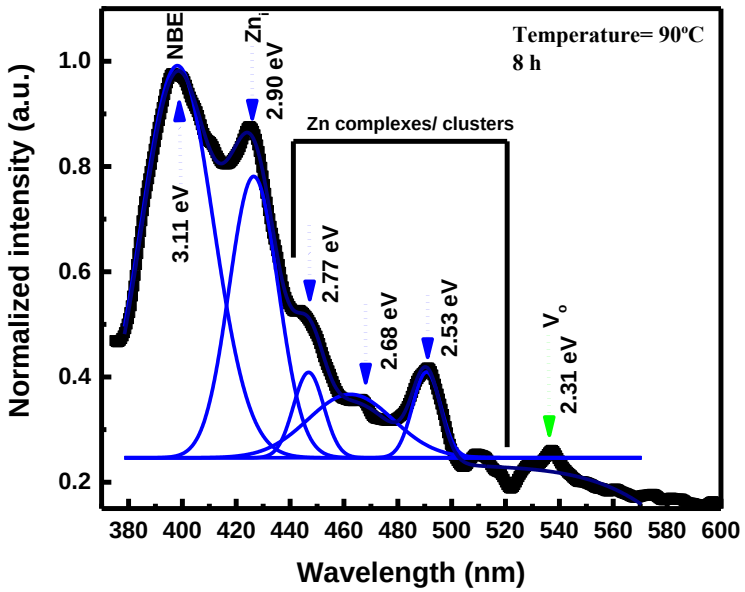

Figure 3.13b2: PL-emission spectra of ZnO NSs produced at 90ºC growth temperature.

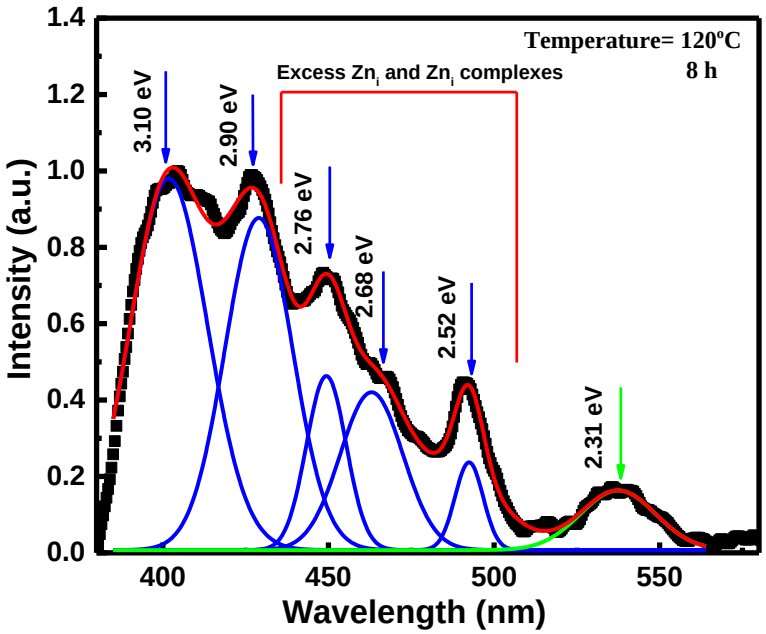

Figure 3.13b3: PL-emission spectra of ZnO NSs produced at 120ºC growth temperature.

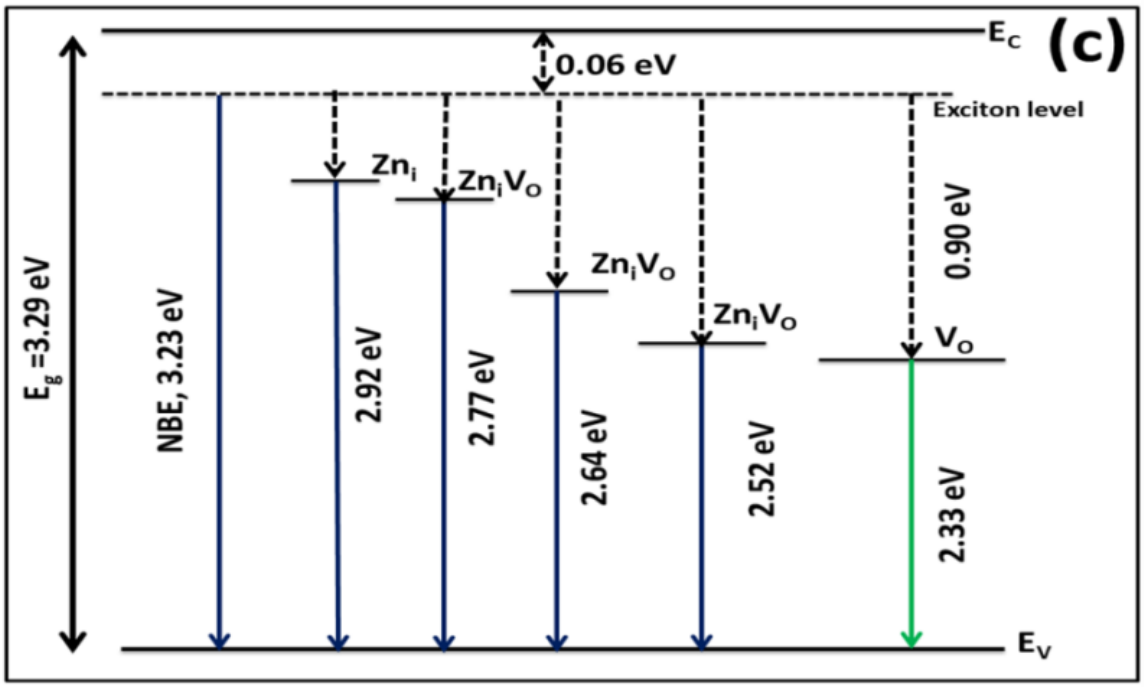

Figure 3.13c: Schematic representation various defect states present within band gap of ZnO.

Table 3.5: Intensity ratio of defect related peaks with respect to the NBE emission peaks at different growth temperature.

Sr. no.	Growth temp. (ºC)	Growth time (h)	Peak Area ~425 nm	$\frac{I_{Zni}}{I_{NBE}}$	$\frac{I_{\sim 490}}{I_{NBE}}$	$\frac{I_{\sim 536}}{I_{NBE}}$
1	70	8	14.75	0.81	0.77	0.64
2	90	8	12.19	0.88	0.42	0.27
3	120	8	22.24	0.98	0.61	0.44

3.4 CONCLUSIONS

This chapter is dedicated to the seed mediated growth of ZnO NWs via simple chemical method at varied growth temperatures (70º C, 90º C and 120º C) at constant growth time of 8h. The conclusions of this chapter given as:

Table 3.6: Cumulative data for all the samples prepared at different growth temperatures.

Sr. no.	Sample	Average size (nm)	Grain size (nm)	Morphology	Optical band gap (eV)	Peak Area ~425 nm	$\frac{I_{Zni}}{I_{NBE}}$	$\frac{I_{\sim 536}}{I_{NBE}}$
1	Nano seeds	26	28	Spherical particles	3.30	74.57	0.78	0.61
2	NWs (70ºC)	364	28.96	Chain like	3.11	14.75	0.81	0.64
3	NWs (90ºC)	367	49.07	Hexagonal wires	3.26	12.19	0.88	0.27
4	NWs (120ºC)	278	49.73	Pencil like	3.28	22.24	0.98	0.44

- With increase in the growth temperature, the crystallinity of the samples observed to increased.
- The size and strain of the NSs' crystallites were significantly affected by the growth temperature. As the temperature increased, the crystallite size increased while the strain in the sample decreased.
- Slight variation in temperatures leads to significant change in the final morphology of ZnO NSs such as broken and hollow tips of NWs obtained at 120º C (8 h), hexagonal cross-section at 90ºC and chain like morphology at 70ºC.

- Diameter distribution getting narrower with the growth temperature.
- Absorption studies shows that the temperature had a significant influence on the optical band gap values. The optical band gap values increased from 3.11 to 3.28eV, with increase in the growth temperature.
- The formation and presence of defect states within the band gap, significantly impacted by the temperature of the growth solution. From the present work, it was concluded that 90°C is the perfect growth temperature to prepare NWs with minimum number of defect state intensities.

CHAPTER-4

EFFECT OF GROWTH TIME ON THE MORPHOLOGICAL AND OPTICAL PROPERTIES OF ZnO NWs

4.1 INTRODUCTION

In the previous chapter the influence of growth temperature on both the morphology and optical characteristics of ZnO nanowires were investigated, while maintaining a constant growth duration. Further, this chapter expands the study by investigating the effect of growth time on the morphology and optical properties of NWs at a fixed growth temperature. Because as growth time progresses, various phenomena such as aging, crystal growth and coalescence can occur, leading to alterations in the properties and morphology of ZnO nanowires.

A number of studies have investigated the synthesis of ZnO nanowires and its dependence on growth time. Amin et al. discovered that longer growth times resulted in larger aspect ratios of the nanowires, while Tian et al. concluded that longer growth times improved the alignment quality and density of NWs, along with an increase in their dimensions [52], [130]. In addition to this, the change in morphology from tower like to flat top structured like rods were also observed in his work [2]. Zhitao et al. observed an improvement in alignment and density of NWs with growth time, but no change in morphology [131]. Wilson et al. studied theoretically the relationship between the size (or aspect ratio) and stable thermodynamic shape of ZnO semiconductor material, as well as the role of surface and edge energies, using density functional theory [132]. Demes mathematically studied the mechanism of growth of NWs from NPs using the concept of Gibbs free energy [133]. Chauhan et al. studied the impact of irradiations on its optical band gap value [134].

The non-uniform distribution of defects and the size of nanomaterials significantly affect their electrical and optical properties [135]. A decrease in the diameter of nanowires typically results in a blue shift in their optical band gap due to quantum confinement. However, for larger NWs, surface effects were responsible to cause the blue shift. For instance, the surface resonance effect was found by Chen et al. to cause a blue shift in the cathodoluminescence (CL) emission spectra of ZnO nanorods (NRs) with diameters of up to 620 nm [136]. Moreover, a blue shift in the CL-emission spectrum of a single pencil-type ZnO NW was observed at various positions with diameters ranging from 50 nm to 700 nm, which was attributed to the Burstein-Moss phenomenon [137].

Another surface phenomenon which can lead to the change in electrical properties of the material is the band bending phenomena. When a semiconductor is brought into contact with another material, such as a metal or an insulator, the electronic properties at the interface gets affected. In particular, the energy bands near the interface can bend due to the differences in the electron affinity and work function of the two materials. The bending of energy bands is called band bending and it creates an electric field across the interface. This electric field can affect the movement of charge carriers across the interface, and it is an important factor in the performance of many electronic devices such as transistors and solar cells. Absorption of electropositive element at the surface of ZnO arises downward band bending, whereas electronegative element arises upward band bending [138]. Further, the amount of band bending depends on the properties of the materials at the interface, such as their work functions and electron affinities, as well as the doping level and the temperature of the semiconductor material. The band bending phenomenon induced by the depletion layer/accumulation layer on the semiconductor (ZnO NW's) surface, was reported to modify the green region of the photoluminescence (PL)-emission spectra [139].

Therefore, in this chapter, the optical characteristics of chemically synthesized ZnO NWs were investigated using absorbance, PL-emission, Raman spectra and sub-band gap excitation measurements for different growth times and temperature conditions. An unanticipated variation in the PL-NBE emission spectra were observed and explained by introducing the band bending concept. Raman spectra were used to measure the vibrational modes of various atoms and thus determine the identity of the sample [140]–[143].

4.2 EXPERIMENTAL DETAILS

ZnO NWs were prepared by the simple chemical approach described in Chapter-3. The synthesis process involves the precursors with the ratio $Zn(NO_3)_2.6H_2O : (CH_2)_6N_4$ = 1:1. This indicates that the concentration of NH^{4+} and OH^- ions is slightly higher than that of Zn^{2+} ions (because for balanced reaction, $Zn(NO_3)_2.6H_2O : (CH_2)_6N_4$ = 2:1). This can be understood by following equation:

$$Zn(NO_3)_2.6H_2O \rightarrow Zn(NO_3)_2 + 6H_2O \quad (1)$$

$$Zn(NO_3)_2 \rightarrow Zn^{2+} + 2NO_3^- \quad (2)$$

The decomposition of HMTA is given below:

$$(CH_2)_6N_4 + 6H_2O \rightarrow 6HCHO + 4NH_3 \quad (3)$$

$$4NH_3 + 4H_2O \rightarrow 4NH_4^+ + 4OH^- \quad (4)$$

$$2OH^- + Zn^{2+} \rightarrow ZnO(s) + H_2O \quad (5)$$

Thus, from equation (4), it was clear that $4NH_4^+$ and $4OH^-$ were produced in the solution, out of which only 2 moles of OH^- required to react with one mole of Zn^{2+} to produce 1 mole of ZnO (equation 5). Therefore $2OH^-$ and $4NH_4^+$ remains in the solution. The pH of the solution, which is necessary for NW growth, is maintained by these excess NH^{4+} and OH^- ions.

Thereafter, NWs were grown by varying the growth time at fixed temperature conditions (90ºC). Their optical properties were investigated in following sections.

4.2.1 Characterizations

The absorbance spectra of the samples were obtained using a Perkin Elmer Lambda 750 UV-visible-NIR spectrophotometer, over the wavelength range of 300 nm to 550 nm. The shape and particle's diameter distribution of the synthesized nanowires were visualized using the Field Emission Scanning Electron Microscopy (FESEM-Supra 55, Carl Zeiss (Germany)) technique. Photoluminescence (PL) measurements were conducted using a Perkin Elmer LS-55 spectrophotometer, where Xenon lamp serves as the excitation source. Photoluminescence (PL) data collections were performed by exciting the sample using energies above and below its band gap and resulting emission spectra recorded over a wavelength range of 350-700 nm using the same instrument. Further, Horiba LabRam spectrometer was utilized to record a Raman spectrum in wavenumber range of 90 cm^{-1}-1500 cm^{-1}, which is significant for examining surface defects within a sample by providing information about the vibrational modes of various atoms.

4.3 RESULTS AND DISCUSSION

4.3.1 Morphological evolution with growth time

Figure 4.1 (a-f) depicts the FESEM images along with their diameter distributions of the synthesized samples for the growth times of 2, 4, 8, 16, 20 and 24 h. All the images confirm the formation of NWs in the sample. The results showed that as the growth duration progressed, the diameter distribution of the NWs became wider, ranging from 0.0449 µm to 0.1879 µm. Here, the Gaussian distribution was utilized to fit the histogram data, by using following Gaussian relation:

$$y = \frac{A\sqrt{2}}{w\sqrt{\pi}} \exp\left(-2\frac{(x - x_c)^2}{w^2}\right) \qquad (6)$$

Where '*y'* represents the counts/frequency, '*A'* is the constant; 'x_c*'* is the center/mean of the curve and '*w'* represents the standard deviation. Here, '*w'* increases with the progression of growth duration from 0.0449 µm to 0.1879 µm, which physically represents the heterogeneity in the diameter values. In simple words, with increase in the growth time, the formation of new nanowires and the enlargement of pre-existing NWs within the sample have been occurred, due to which broadening in the peak was recoded. In addition to this, value of 'x_c*'* is also increasing which simply represents the growth of NW's diameter with the progression of growth durations. For growth duration ranging from 2 h to 24 h, the diameter of the wires varies as 170, 280, 399, 390, 411 and 573 nm, while the lengths vary as 0.52, 1.34, 1.95, 2.26, 2.42 and 4.47 µm respectively. The longest and widest NWs were recorded for 24 h growth time with average length of 4.476 µm and width of 0.5738 µm, while the shortest and narrowest NWs were recorded for 2 h growth time with average length of 0.516 µm and width of 0.170 µm. Despite the use of HMTA, the diameters of NWs are continually increasing during growth. This is because, as the time progresses, the ammonium and hydroxide ions gets consumed, resulting in weak bonding of HMTA at the lateral surface. The variation of diameter with the progression of growth time is shown in Table 4.1. The size (width) of the NWs was found to satisfy the power law equation $d = d_0 t^n$, where n = 1/3 (Figure 4.2). This demonstrates that the diffusion limited growth dominates the growth of NW's diameter with growth time. Figure 4.3 represents the length, width and aspect ratio variations with the growth durations. Additionally, an alteration in morphology from hexagonal to cylindrical cross-section

was observed with an increase in growth time (as shown in Figure 4.1(e-f)). It may be due to uniform diffusion of Zn interstitials towards the surface of NWs with the growth time, which leads to the smooth and cylindrical cross sections.

It was also observed that with the progression of growth time, the edges/boundaries of the wires are getting intense. The observed contrast in the FESEM images is likely caused by the metallic nature of the NWs' edges, which leads to generate more secondary charge carriers ***'e$^-$'*** and resulting in brighter boundary walls.

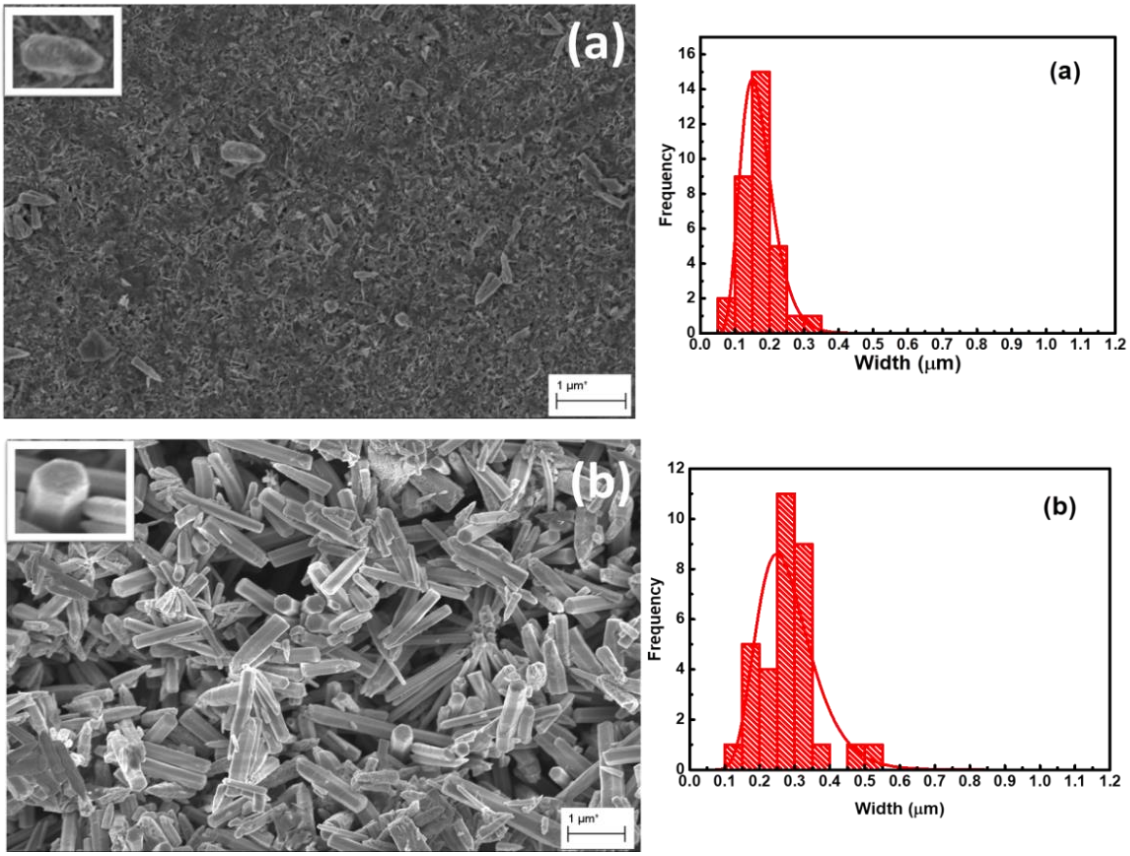

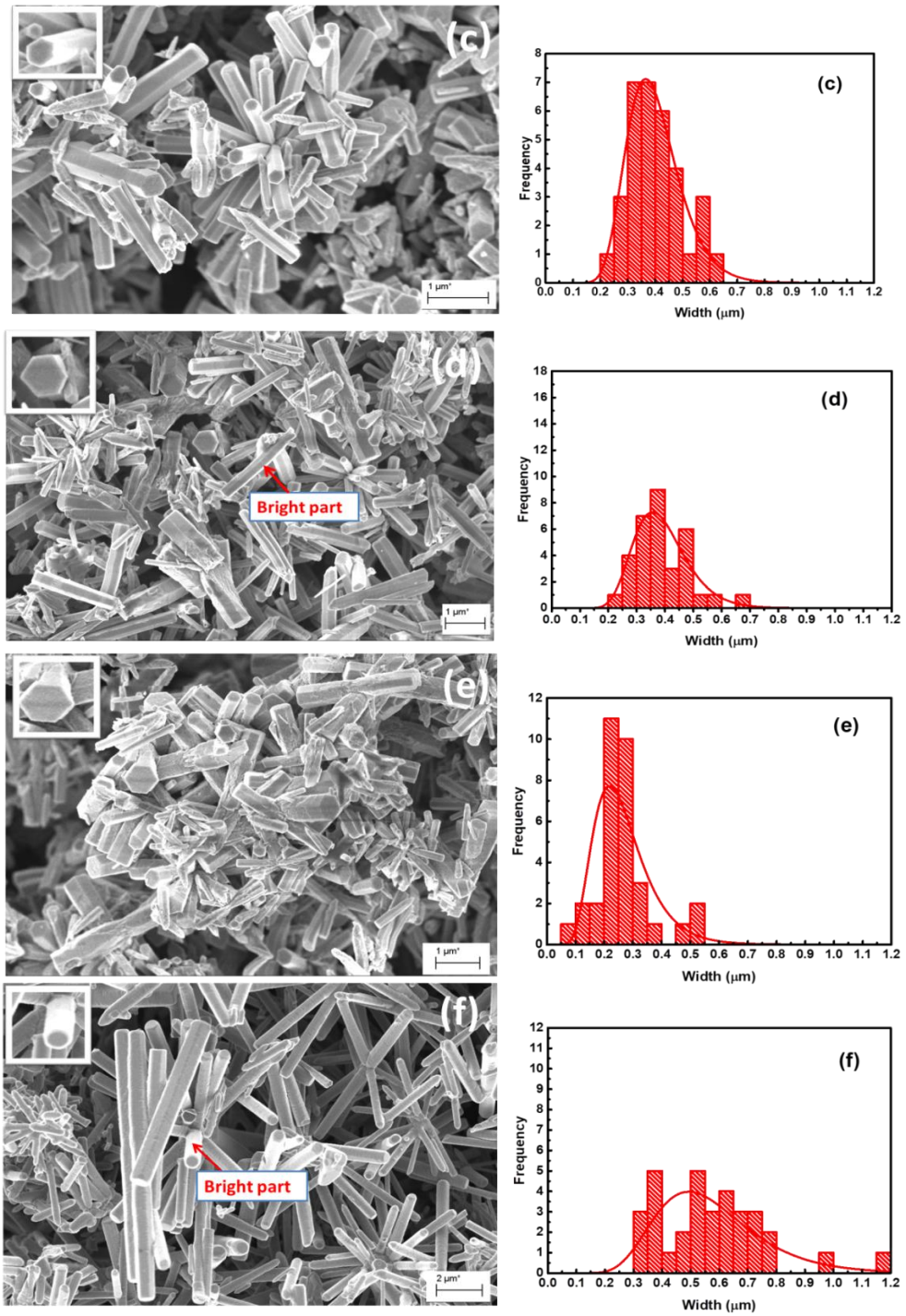

Figure 4.1 (a-f): Field-emission scanning electron microscope (FESEM) images depict samples grown at various time intervals, including 2, 4, 8, 16, 20, and 24 hours. The inset image provides a magnified view of a single nanowire, while the adjacent images demonstrate the width distribution of the nanowires.

Table 4.1: Nanowires average diameter and morphology as a function of growth time (90°C).

Sr. no.	Growth time (h)	Morphology	Diameter (nm)
1	2	Hexagonal	170
2	4	Hexagonal	280
3	8	Hexagonal	399
4	16	Hexagonal	390
5	20	Hexagonal	411
6	24	Cylindrical	573

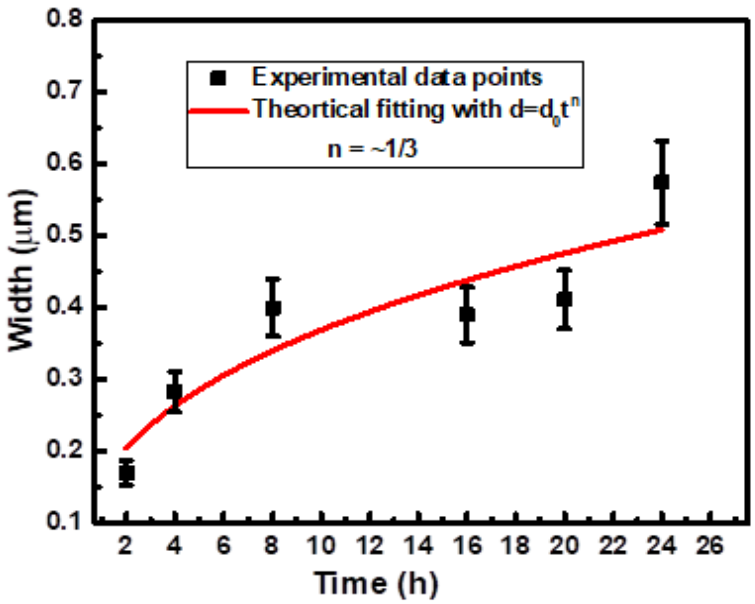

Figure 4.2: Diameter variation of NWs with the effect of growth duration.

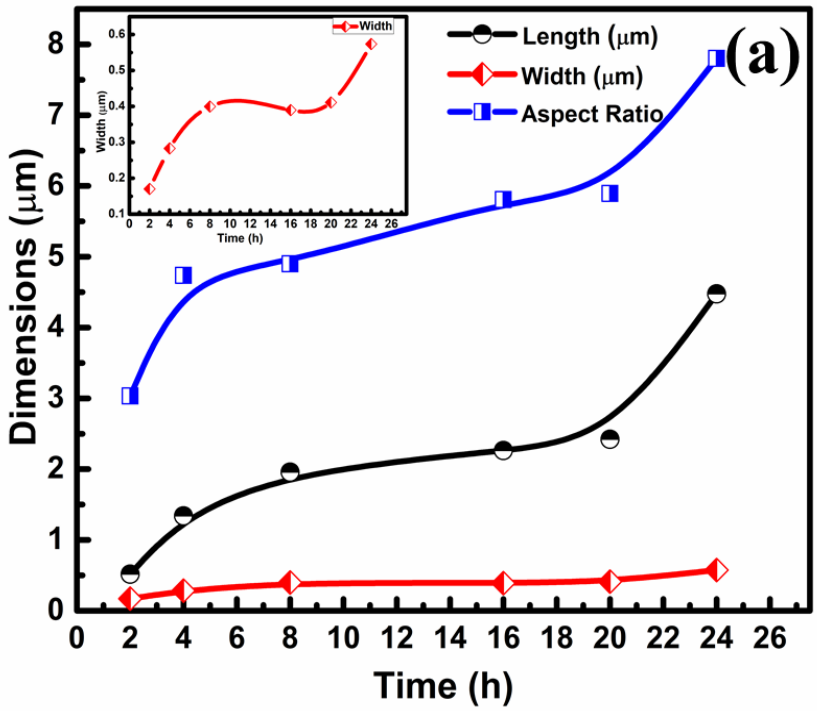

Figure 4.3: Changes in the length, diameter and aspect ratio of the NWs as a function of growth durations.

Thereafter, NWs morphology was also recorded at higher growth times up to 48 h and slight increase in the length and width was observed as the time is increased as shown in Figure 4.4 and 4.5.

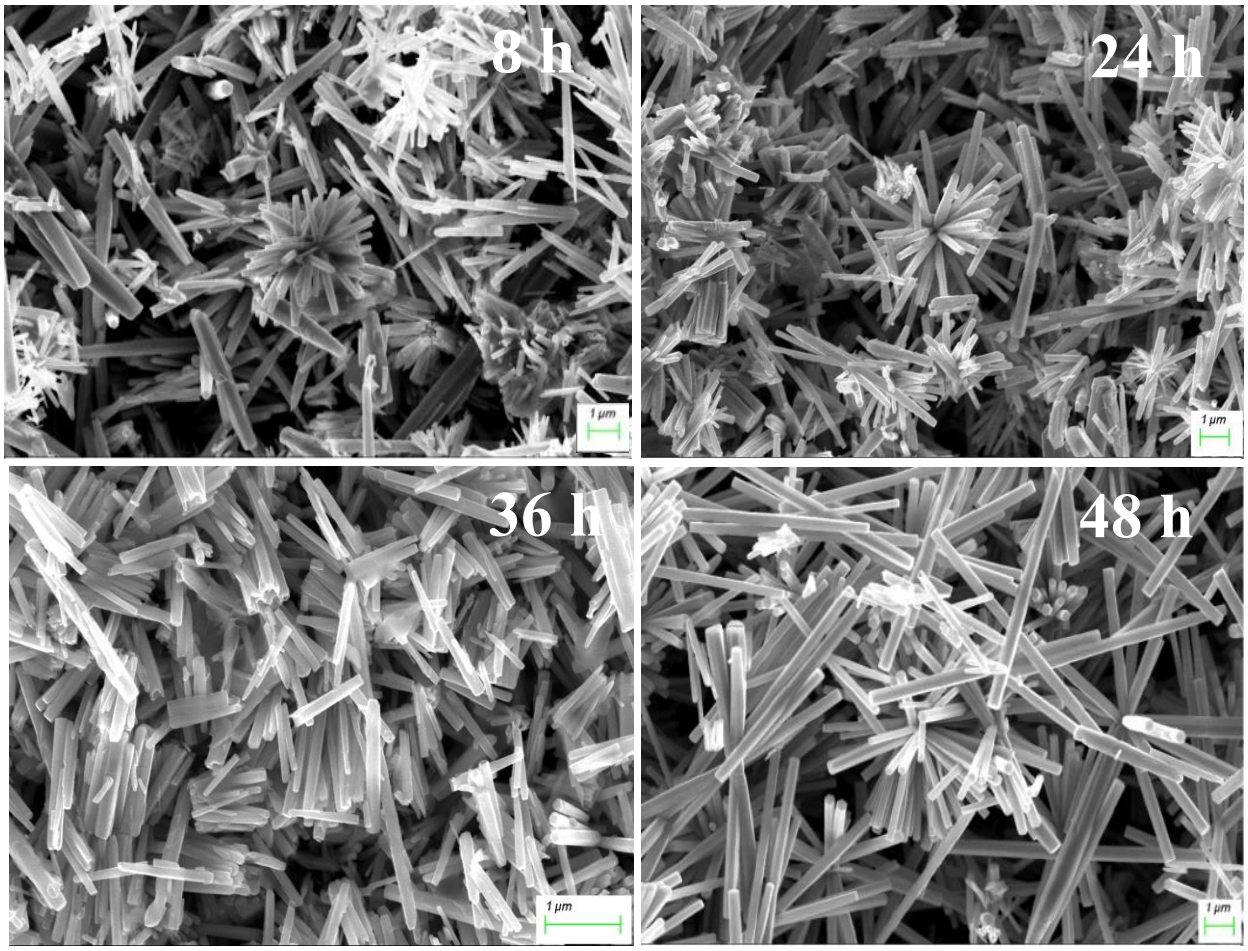

Figure 4.4: FESEM pictures of the sample prepared at higher growth times (90º C).

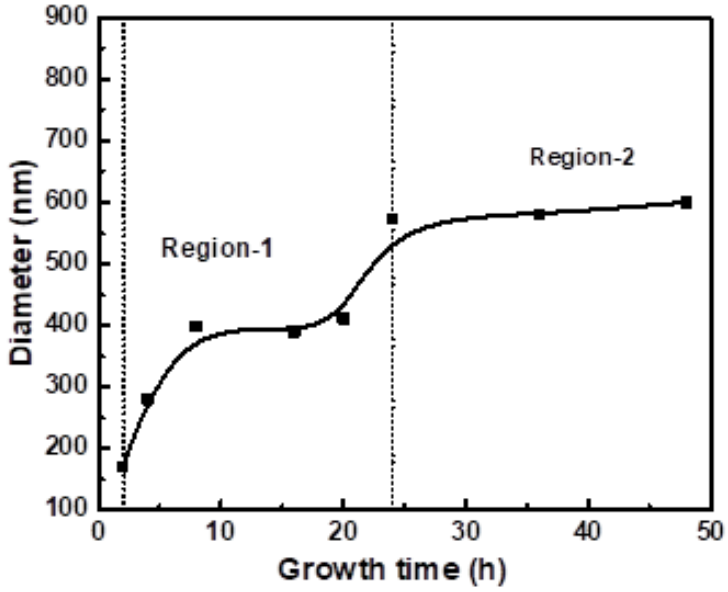

Figure 4.5: Impact of longer growth durations on the dimensions of the nanowires.

4.3.2 Field Emission Scanning Electron Microscopy image analysis

The FESEM images for each growth times were shown in previous Section 4.3.1. Here, detailed analysis of the FESEM images were conducted. It was observed from the FESEM images that with the increase in the growth time, the diameter of NWs increases. The intensity profile for the ZnO nanowires at each growth durations were represented in Figure 4.6. The intensity profile demonstrates that the width of the intense boundaries of NWs expands as the growth time progresses, and it also suggests an increase in diameter over time. Thereafter, intensity ratio (I_b/I_s, I_b= bulk intensity at the center of NW, I_s= surface intensity depicted from edges) from Figure 4.6, was plotted in Figure 4.7. It was concluded from the graph that intensity increases by the equation $(I_b/I_s) = (I_b/I_s)_o + At^{1/3}$; where $(I_b/I_s)_o$ represents the onset value, '*t*' represents growth time and '*A*' is the constant, which clearly signifies the diffusion mechanism for the increment in the bright region of the NWs. Therefore, it was concluded that with the increase in the growth time, more Zn content diffuses towards the surface and leads to increase in the width of the bright boundaries [144]. The intensity profiles were also plotted for the samples prepared at other temperatures *i.e.*70ºC and 120ºC and represented in Figure 4.8. Therefore, it was concluded that all the samples

show similar kind of profile *i.e.* less intensity at the bulk and higher intensity at the boundaries. Thereafter, intensity ratio (I_b/I_s) from Figure 4.8, was plotted in Figure 4.9 (growth time = 8h) and data points were fitted with straight line equation. Therefore, it was cleared that the increase in intensity at the edges shows a direct relationship with the growth temperature.

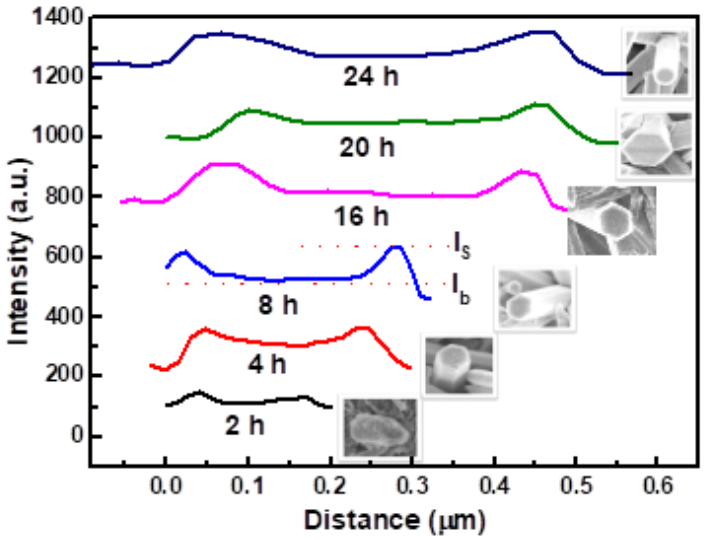

Figure 4.6: Distribution of intensity along the radial direction of NWs for growth times of 2, 8, 16, 20, and 24 h at 90°C.

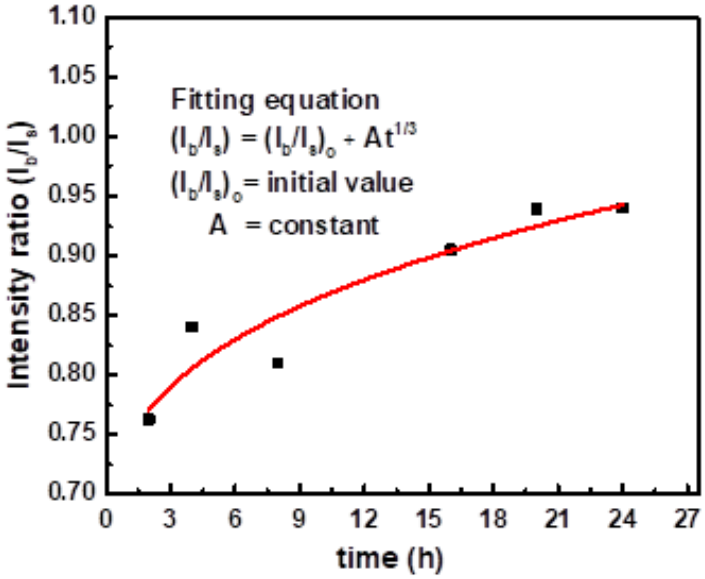

Figure 4.7: Variation of Intensity ratio (I_b/I_s) with respect to the growth time.

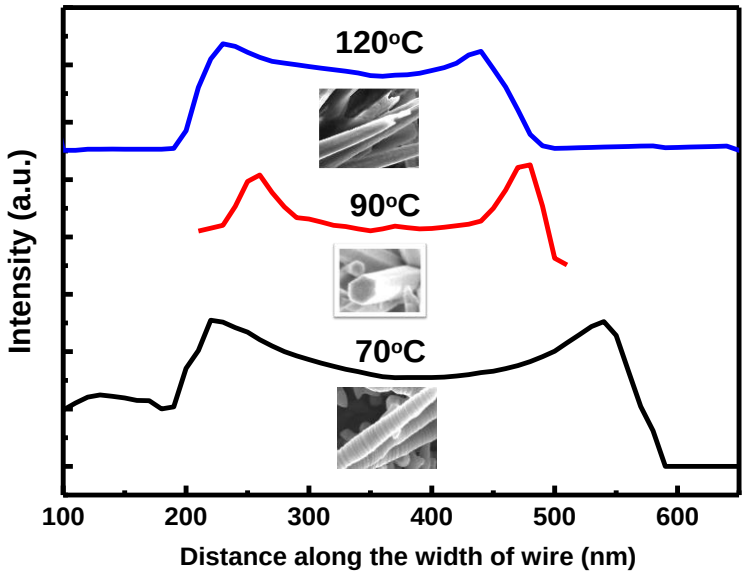

Figure 4.8: Intensity profile of ZnO NW synthesized at 70º C, 90ºC and 120º C growth temperatures at 8 h of growth time.

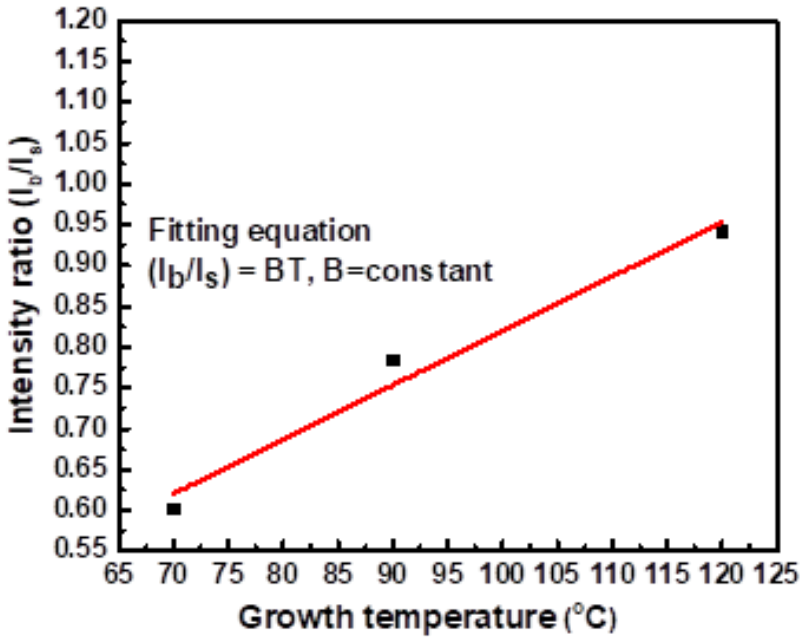

Figure 4.9: Variation of Intensity ratio (I_b/I_s) with respect to the growth temperature.

4.3.3 EDX mapping

Further to confirm the reason for the intense boundaries, the EDX mapping of the prepared samples was recorded. This method is apt for revealing the elemental distribution along the entire length of the nanowire. Figures 4.10 (a,b,c) illustrate the EDX mapping of the samples with non-uniform, hexagonal cross-sectional and cylindrical cross-sectional morphologies of NWs. These figures provide a clear visualization of the presence of a higher concentration of Zn element at the edges of the NWs, as compared to the bulk of the NWs, for all samples. The elemental composition of the samples in weight and atomic percentage were tabulated in the Table 4.2. Additionally, it was also anticipated that the atomic percentage of Zn increases as the morphology of the sample changes from non-uniform NSs to hexagonal and cylindrical cross section. As it was mentioned that a non-uniform structures formed at low temperature *i.e.* 70ºC, whereas hexagonal and cylindrical cross-sectional NWs were obtained at 90ºC. From the previous section (Section - 4.3.2), it was clear that, intensity ratio (I_b/I_s) increases linearly with increase in the growth temperature, that is why as growth temperature increases, Zn content shows an increase. With the increase in growth time, bright boundaries also increase, that is the reason for further increase in the Zn content. These results from EDX spectra also give the confirmation of reason for the bright boundaries *i.e.* they are due to excess Zn content at the surface. Further, Figure 4.11 shows the resemblance of FESEM and EDX mapping image.

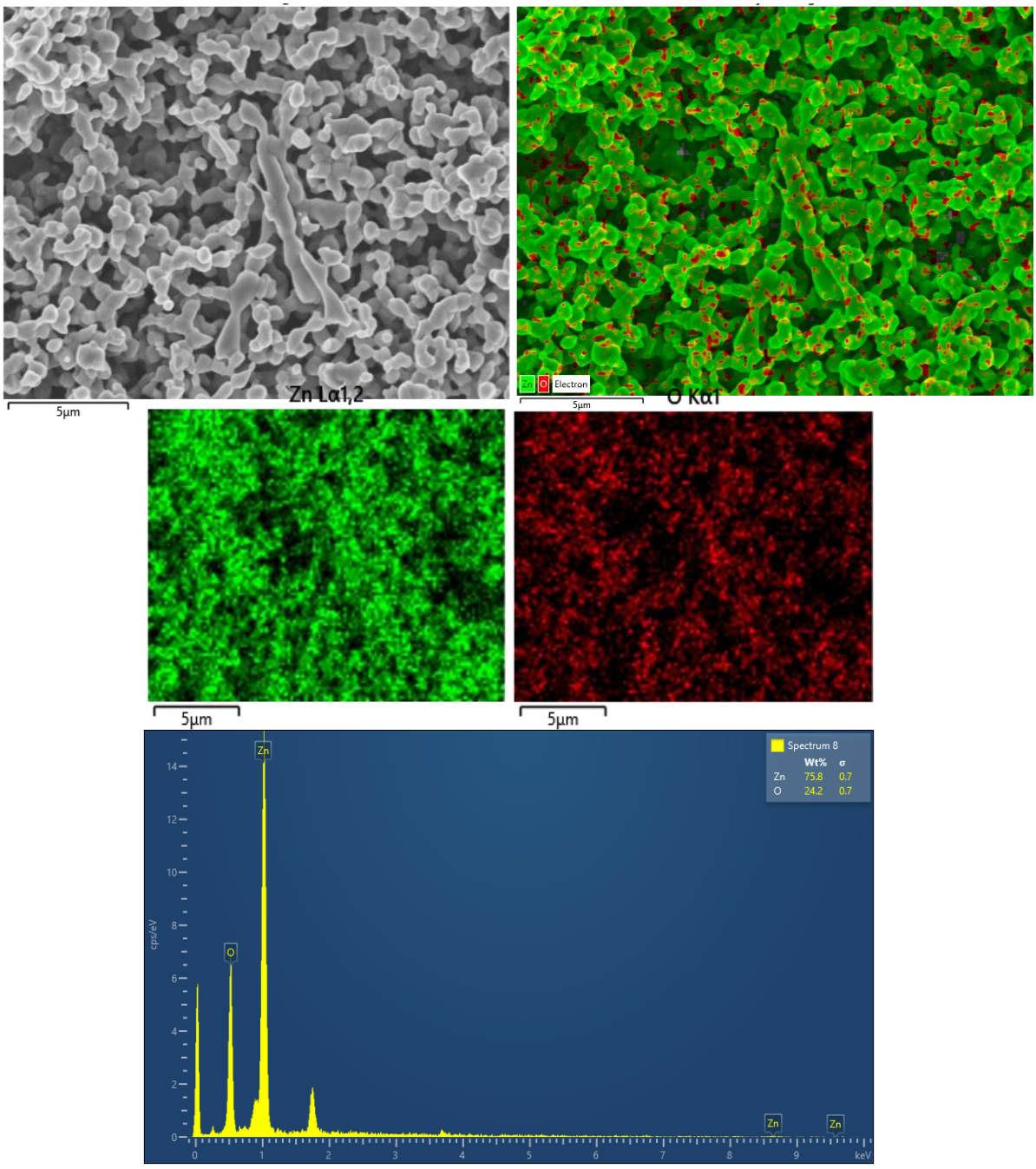

Figure 4.10a: EDX elemental mapping and EDX spectra for the non-uniform ZnO NSs at 70º C.

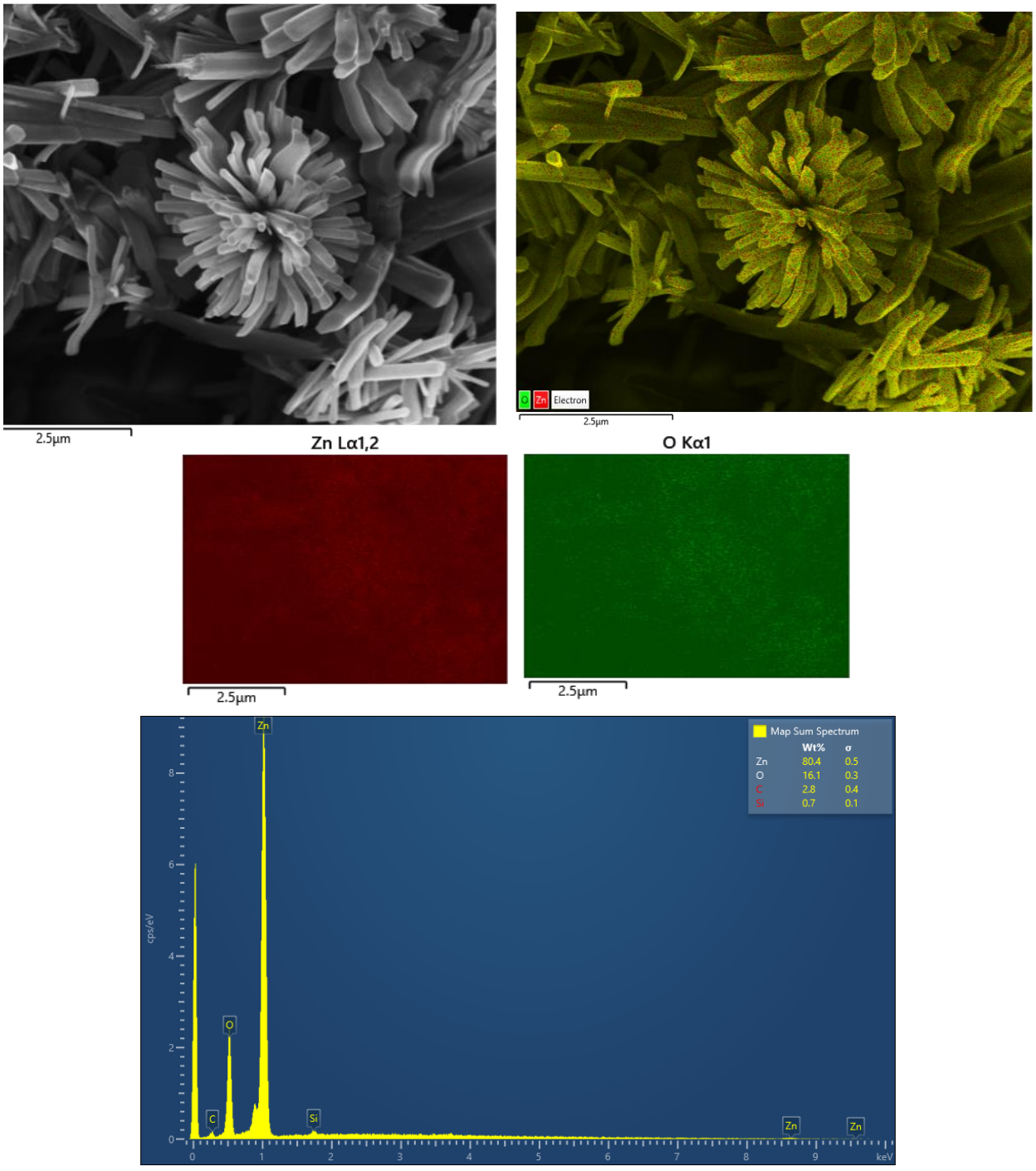

Figure 4.10 b: EDX elemental mapping and EDX spectra for the hexagonal cross section ZnO NWs.

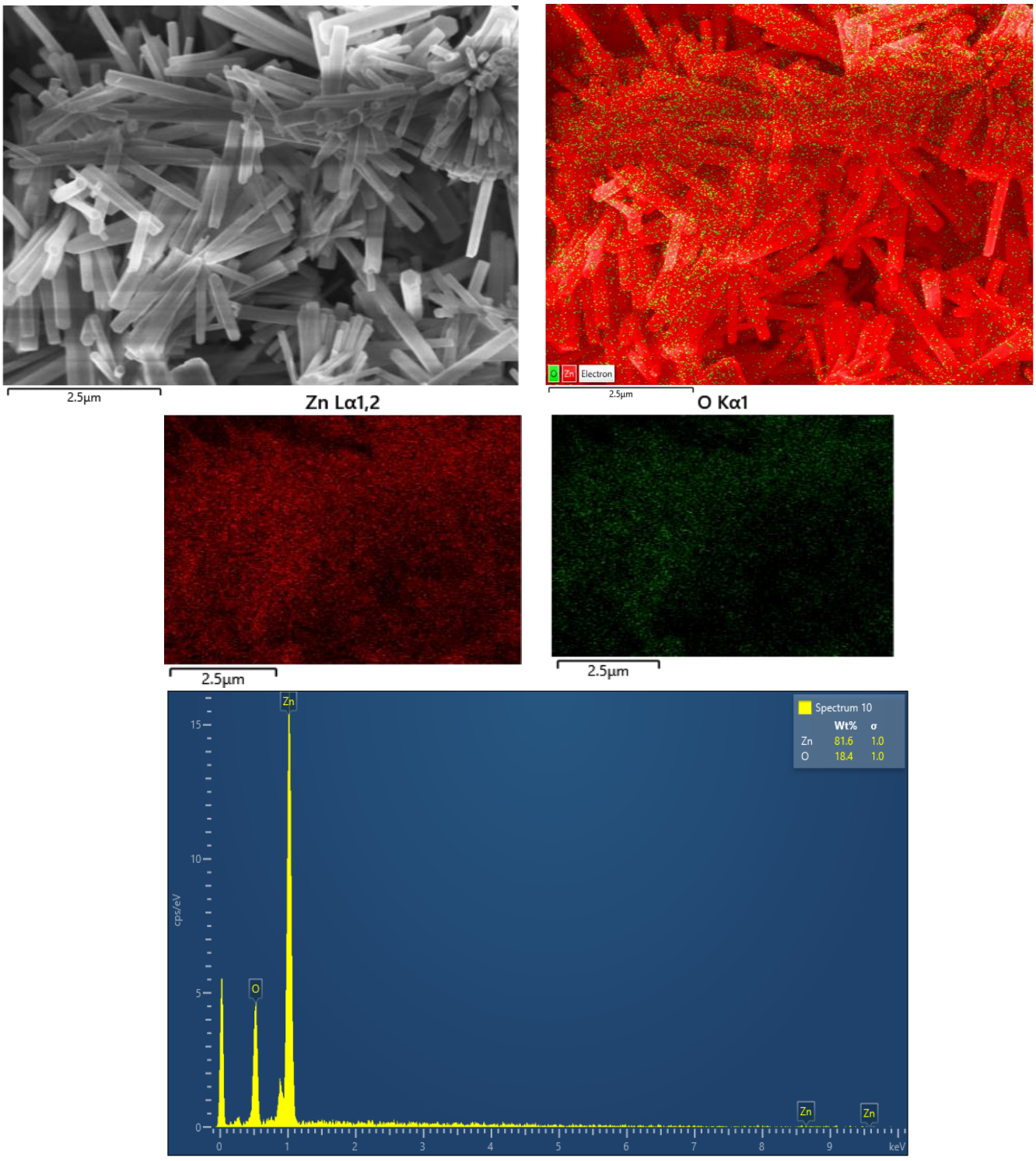

Figure 4.10 c: EDX mapping images and EDX spectra for the cylindrical cross section ZnO NWs.

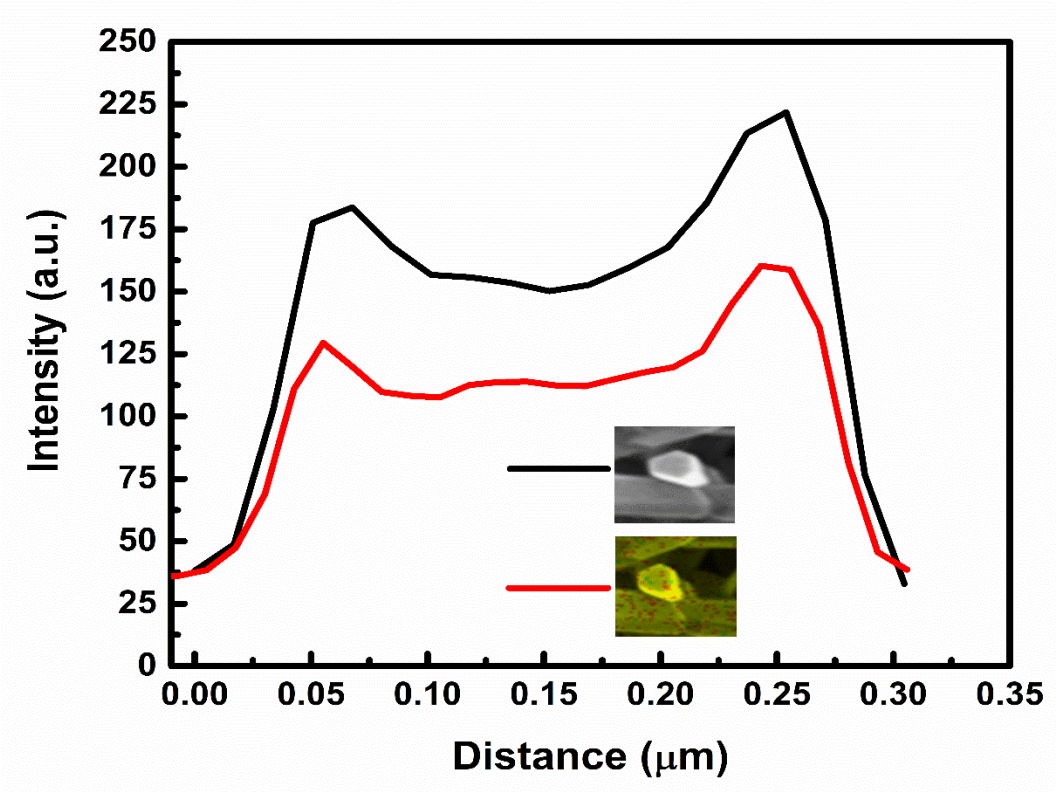

Figure 4.11: A comparison of the intensity plots of EDX and FESEM image of NW.

Table 4.2: Table represents the elemental composition in weight and atomic percentage (from EDX spectra).

Sr. no.	Sample	Element	Weight percentage	Atomic percentage
1	Non uniform ZnO NSs	Zn	78.8	43
2		O	24.2	57
3	Hexagonal cross sectional rods	Zn	80.43	50.15
4		O	19.57	49.85
5	Cylindrical cross sectional rods	Zn	81.63	52.10

6	O	18.37	47.90

4.4 Optical properties

4.4.1 Absorbance spectroscopy (NWs)

Additionally, Figure 4.12 (a) presents the absorbance spectra of the samples grown at 90°C, with varying growth durations ranging from 2 h to 24 h. Band gaps for the entire samples were calculated using Tauc plot. Here, the band gaps were calculated by using the intersection of two straight lines, this is because the absorption below band gap is not approaching zero, instead showing exponential rise. Therefore, it was known that band gap energy is generally tells the minimum energy between VB and CB, which can be observed from the onset value of the absorption coefficient curve. Accordingly, the optical band gaps were measured to be 3.29 eV, 3.26 eV, 3.27 eV, 3.25 eV, 3.26 eV, and 3.28 eV, for the growth periods of 2 h, 4 h, 8 h, 16 h, 20 h and 24 h respectively and (Figure 4.12 b and its inset) tabulated in Table 4.3. The band gap values of the samples closely matched with the energy band gap of the ZnO NWs (~3.27 eV). As a result, it was observed that all the values obtained were relatively similar and the dimensions of the samples were comparable to those of the bulk material. Thereafter, it was also observed from the Tauc plot that there is an exponential curve below band gap, which is showing an increase with the growth time, which might be due to the near band absorption within the band gap [145].

Moreover, absorption below band gap can be expressed by exponential curve shown below:

$$\propto = A \exp\left(-\frac{h\nu}{E_U}\right) \tag{7}$$

where 'A' is constant, '$h\nu$' represent the incident photon energy and 'E_U' is the Urbach energy.

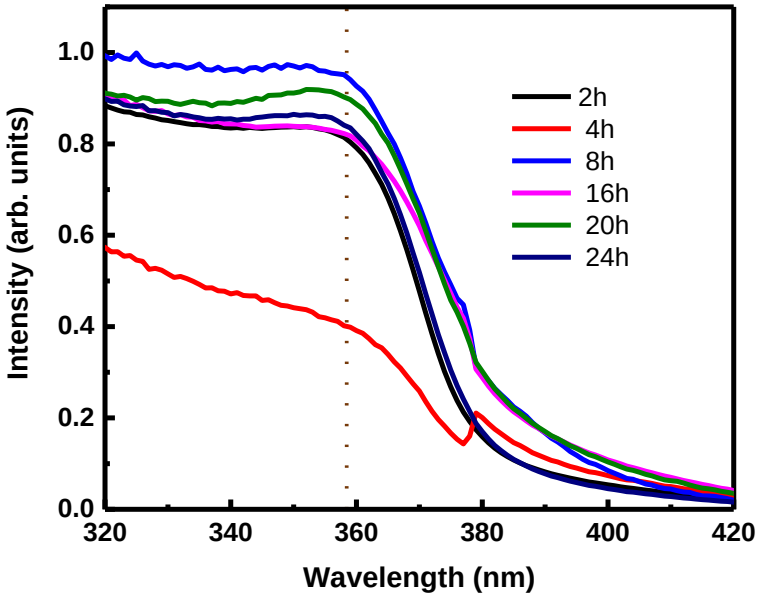

Figure 4.12: (a) The absorbance spectra of the samples prepared at 90°C, with different growth times.

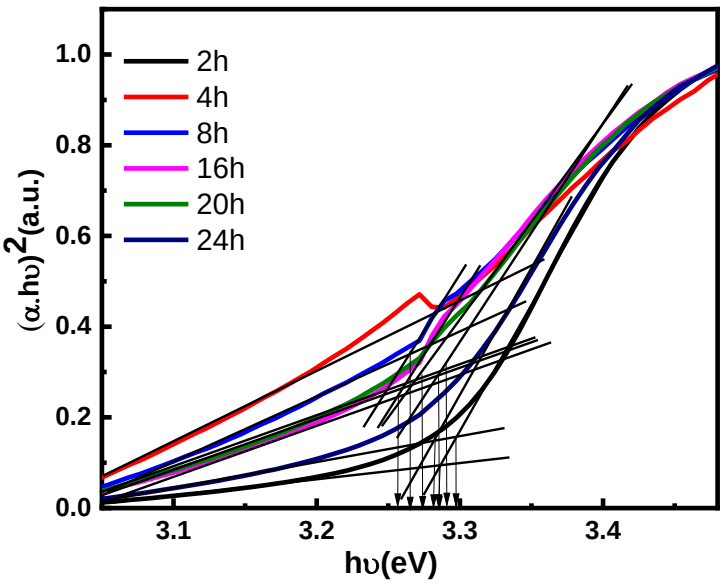

Figure 4.12 (b): Tauc plot for the samples prepared at growth time of 2 h – 24 h.

Table 4.3: Tabular representation of band gap energy values for the samples prepared under constant temperatures 90℃ and at varying growth times.

Sr. no.	Growth time (h)	Band gap (eV)
1	Seeds	3.30
2	2	3.29
3	4	3.26
4	8	3.27
5	16	3.26
6	20	3.26
7	24	3.28

4.4.2 PL-emission studies ($h\upsilon \geq E_g$)

Figure 4.13 represents the PL-emission spectra of samples grown from 2 to 24 h at 90°C. From the spectra three main points are observed, which are given by:

1. Consistent increase in the Zn interstitial defect peak intensity with the growth time.

2. Pinning of the defect states within the band gap.

3. Shift of NBE emission peak towards longer wavelengths with the growth time.

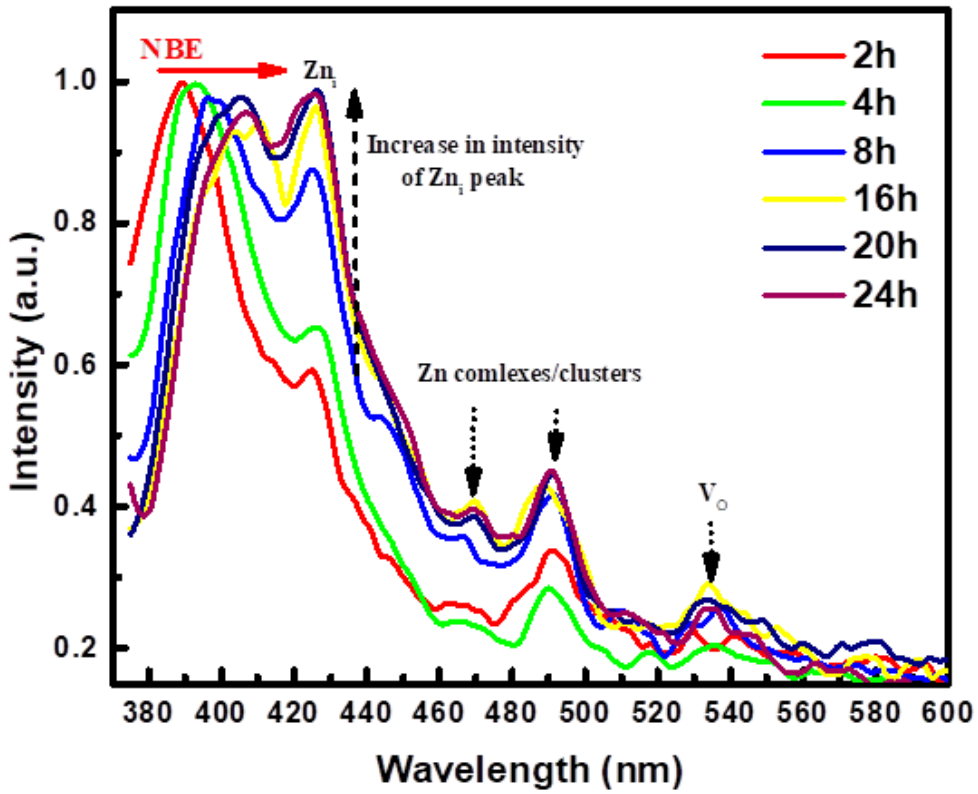

Figure 4.13: PL-emission spectra of the ZnO NWs grown at 2 h, 4 h, 8 h, 16 h, 20 h and 24 h.

It is well known that Zn interstitial has very low migration energy, and can migrate via the kick-out mechanism under room temperature. As the growth time increases, the number of Zn interstitials increases, leading to corresponding increase in Zn interstitial intensity. The results show a linear relationship with growth time (Figure 4.14). The samples prepared at 70℃and 120℃ also display an increase in Zn defect peak intensity, shown in Table 4.4 (intensity ratios). The linear rise in intensity appears to be directly proportional to the size of the depletion region, which was determined to consist of excess Zn or defects related to Zn clusters.

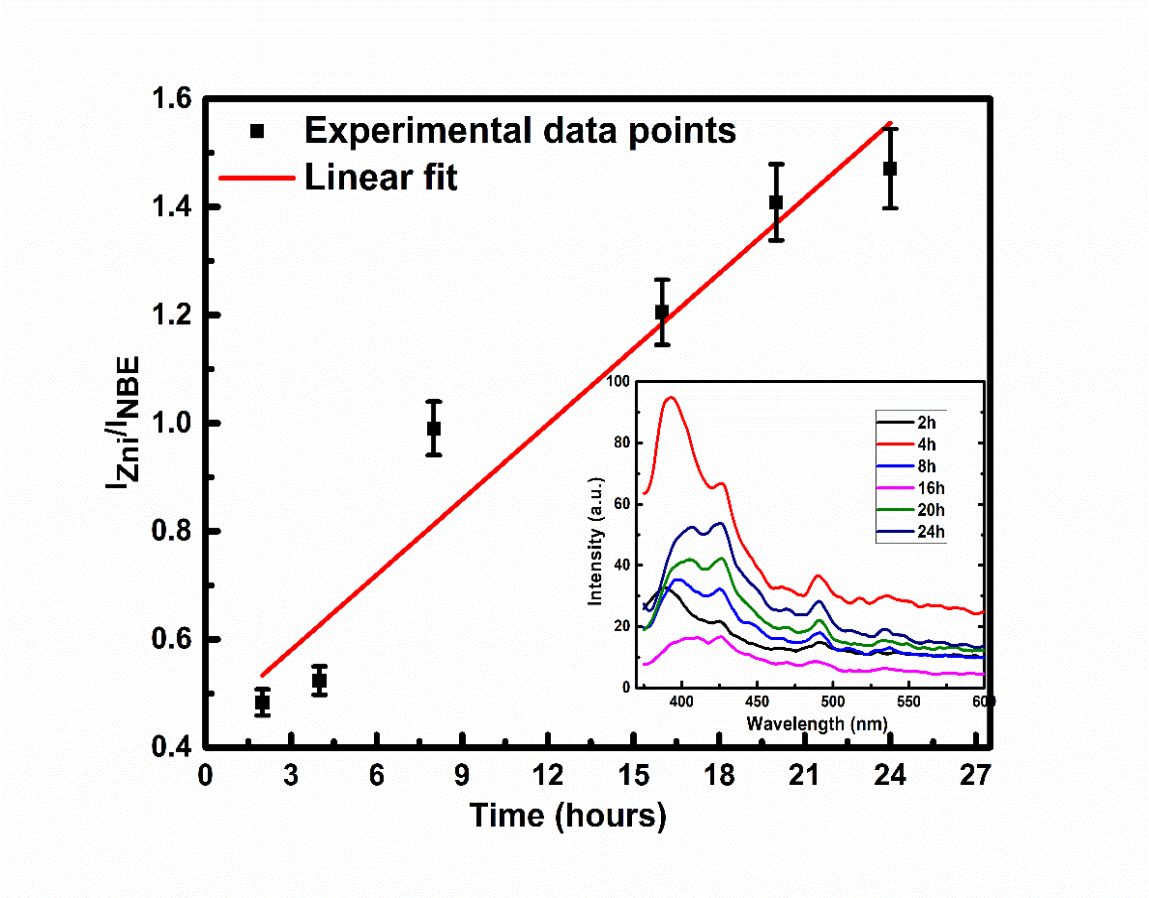

Figure 4.14: Shift in I_{Zni}/I_{NBE} ratio with respect to the growth durations.

Furthermore, the samples prepared at growth temperatures of 70°C, 90°C and 120°C for 8 h and 24 h exhibited a red shift in the NBE emission peak (Figures 4.13, 4.15, and 4.16). The values of shift are represented in Table 4.5. These values of shift (56 meV and 71 meV) are higher than thermal energy (25 meV) at RT. Therefore, these values of shifts are also significant for consideration. Other than NBE emission peaks, defect related peaks were also observed in the PL-emission spectra, position of which remains fixed within the band gap. These defect related peaks corresponds to Zn interstitial (~425 nm), excess Zn and Zn related complexes (~ 448 nm, ~470 nm and ~492 nm) and oxygen vacancy (~536 nm) [21,25]. Fixed positions for the defect state signify the similar local environment of the defects for all the samples. The position of the defect states is defined by the surrounding environment of the defects not by the energy of the electrons in the band.

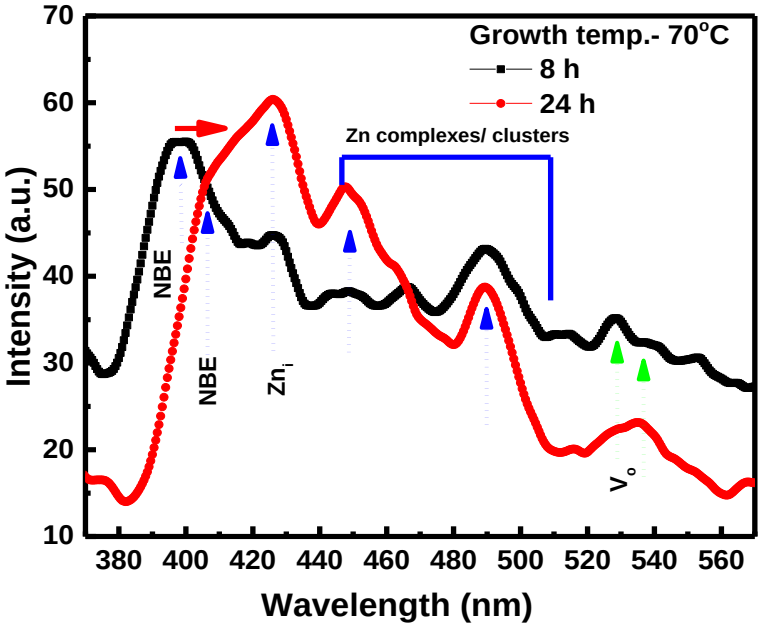

Figure 4.15: Shift in NBE emission peak with respect to growth duration of 8 h and 24 h (70ºC)**.**

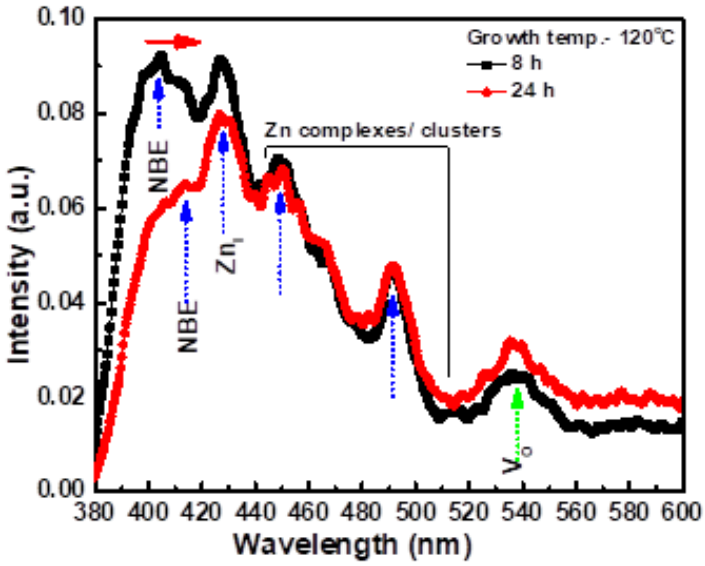

Figure 4.16: Shift of the NBE emission peak as a function of the growth duration of 8h and 24h (120ºC).

Table 4.4: Intensity ratios of Zn_i peak with respect to the NBE emission peak.

Sr. no.	Temperature (ºC)	Growth time (h)	I_{Zni}/I_{NBE}
1	70	8	0.81
2		24	1.18
3	90	8	1.00
4		24	1.06
5	120	8	0.99
6		24	1.20

Table 4.5: Variation in the NBE emission peak shift with changing growth temperature and time.

Sr. no.	Temperature (ºC)	Growth time (h)	PL (NBE) E_{NBE} (eV)	PL energy shift (NBE) ΔE_{NBE} (eV)
1	70	8	3.113	0.056
2		24	3.057	
3	120	8	3.068	0.071
4		24	2.997	

4.4.3 Surface analysis for unexpected shift in NBE emission peak (Band bending concept)

The NBE emission peak maxima were observed to shift towards higher wavelengths with longer growth times as shown in the PL-emission spectra (Figures 4.13, 4.15, 4.16). Table 4.6 shows the values of their NBE emission energies and depletion layer width for different growth times (2 h to 24 h). With reference to the first sample (2 h), the red shift value for the NWs synthesized at 90ºC varies from 55 meV to 149 meV. Energy resolution for PL-emission spectrophotometer is ±4 meV. The values of energy shift in the present case are greater than the energy resolution values. Therefore, this observed red shift is quite significant. A change in the growth temperature and time of the samples, as listed in Table 4.5, resulted in a red shift of the NBE emission peak. Specifically, the shift occurred as the growth temperature was decreased from 90º C to 70º C (or increased to 120º C) and as the growth time was extended from 8 h to 24 h. Previous studies reports the quantum confinement as the main reason for blue shift/red shift with the decrease/increase in the width of the NWs [147]. However, dimensions of nanowires in the present study are quite large, making it difficult to observe the quantum confinement effect and as a result, this approach may not provide an accurate explanation for the shift. Therefore, a different approach to the problem is required.

The surface effect was put out as a remedy to overcome the present situation after a careful evaluation of the obtained results. Studies have reported that n-type semiconductors with metallic cluster boundaries exhibit upward band bending [148].

Because in the n-type semiconductor, there are abundance of electrons and when metal with higher work function comes in contact with it, then electrons will start flowing from the semiconductor to the metal in order to align the Fermi level. When Fermi level of semiconductor and metal gets aligned, then Helmholtz layer formed between them. At the metal/semiconductor interface, a Helmholtz double layer is formed where the metal layer carries a negative charge and the semiconductor surface is positively charged due to electrostatic induction. The low concentration of charge carriers in the semiconductor prevents effective screening of the electric field between the metal and semiconductor interface. This results in the depletion of free carriers near the semiconductor surface compared to the bulk, leading to the formation of a depletion region. The electric field and charge transfer between the semiconductor and metal cause the band to bend

upwards in this region. To describe the potential in the depletion region relative to the bulk, the Poisson equation was employed, which is given by:

$$\nabla^2\varphi = -\frac{\rho}{\varepsilon} \qquad (8)$$

where 'ρ' is the charge density in the depletion region and 'ε' is the permittivity. Thereafter, it was assumed that surface charge density along 1-D and given as:

$$\frac{d^2\varphi_{BB}}{dz^2} = -\frac{\rho}{\varepsilon} \qquad (9)$$

Assuming the depletion region is in the n-type semiconductor, it was also assumed that the positive charges in the depletion region are due to the complete ionization of the bulk donors, which are homogeneously distributed with density '*n'*.

$$\rho = en; 0 < z < W \qquad (10)$$

$$\rho = 0; z > W \qquad (11)$$

where '*W'* is the depletion width. Using equations (9-11), 'φ_{BB}' within the depletion region is evaluated, given as:

$$\varphi_{BB}(z) = -\frac{en}{2\varepsilon_r\varepsilon_o}(z-D)^2; \quad 0 \le z \le D \qquad (12)$$

'φ_{BB}' shows the parabolic relation within the depletion width. Thus the depletion width can be evaluated, if the potential at *z=0* is known, therefore, this can be shown as:

$$W = \left[\frac{2\varepsilon_r\varepsilon_o\varphi_{BB}(0)}{en}\right]^{1/2} \qquad (13)$$

Therefore, the formula for the band bending can be written as [149] [17,27]:

$$\varphi = \frac{enW^2}{2\epsilon_{ZnO}\epsilon_o} \ldots\ldots\ldots\ldots\ldots (14)$$

Here, *'φ_{BB}'* is replaced by the 'φ' and 'ε_r' by 'ε_{ZnO}'. To perform the calculation, the given values were utilized for $\in_{ZnO}$, $\in_o$, ***n*** and ***e*** *i.e.* ~8.66, 8.85 X 10^{-12} $m^{-3}kg^{-1}s^4A^2$, ~10^{23} cm^{-3} and 1.6 X 10^{-19} C utilized respectively [148].

Here, dielectric constant value of ZnO was utilized, because it was mentioned previously that the depletion layer forms at the surface of n-type semiconductor (ZnO). Furthermore, a constant carrier concentration was assumed in order to solely observe the impact of depletion width on the magnitude of band bending. But in actual, it depends on defect concentrations in the sample.

Here, the FESEM pictures (Figure 4.6) of ZnO NWs are used to determine the depletion layer's width. The Energy Dispersive X-ray Spectroscopy (EDS) mapping images confirms the reason of bright boundaries of NWs. It shows that there is excess Zn element distribution at edges in contrast to the interior of the nanowires. Table 4.6 illustrates how the magnitude of band bending changes with variations in the width of the depletion layer and the growth time of the nanowires. Observations revealed that as the width of bright boundary increases, the band bending values also shows an increase, which is reflected in the shift towards longer wavelengths of PL-NBE peak. It was demonstrated from Table 4.6 is that, the value of band bending energy for growth time of 2 h is comparable to the thermal energy of RT, therefore this value in insignificant to consider. However, the subsequent values of band bending energies are significantly larger than thermal energy, and therefore, they are considered effective shifts that should be taken into account.

Table 4.6: Table represents the band bending values, depletion layer width and PL-emission shift with the impact of growth time (temperature - 90º C).

Sample	**Growth time (h)**	**PL (NBE) E_{NBE} (eV)**	**Depletion layer width (nm)**	**Band Bending extent E_b (eV)**	**PL shift (NBE) ΔE_{NBE} (eV)**
1	2	3.199	16	0.026	-
2	4	3.144	19	0.037	0.055

3	8	3.120	21	0.046	0.079
4	16	3.077	27	0.076	0.122
5	20	3.050	28	0.082	0.149
6	24	3.050	30	0.094	0.149

Thereafter, in order to analyze the path length of the free electrons in the conduction band, the diffusion length of the electron in conduction band was calculated. Using the diffusion coefficient of the electron "***D = 0.05-0.5 cm²/s*** for single ZnO NW in CB" [150], diffusion length was calculated using relation given by:

$$\boldsymbol{l = \sqrt{2Dt}} \tag{2}$$

where ***l*** = diffusion length, ***t*** = electrons life time in Conduction band (300 picoseconds)

$$\boldsymbol{l = \sqrt{2 * 0.05 * 300 * 10^{-12}}} \quad \text{or} \quad \boldsymbol{l = \sqrt{2 * 0.5 * 300 * 10^{-12}}} \tag{15}$$

$$\boldsymbol{l = 17.32 \; or \; 173.2 \; nm} \tag{16}$$

Using the above relation, the diffusion length ('***l'***) of electron in CB is calculated to be ***17.32 nm***, when the diffusion coefficient (D) equals ***0.05 cm²/s.*** As a result, the movement of charge carriers (e^-) in CB is towards the center of the ZnO NW and vice-versa for the holes (Figure 4.17 a). Therefore, the recombination of charge carriers can be given by:

$$\boldsymbol{E_g^1 = E_{NBE} = E_g - E_b} \qquad \boldsymbol{as \; E_g^1 \; (E_{NBE}) < E_g} \tag{17}$$

where E_g = band gap, E_b = band bending and E_g^1 = Effective NBE emission energy

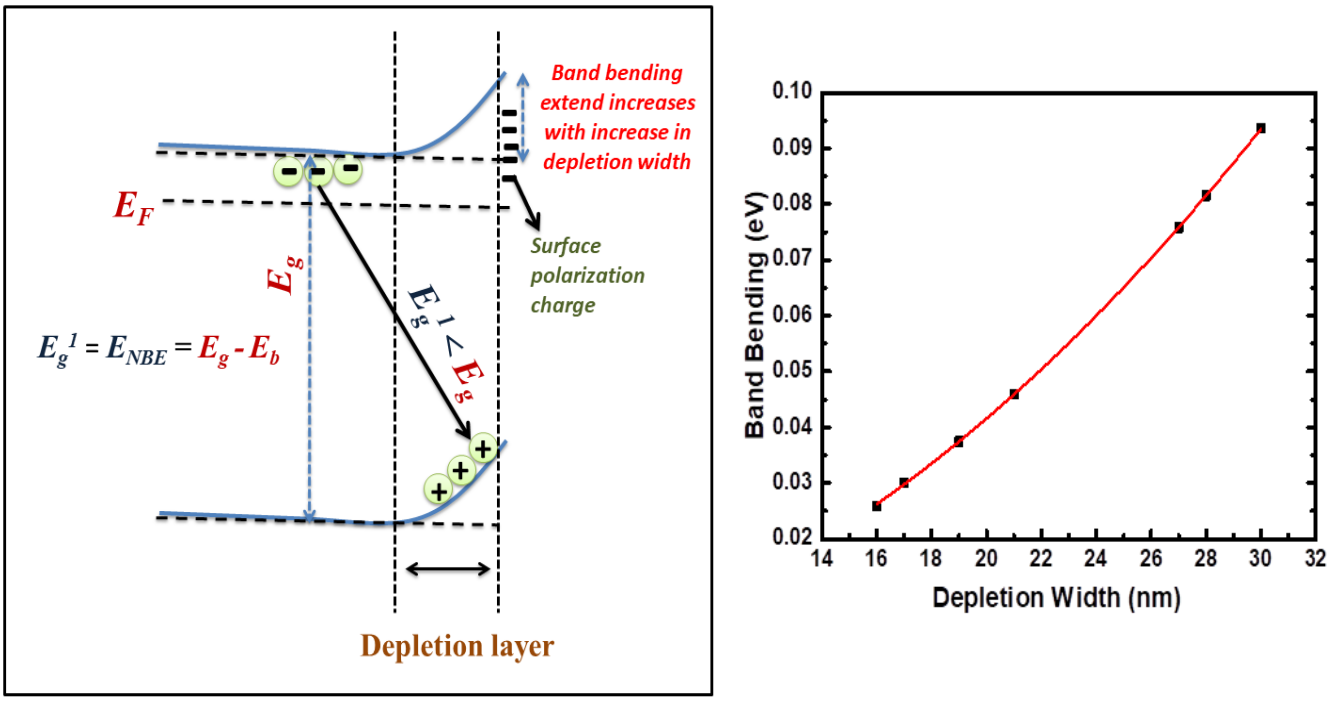

Figure 4.17: (a) Diagrammatic illustrations of band bending phenomenon occurring at the surface of a nanowire and the accompanying e^- - h^+ recombination and (b) Variation of bend bending with the depletion layer width.

Figure 4.17 (a) illustrates that as the radial growth of NWs enhances, the value of band bending 'E_b' shows an increase, resulting in a drop in the near band edge emission energies 'E_{NBE}'.

The shift in the NBE emission peak can also be understood by the concept of quantum confinement. Quantum confinement can be assumed to be occurred at the surface of the NWs *i.e.* in the bright boundary region of the NWs. If potential at the surface of the NWs was assumed to be:

$$V(x) = \begin{cases} 0 & a < x < b \\ V_0 & x \leq b, x \geq a \end{cases} \ldots\ldots\ldots\ldots\ldots (18)$$

Here height of the potential well 'V_0', was assumed to be equivalent to the work function of the NWs. Then a large amount of energy is required for an electron to overcome this barrier height and therefore, electrons were assumed to be confined within the potential well. Therefore, the surface

of the nanowires can be called as the infinite potential well for the charge carrier electron, which was deduced to be confined within it as shown in Figure 4.18(a).

Figure 4.18(b) illustrates a plot of the energy (PL - NBE emission) versus the width of the depletion layer, following the confinement relation $E\ \alpha\ \frac{1}{d1^2} + \frac{1}{d1}$. The depletion layer width '*d1*' of the nanowire is shown to confine particles *i.e.* electrons in it, thereby explaining the observed energy shift in PL-NBE energy state.

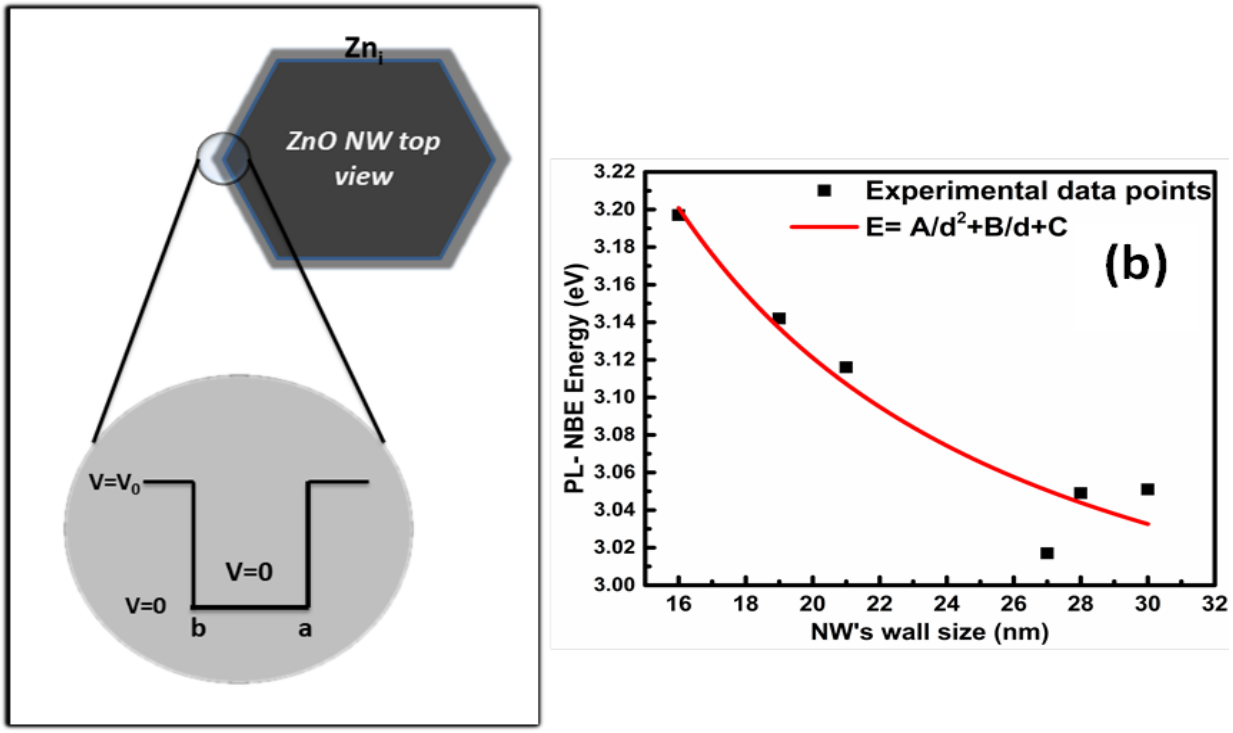

Figure 4.18: (a) and (b) depict the concept of quantum confinement at the surface of NW through a schematic representation and a graph, respectively. The graph shows the experimental shift in PL-NBE emission as a function of the depletion layer width of the NWs, with the curve fitting following the confinement relation.

Additionally, due to the presence of surface polarization charges at the surface at room temperature can also enhances the absorption of environment oxygen [151]. This can be achieved through the capture of free electrons by environmental oxygen as given by [149]:

$$O_2 + e^- \rightarrow O_2^- \qquad (6)$$

This can also participate in enhancing the depletion width at the surface. The similar phenomenon was assumed to happen also for the NWs aged at 70℃and 120℃.

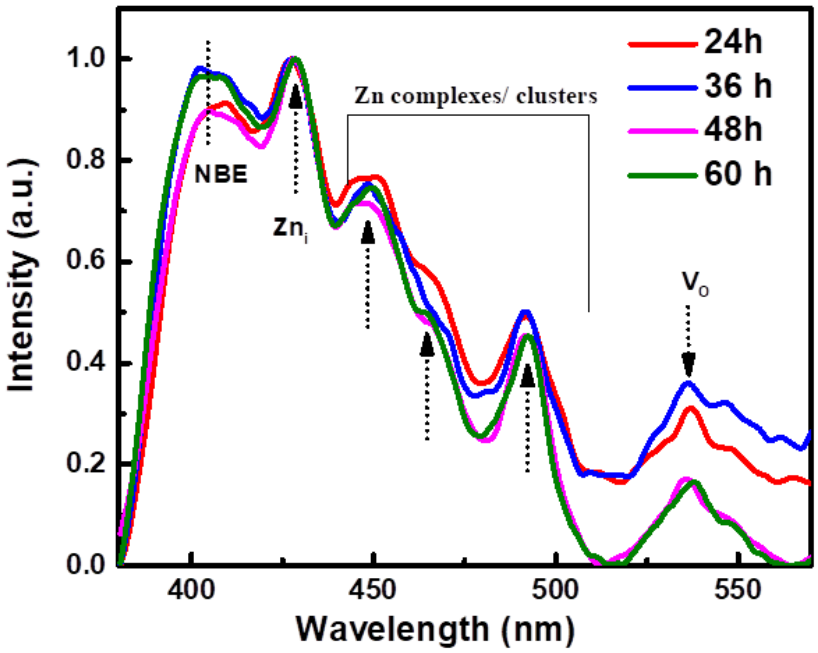

Figure 4.19: PL-emission spectra at higher growth times.

Thereafter, PL-emission spectra were also recorded at higher growth times and shown in Figure 4.19. It was observed from the graph that, with further rise in the growth time, the variation in the NBE emission peak gets saturated and no further shift was observed. Therefore, band bending gets saturated after 24 h.

4.4.4 Sub - band gap excitation ($h\upsilon < E_g$)

ZnO NWs can be excited below the band gap energy value. Sub band gap excitation is possible by various imperfections and defect states present within band gap as per reported studies [152]. If the sample were excited with wavelength 400 nm ***($h\upsilon < E_g$)***, then the PL - spectra shows emission energies in the visible region corresponds to values as ~480.01 nm, ~540.04 nm, ~560.08 nm and ~603.02 nm (Figure 4.19 a). Furthermore, the use of excitation wavelength of a 450 nm resulted in

the appearance of an emission peak at approximately ~603.02 nm, which suggests the existence of Zn vacancies in the samples (Figure 4.19b).

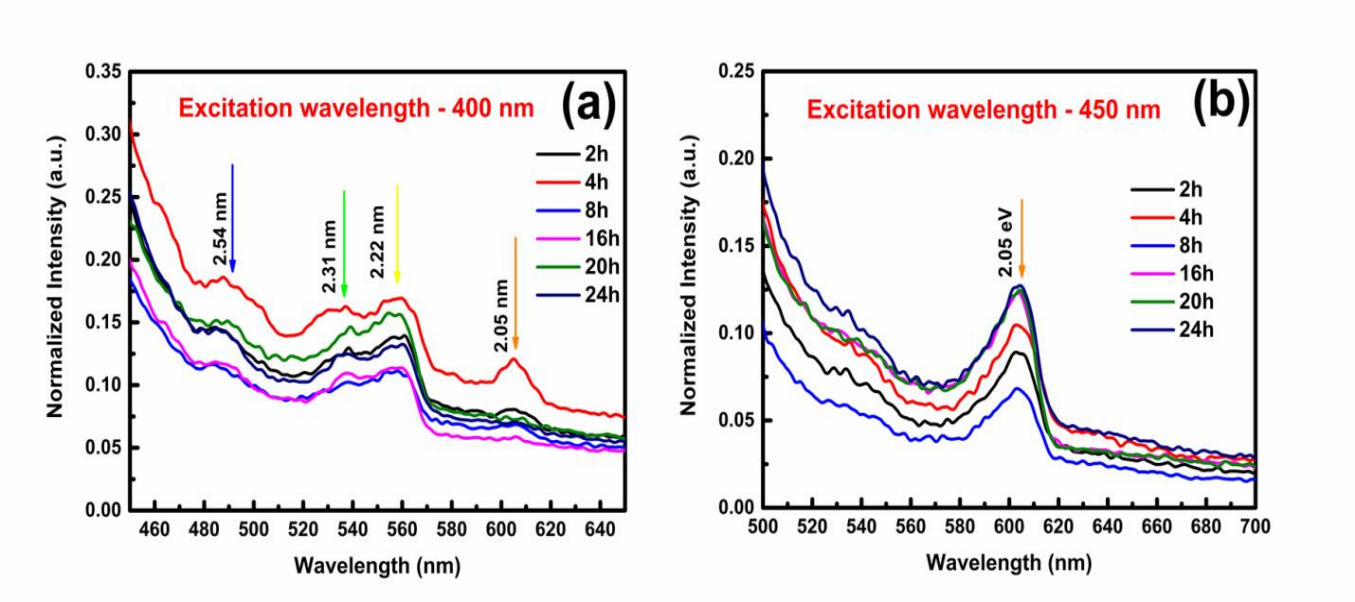

Figure 4.20: (a) Excitation of ZnO sample with sub-band gap excitation energy of ~ 400 nm and (b) ~450 nm.

4.4.5 Raman spectroscopy

Raman spectroscopy gives us the information about the vibrational modes in the ZnO NWs prepared for different growth times. As we know that ZnO has a hexagonal wurtzite structure belongs to C_{6v}^4 space group and according to group theory it should have eight sets of phonon normal modes at the zone center (Γ). These normal phonon modes are given by:

$$\Gamma = 2A_1 + 2B_1 + 2E_1 + 2E_2 \qquad (7)$$

Modes 'A_1'and 'E_1' are the acoustic and rests of the modes are optical [153], [154]. In Raman spectra, only optical modes were observed.

Both 'A_1' and 'E_1' modes are Raman or IR active and which can be further splits into transverse optical (TO) and longitudinal optical (LO) phonons. In contrast, the 'E_2' modes are Raman active and consists two frequency modes 'E_2^{high}' and 'E_2^{low}' whereas 'B_1' mode is inactive or called as silent mode. 'A_1' mode in the spectra appears only when the incident light falls parallel to [0001]

plane of the highly oriented ZnO thin film. In the present case, the 'E_2^{high}', 'E_2^{low}' and '$E_2^{high} - E_2^{low}$' modes were observed. The 'E_2^{high}' mode arises from the vibrations of oxygen sub-lattices whereas 'E_2^{low}' energy results from the vibrations of the massive Zn sub-lattices [155]. Furthermore, additional modes such as '*2TA*' ('*2E₂ (low)*'), '*A₁ (TO)*', '*A₁ (LO)*' were identified and attributed to a multi-phonon process. The observed modes confirm the hexagonal wurtzite structure of high-quality ZnO crystal. Table 4.7 represents the peak positions of the observed vibrational modes at different growth times. Figure 4.20 (a) represents the Raman spectra for the sample grown at 2 h in the wavenumber range varied from 0 cm^{-1} to 1500 cm^{-1}. Figure 4.21 (b) depicts the Raman spectra for the samples at subsequent growth time varying from 2 h to 24 h.

In present case, two observations were made from the spectra (Figure 4.21b):

(i) Broadening of the various peaks in the spectra, and

(ii) The shift in the frequency of the peaks over time.

Various reasons have been reported for the broadening of Raman modes, including quantum confinement [156], surface bond contraction [156], bond length contraction [157], temperature variation [32], and defects or structural disorder [33]. However, in the current study, the broadening of the modes was found to be caused by the presence of defects and impurities in the sample, specifically due to the presence of Zn interstitials or clusters [160]. These defects violate the phonon selection rule *i.e. q=0*, resulting in the scattering of phonons with *q≠0*. This leads to the involvement of both acoustic and optic phonons in phonon dispersion, resulting in the broadening of the peaks. The tensile strain or stress might be the reason behind the shift in the frequency value [158] .

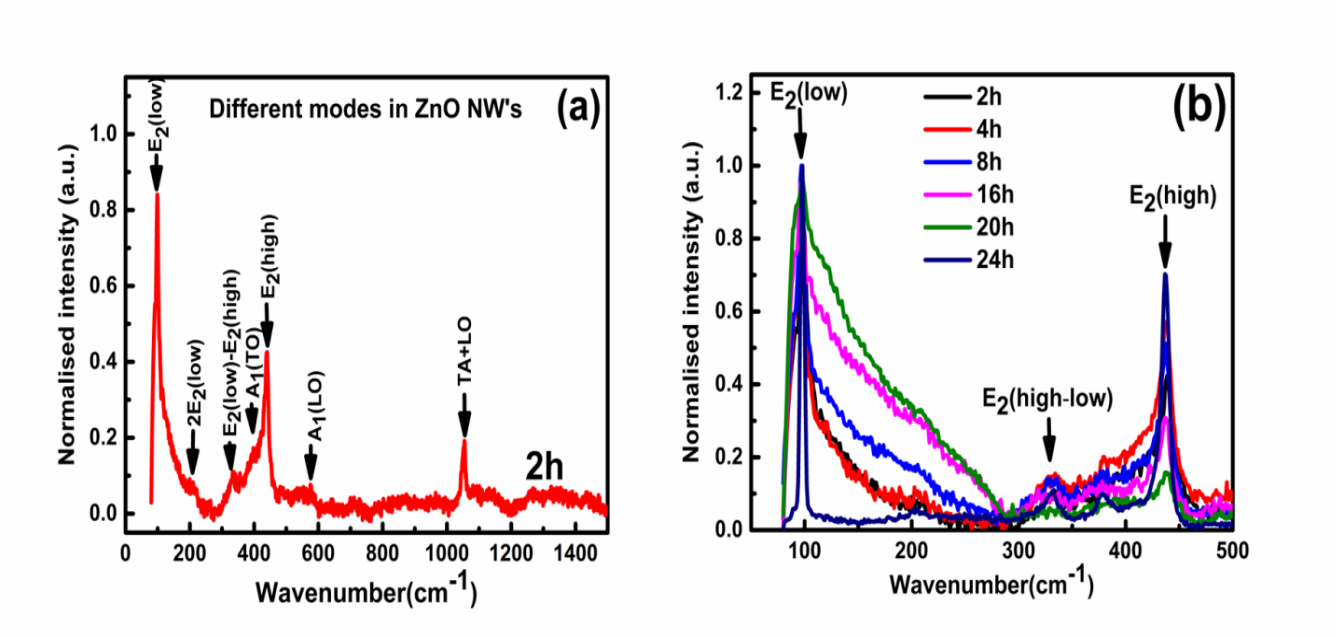

Figure 4.21:(a) The Raman spectra of ZnO nanowires (NWs) aged for 2 hours are analyzed in the frequency range of 80 cm^{-1} – 1400 cm^{-1} and (b) Raman spectra for samples grown at 2, 4, 8, 16, 20, and 24 h in the frequency range of 80 cm^{-1} – 500 cm^{-1}.

Table 4.7: Raman active modes in ZnO nanowires.

	ZnO Modes							
		Frequency (cm^{-1})						
Sr. no.	**Frequency Modes**	**Growth Time**						**Reference**
		2 h	**4 h**	**8 h**	**16 h**	**20 h**	**24 h**	[158]
1	E_2(low)	98	98	98	97	98	99	99
2	2TA, 2 E_2(low)	199	212	203	203	209	205	203

3	E_2(high)-E_2(low)	333	335	330	332	332	333	333
4	A_1(TO)	-	383	373	380	391	378	378
5	E_2(high)	438	436	436	439	438	438	438
6	A_1(LO)	576	573	569	570	564	579	574
7	TA+LO	1056	1053	1052	1054	1053	1072	1072

4.4 CONCLUSION

In this chapter, the morphological and optical properties of the NWs were discussed, which were prepared under different growth time and at fixed temperature conditions. The findings of this research shed light on the unusual shifts observed in the PL-NBE emission peaks with the increasing growth time. The summary of the chapter's conclusion is outlined below:

- The effect of growth times thus concluded to impact the cross sections of the synthesized NWs such as hexagonal cross section transformed to cylindrical cross section with the growth time.
- The intensity of Zn_i defect peak observed to increase with the increase in growth time for all the samples. This indicates that as the growth time increases, more growth species attach to the NWs, leading to a higher intensity of Zn_i defects.
- The difference in the intensity profile of the center and edges of the NWs indicates that their is possible existence of excess Zn_i or Zn related clusters, with a comparatively higher concentration on the surface than in the interior of the NWs.
- The abnormal variation in the PL-NBE emission peak with respect to the growth time was observed for all the NWs prepared at different temperatures. The cause of this shift is due to the surface band bending caused by the presence of excessive Zn at the surface.
- The broadening of the E_2(low) (~99 cm^{-1}) Raman spectral peak, was attributed to the presence of Zn cluster defects in the NWs sample.

CHAPTER 5

CONCLUSION AND FUTURE SCOPE

5.1 CONCLUSION

Zinc Oxide (ZnO) nanowires has gained attention due to their unique optical properties and potential applications in various fields. These NWs are highly valued for their large surface-to-volume ratio, which leads to improved charge collection and transport properties. Additionally, their non-toxicity, easy synthesis and bio-compatibility make them an attractive material for various applications [161]. Optically, ZnO NWs are highly desirable due to their wide optical band gap (approximately 3.27 eV) and large exciton binding energy (approximately 60 meV) at room temperature. These properties, along with their high surface-to-volume ratio, make ZnO NWs ideal for use in optoelectronics such as photo detectors, sensors, LEDs, and solar cells. Additionally, their strong light emission and high transparency make them suitable for use in various displays and lighting applications. The conclusion of each chapter of the thesis is summarized below:

Chapter 1: "Introduction and review of literature". This chapter provides a brief overview of ZnO, including the reasons for its popularity in nanotechnology. In addition, the chapter discusses nucleation and growth models and various existing synthesis methods, such as physical methods and chemical methods for the growth of ZnO nanomaterials.

Chapter 2: "Studies on temporal growth and aging of ZnO nanoparticles**".** This chapter introduces the synthesis of ZnO Nanoparticles (NPs) and investigated the temporal evolution and aging of ZnO nanoparticles (NPs) in colloidal solution through the use of both experimental and theoretical methods. UV-vis spectroscopy and TEM results demonstrate that nucleation and growth occur within 2 minutes in the growth solution. Atomically balanced and unbalanced precursors were studied in details. Therefore, it was found that atomically balanced reactions (S1) result in growth and aging of NPs, while atomically unbalanced reactions (S2) result in decoupling of growth due to the presence of an excess of Zn environment around nuclei. Thereafter, the growth of NPs was understood and modeled using a theoretical model *i.e.* Phase field model (PFM).

Chapter 3: "Effect of temperature on the morphological and optical properties of ZnO NWs". The conclusion of this chapter highlights the significance of temperature variations on the final morphology of ZnO NSs. Absorption studies have shown that the growth temperature has a significant impact on the optical band gap values of ZnO nanowires (NWs). The NWs synthesized

at 90℃ showed a noticeable difference from those synthesized at 70℃ in terms of optical band gap values, possibly due to non-uniform growth of the NWs. The FEEM results showed that broken and hollow tips of NWs can be obtained at a temperature of 120℃ and growth time of 8 hours. The intensity of Zn_i defects increased with the growth time for all samples synthesized at 70℃, 90℃and 120℃, indicating that more growth species attached to the NW's surface, resulting in an increase in Zn_i defect-related intensity. Additionally, the XRD data analysis showed that temperature has a significant effect on the crystallite size and strain of the NSs.

Chapter 4: "Effect of growth time on the morphological and optical properties of ZnO NWs". This chapter describes the impact of growth time on the optical properties of the ZnO NSs obtained at different growth durations. The growth time was found to impact the cross sections of the synthesized NWs, with a hexagonal cross section transforming into a cylindrical cross section with only changing the growth time. It was also concluded that growth time beyond 24 hours leads to a consistent increase in the length of NWs. The intensity profile difference within the center and edges of the NWs suggested the presence of excess Zn interstitials or metal clusters at the surface of the NWs compared to the bulk. The core importance of this chapter is the red shift in the near band edge emission peak of the PL-emission spectra with increase in the growth time. The band bending concept at the surface of the nanowires were introduced and explained. The broadening in the Raman spectral peak at 99 cm^{-1} with increased growth time was found to be influenced by the presence of Zn cluster defects in the NWs sample.

5.2 FUTURE SCOPE

- Excess zinc at the surface of zinc oxide (ZnO) nanowires (NWs) can increase the sensing sensitivity of ZnO NW-based sensors by changing the surface properties of the nanowires, such as surface charge and defects. The increased sensitivity can result in improved sensing performance for various sensing applications, such as gas sensing, humidity sensing and chemical sensing.
- One of the key areas of future research is to optimize the amount of excess zinc at the surface of ZnO NWs to achieve the optimal sensing performance for different sensing applications. In order to achieve this, it will be important to develop a deeper understanding of the relationship between the amount of excess zinc and the sensing properties of ZnO NWs.
- Additionally, the excess zinc can also enhance the catalytic activity of the ZnO NWs, making them useful for catalytic applications.

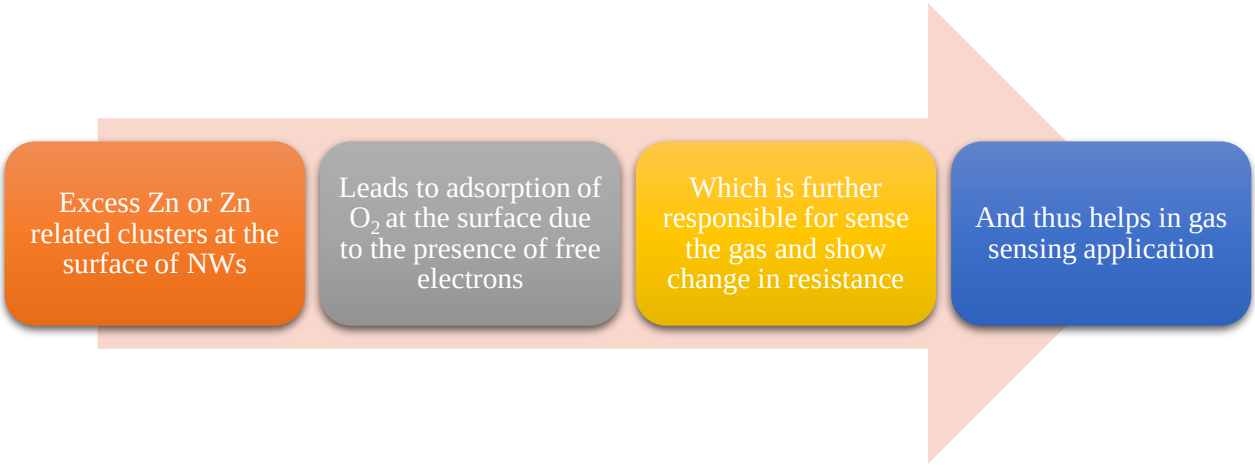

Figure 5.1: Flow chart for the gas sensing applications.

LIST OF PUBLICATIONS

&

CONFERENCE PAPERS

LIST OF PUBLICATIONS & CONFERENCE PAPERS

LIST OF PUBLICATIONS

1. Paper published in J. of cluster science - "**P. Sharma**, S.K. Tiwari, P.B. Barman, Temporal Growth and Aging of ZnO Nanoparticles in Colloidal Solution: Phase Field Model, J. of Cluster Science (2022). https://doi.org/10.1007/s10876-022-02309-3**" (SCOPUS, SCI, and SCIE / IF 3.447)**.

2. Paper published in the J. of luminescence - "**P. Sharma**, S.K. Tiwari, P.B. Barman, Abnormal red shift in photoluminescence emission of ZnO nanowires, Journal of Luminescence 251 (2022) 119231. https://doi.org/10.1016/j.jlumin.2022.119231**." (SCOPUS, ISI SCI / IF 4.171).**

CONFERENCES

1. Paper presented in online mode at "DAE-SSPS 2021: 65th DAE Solid State Physics Symposium 2021" organized by BARC, Mumbai, India entitled "Morphological transition of the ZnO hexagonal nanowires to cylindrical nanowires".

2. Conference "Emergent Converging Technologies and Biomedical Systems (ETBS 2022)" attended and paper presented in virtual mode at Jaypee university of IT entitled "Absorbance and emission studies of ZnO nanostructures".

3. Conference "CENTRE OF EXCELLENCE IN SUSTAINABLE TECHNOLOGIES FOR RURAL DEVELOPMENT [CESTRD]" attended in virtual mode at Jaypee university of Information Technology" organized by Department of Biotechnology and Bioinformatics from 18-19 September, 2020.

WORKSHOPS

1. Attended one-week hands-on workshop on “Computational Methods for Physics and Materials Science (CMPMS-2022)” organized by Department of Physics and Materials Science, Jaypee University of Information Technology during December 29, 2022 to January 3, 2023

2. Attended online workshop on “INUP - i2i Familiarization Workshop on Nanofabrication Technologies”, held at IIT Bombay from 19-21, January, 2022.

3. Attended online workshop on “Recent Advances and Applications of Conducting Polymer Nanostructures and Nanocomposites” (RA2CPNC) at IIT Mandi during 23rd-24th June 2021.

4. Attended online Course on” Refresher Course in Physics (Special Focus on Material Science and Biophysics) Under TEQIP-III” at IIT Dhanbad organized by Department of Physics from 8-20 February, 2021.

5. Attended online workshop on “Rietveld Refinement Method” organized by UGC-DAE Consortium for Scientific Research Mumbai Centre in association with Indore Centre from 20-22, September 2020.

REFERENCES

REFERENCES

[1] V. Balzani, “Nanoscience and nanotechnology: A personal view of a chemist,” Smal, vol. 1, no. 3, pp. 278–283, 2005, doi: 10.1002/smll.200400010.

[2] S. Al Marri, Nanoscience and Technology, vol. 1, no. 1. 2013.

[3] T. Hanada, “Basic Properties of ZnO, GaN, and Related Materials,” pp. 1–19, 2009, doi: 10.1007/978-3-540-88847-5_1.

[4] A. B. Djuriić, A. M. C. Ng, and X. Y. Chen, “ZnO nanostructures for optoelectronics: Material properties and device applications,” Prog. Quantum Electron., vol. 34, no. 4, pp. 191–259, 2010, doi: 10.1016/j.pquantelec.2010.04.001.

[5] J. Y. Lao, J. G. Wen, and Z. F. Ren, “Hierarchical ZnO Nanostructures,” Nano Lett., vol. 2, no. 11, pp. 1287–1291, 2002, doi: 10.1021/nl025753t.

[6] A. Sandhu, “The future of ultraviolet LEDs,” Nat. Photonics, vol. 1, no. 1, p. 38, 2007, doi: 10.1038/nphoton.2006.36.

[7] D. Il Suh, S. Y. Lee, J. H. Hyung, T. H. Kim, and S. K. Lee, “Multiple ZnO nanowires field-effect transistors,” J. Phys. Chem. C, vol. 112, no. 4, pp. 1276–1281, 2008, doi: 10.1021/jp709673s.

[8] M. H. Huang et al., “Room-temperature ultraviolet nanowire nanolasers,” Science (80-.)., vol. 292, no. 5523, pp. 1897–1899, 2001, doi: 10.1126/science.1060367.

[9] X. Wang, C. J. Summers, and Z. L. Wang, “Growth of Aligned ZnO Nanorods for Nano-optoelectronics and Nanosensor Arrays,” Nano, vol. 4, no. 3, pp. 2–5, 2004, [Online]. Available: http://pubs.acs.org/doi/abs/10.1021/nl035102c

[10] V. A. Coleman and C. Jagadish, “Basic properties and applications of ZnO,” Zinc Oxide Bulk, Thin Film. Nanostructures Process. Prop. Appl., pp. 1–20, 2006, doi: 10.1016/B978-008044722-3/50001-4.

[11] C. F. Klingshirn, “ZnO: Material, physics and applications,” ChemPhysChem, vol. 8, no. 6,

pp. 782–803, 2007, doi: 10.1002/cphc.200700002.

[12] S. Ashraf et al., “MOCVD of vertically aligned ZnO nanowires using bidentate ether adducts of dimethylzinc,” Chem. Vap. Depos., vol. 17, no. 1–3, pp. 45–53, 2011, doi: 10.1002/cvde.201006881.

[13] A. T. Le, M. Ahmadipour, and S. Y. Pung, “A review on ZnO-based piezoelectric nanogenerators: Synthesis, characterization techniques, performance enhancement and applications,” J. Alloys Compd., vol. 844, p. 156172, 2020, doi: 10.1016/j.jallcom.2020.156172.

[14] S. Trolier-mckinstry, S. Zhang, A. J. Bell, and X. Tan, “High-Performance Piezoelectric Crystals , Ceramics , and Films,” no. February, pp. 1–27, 2018.

[15] C. Wang, Y. Wang, G. Zhang, C. Peng, and G. Yang, “on the electronic structure and thermoelectric properties of ZnO nanowires,” pp. 3771–3776, 2014, doi: 10.1039/c3cp54289k.

[16] K. Davis, R. Yarbrough, M. Froeschle, and J. White, “RSC Advances a sol – gel synthesis of solvent driven shape- controlled crystal growth †,” pp. 14638–14648, 2019, doi: 10.1039/c9ra02091h.

[17] A. Sáenz-Trevizo, P. Amézaga-Madrid, P. Pizá-Ruiz, W. Antúnez-Flores, and M. Miki-Yoshida, “Optical band gap estimation of ZnO nanorods,” Mater. Res., vol. 19, pp. 33–38, 2016, doi: 10.1590/1980-5373-MR-2015-0612.

[18] S. Haffad, G. Cicero, and M. Samah, “Structural and electronic properties of ZnO nanowires: A theoretical study,” Energy Procedia, vol. 10, pp. 128–137, 2011, doi: 10.1016/j.egypro.2011.10.165.

[19] J. B. Xia and X. W. Zhang, “Electronic structure of ZnO wurtzite quantum wires,” Eur. Phys. J. B, vol. 49, no. 4, pp. 415–420, 2006, doi: 10.1140/epjb/e2006-00093-1.

[20] P. Erhart, K. Albe, and A. Klein, “First-principles study of intrinsic point defects in ZnO : Role of band structure , volume relaxation , and finite-size effects,” Phys. Rev. B, pp. 1–9,

2006, doi: 10.1103/PhysRevB.73.205203.

[21] M. Usuda, N. Hamada, T. Kotani, and M. Van Schilfgaarde, “All-electron (formula presented) calculation based on the LAPW method: Application to wurtzite ZnO,” Phys. Rev. B - Condens. Matter Mater. Phys., vol. 66, no. 12, pp. 1–8, 2002, doi: 10.1103/PhysRevB.66.125101.

[22] P. K. Aspoukeh, A. A. Barzinjy, and S. M. Hamad, “Synthesis, properties and uses of ZnO nanorods: a mini review,” Int. Nano Lett., vol. 12, no. 2, pp. 153–168, 2022, doi: 10.1007/s40089-021-00349-7.

[23] M. F. L.V. Podrezova, S. Porro, V Cauda, “Comparison between ZnO nanowires grown by chemical vapor deposition and hydrothermal synthesis.” pp. 623–632, 2013.

[24] W. Y. Wu, C. C. Yeh, and J. M. Ting, “Effects of seed layer characteristics on the synthesis of ZnO nanowires,” J. Am. Ceram. Soc., vol. 92, no. 11, pp. 2718–2723, 2009, doi: 10.1111/j.1551-2916.2009.03022.x.

[25] R. Devaraj, K. Venkatachalam, K. Saravanakumar, P. M. Razad, and K. Mahalakshmi, “Role of hexamine: growth of multiarmed ZnO nanorods and evidence of merging due to lateral growth,” J. Mater. Sci. Mater. Electron., vol. 27, no. 11, pp. 12201–12208, 2016, doi: 10.1007/s10854-016-5375-7.

[26] S. Bagga, J. Akhtar, and S. Mishra, “Synthesis and applications of ZnO nanowire: A review,” AIP Conf. Proc., vol. 1989, no. July, 2018, doi: 10.1063/1.5047680.

[27] Y. Sun, G. M. Fuge, and M. N. R. Ashfold, “Growth mechanisms for ZnO nanorods formed by pulsed laser deposition,” Superlattices Microstruct., vol. 39, pp. 33–40, 2006, doi: 10.1016/j.spmi.2005.08.029.

[28] F. Paquin, J. Rivnay, A. Salleo, N. Stingelin, and C. Silva, “Multi-phase semicrystalline microstructures drive exciton dissociation in neat plastic semiconductors,” J. Mater. Chem. C, vol. 3, no. 207890, pp. 10715–10722, 2015, doi: 10.1039/b000000x.

[29] H. L. Cao, X. F. Qian, Q. Gong, W. M. Du, X. D. Ma, and Z. K. Zhu, “Shape- and size-

controlled synthesis of nanometre ZnO from a simple solution route at room temperature," Nanotechnology, vol. 17, no. 15, pp. 3632–3636, 2006, doi: 10.1088/0957-4484/17/15/002.

[30] B. Cheng and E. T. Samulski, "Hydrothermal synthesis of one-dimensional ZnO nanostructures with different aspect ratios," Chem. Commun., vol. 4, no. 8, pp. 986–987, 2004, doi: 10.1039/b316435g.

[31] S. Y. Li, P. Lin, C. Y. Lee, and T. Y. Tseng, "Field emission and photofluorescent characteristics of zinc oxide nanowires synthesized by a metal catalyzed vapor-liquid-solid process," J. Appl. Phys., vol. 95, no. 7, pp. 3711–3716, 2004, doi: 10.1063/1.1655685.

[32] P. Y. Dave, K. H. Patel, K. V. Chauhan, A. K. Chawla, and S. K. Rawal, "Examination of Zinc Oxide Films Prepared by Magnetron Sputtering," Procedia Technol., vol. 23, pp. 328–335, 2016, doi: 10.1016/j.protcy.2016.03.034.

[33] M. Arroyo-Hernández, R. Álvaro, S. Serrano, and J. L. Costa-Krämer, "Catalytic growth of ZnO nanostructures by r.f. magnetron sputtering," Nanoscale Res. Lett., vol. 6, pp. 1–6, 2011, doi: 10.1186/1556-276X-6-437.

[34] W. T. Chiou, W. Y. Wu, and J. M. Ting, "Growth of single crystal ZnO nanowires using sputter deposition," Diam. Relat. Mater., vol. 12, no. 10–11, pp. 1841–1844, 2003, doi: 10.1016/S0925-9635(03)00274-7.

[35] H. Wan and H. E. Ruda, "A study of the growth mechanism of CVD-grown ZnO nanowires," J. Mater. Sci. Mater. Electron., vol. 21, no. 10, pp. 1014–1019, 2010, doi: 10.1007/s10854-010-0118-7.

[36] P. C. Chang et al., "ZnO nanowires synthesized by vapor trapping CVD method," Chem. Mater., vol. 16, no. 24, pp. 5133–5137, 2004, doi: 10.1021/cm049182c.

[37] O. Lupan et al., "Synthesis and characterization of ZnO nanowires for nanosensor applications," Mater. Res. Bull., vol. 45, no. 8, pp. 1026–1032, 2010, doi: 10.1016/j.materresbull.2010.03.027.

[38] L. V. Podrezova, S. Porro, V. Cauda, M. Fontana, and G. Cicero, "Comparison between

ZnO nanowires grown by chemical vapor deposition and hydrothermal synthesis," Appl. Phys. A Mater. Sci. Process., vol. 113, no. 3, pp. 623–632, 2013, doi: 10.1007/s00339-013-7838-5.

[39] L. Lu, J. Chen, L. Li, and W. Wang, "Direct synthesis of vertically aligned ZnO nanowires on FTO substrates using a CVD method and the improvement of photovoltaic performance," Nanoscale Res. Lett., vol. 7, pp. 1–8, 2012, doi: 10.1186/1556-276X-7-293.

[40] S. Y. Li, C. Y. Lee, and T. Y. Tseng, "Copper-catalyzed ZnO nanowires on silicon (1 0 0) grown by vapor-liquid-solid process," J. Cryst. Growth, vol. 247, no. 3–4, pp. 357–362, 2003, doi: 10.1016/S0022-0248(02)01918-8.

[41] V. K. Sharma, B. K. Gupta, and G. D. Varma, "Optical and magnetic properties of (Zn,Mn)O nanostructures synthesized by CVD method," Cryst. Res. Technol., vol. 46, no. 5, pp. 523–528, 2011, doi: 10.1002/crat.201100029.

[42] A. b. Hartanto, X. Ning, Y. Nakata, and T. Okada, "Growth mechanism of ZnO nanorods from nanoparticles formed in a laser ablation plume," vol. 301, pp. 299–301, 2004, doi: 10.1007/s00339-003-2286-2.

[43] F. Ren, "Synthesis and microstructure of vertically aligned ZnO nanowires grown by high-pressure-assisted pulsed-laser deposition," pp. 6925–6932, 2008, doi: 10.1007/s10853-008-2988-0.

[44] S. Choopun, H. Tabata, and T. Kawai, "Self-assembly ZnO nanorods by pulsed laser deposition under argon atmosphere," J. Cryst. Growth, vol. 274, no. 1–2, pp. 167–172, 2005, doi: 10.1016/j.jcrysgro.2004.10.017.

[45] S. Kim, J. Lee, J. Kim, and Y. Heo, "Effects of Temperature , Target / Substrate Distance , and Background Pressure on Growth of ZnO Nanorods by Pulsed Laser Deposition," pp. 9020–9024, 2014, doi: 10.1166/jnn.2014.10062.

[46] Y. W. Heo et al., "UV photoresponse of single ZnO nanowires," Appl. Phys. A Mater. Sci. Process., vol. 80, no. 3, pp. 497–499, 2005, doi: 10.1007/s00339-004-3045-8.

[47] Y. W. Heo et al., “Site-specific growth of Zno nanorods using catalysis-driven molecular-beam epitaxy,” Appl. Phys. Lett., vol. 81, no. 16, pp. 3046–3048, 2002, doi: 10.1063/1.1512829.

[48] I. Isakov, M. Panfilova, M. J. L. Sourribes, and P. A. Warburton, “Growth of ZnO and ZnMgO nanowires by Au-catalysed molecular-beam epitaxy,” Phys. Status Solidi Curr. Top. Solid State Phys., vol. 10, no. 10, pp. 1308–1313, 2013, doi: 10.1002/pssc.201200940.

[49] B. Pandey, S. Ghosh, P. Srivastava, D. Kabiraj, T. Shripati, and N. P. Lalla, “Synthesis of nanodimensional ZnO and Ni-doped ZnO thin films by atom beam sputtering and study of their physical properties,” Phys. E Low-Dimensional Syst. Nanostructures, vol. 41, no. 7, pp. 1164–1168, 2009, doi: 10.1016/j.physe.2009.01.016.

[50] C. E. Iheomamere, C. L. Arnold, J. Summers, R. F. Reidy, A. A. Voevodin, and N. D. Shepherd, “Characterization of RF magnetron-sputtered a -BO x N y / ZnO MIS structures for transparent electronics,” J. Mater. Sci. Mater. Electron., vol. 33, no. 2, pp. 974–984, 2022, doi: 10.1007/s10854-021-07368-2.

[51] D. H. Kim et al., “Comparison of the optical properties of undoped and Ga-doped ZnO thin films deposited using RF magnetron sputtering at room temperature,” Opt. Commun., vol. 281, no. 8, pp. 2120–2125, 2008, doi: 10.1016/j.optcom.2007.12.015.

[52] G. Amin, M. H. Asif, A. Zainelabdin, S. Zaman, O. Nur, and M. Willander, “Influence of pH , Precursor Concentration , Growth Time , and Temperature on the Morphology of ZnO Nanostructures Grown by the Hydrothermal Method,” journel Nanomater., vol. 2011, 2011, doi: 10.1155/2011/269692.

[53] S. Karthika, T. K. Radhakrishnan, and P. Kalaichelvi, “A Review of Classical and Nonclassical Nucleation Theories,” Cryst. Growth Des., vol. 16, no. 11, pp. 6663–6681, 2016, doi: 10.1021/acs.cgd.6b00794.

[54] B. Ludi and M. Niederberger, “Zinc oxide nanoparticles: Chemical mechanisms and classical and non-classical crystallization,” Dalt. Trans., vol. 42, no. 35, pp. 12554–12568, 2013, doi: 10.1039/c3dt50610j.

[55] T. L. Sounart, J. Liu, J. A. Voigt, M. Huo, E. D. Spoerke, and B. McKenzie, “Secondary nucleation and growth of ZnO,” J. Am. Chem. Soc., vol. 129, no. 51, pp. 15786–15793, 2007, doi: 10.1021/ja071209g.

[56] Y. Tong et al., “Growth of ZnO nanostructures with different morphologies by using hydrothermal technique,” J. Phys. Chem. B, pp. 20263–20267, 2006.

[57] H. You and J. Fang, “Particle-mediated nucleation and growth of solution-synthesized metal nanocrystals: A new story beyond the LaMer curve,” Nano Today, vol. 11, no. 2, pp. 145–167, 2016, doi: 10.1016/j.nantod.2016.04.003.

[58] M. Yang, G. Pang, J. Li, L. Jiang, and S. Feng, “Preparation of ZnO nanowires in a neutral aqueous system: Concentration effect on the orientation attachment process,” Eur. J. Inorg. Chem., no. 19, pp. 3818–3822, 2006, doi: 10.1002/ejic.200600369.

[59] R. Devaraj, K. Venkatachalam, and P. M. Razad, “Role of seed layer: lattice orientation attachment and structural stabilization on the lateral growth of ZnO nanorods,” J. Mater. Sci. Mater. Electron., vol. 27, no. 4, pp. 4011–4018, 2016, doi: 10.1007/s10854-015-4255-x.

[60] B. Fan, Y. Zhang, R. Yan, and J. Fan, “Multistage growth of monocrystalline ZnO nanowires and twin-nanorods: Oriented attachment and role of the spontaneous polarization force,” CrystEngComm, vol. 18, no. 34, pp. 6492–6501, 2016, doi: 10.1039/c6ce01337f.

[61] J. Anwar and D. Zahn, “Uncovering molecular processes in crystal nucleation and growth by using molecular simulation,” Angew. Chemie - Int. Ed., vol. 50, no. 9, pp. 1996–2013, 2011, doi: 10.1002/anie.201000463.

[62] E. Jeong et al., “Nonconventional nucleation and growth of Au nanoparticles with improved adhesion on oxygen-excessive oxide surfaces,” Appl. Surf. Sci., vol. 553, p. 149385, 2021, doi: 10.1016/j.apsusc.2021.149385.

[63] W. A. Saidi, “Density functional theory study of nucleation and growth of pt nanoparticles on MoS2(001) surface,” Cryst. Growth Des., vol. 15, no. 2, pp. 642–652, 2015, doi: 10.1021/cg5013395.

[64] Y. Wang, B. Xiang, H. Q. Yang, and C. W. Hu, “Density Functional Theory Study on the Nucleation and Growth of Ptn Clusters on Al2O3(001) Surface,” ACS Omega, vol. 2, no. 7. pp. 3250–3259, 2017. doi: 10.1021/acsomega.7b00342.

[65] M. K. Niranjan, T. Karthik, S. Asthana, J. Pan, and U. V. Waghmare, “Theoretical and experimental investigation of Raman modes, ferroelectric and dielectric properties of relaxor Na0.5Bi0.5TiO 3,” J. Appl. Phys., vol. 113, no. 19, pp. 0–7, 2013, doi: 10.1063/1.4804940.

[66] N. Provatas, Phase-Field Methods in Materials Science and Engineering. 2010.

[67] P. W. Voorhees, “Phase field modeling of grain growth : effect of boundary thickness , triple junctions , misorientation , and anisotropy,” J. Mater Sci, pp. 2206–2217, 2009, doi: 10.1007/s10853-008-3196-7.

[68] Y. Wang, P. C. Mcintyre, and W. Cai, “Phase Field Model for Morphological Transition in Nanowire Vapor-Liquid-Solid Growth,” Cryst. Growth Des., 2017, doi: 10.1021/acs.cgd.7b00197.

[69] N. Wang, M. Upmanyu, and A. Karma, “PHYSICAL REVIEW MATERIALS 2 , 033402 (2018) Phase-field model of vapor-liquid-solid nanowire growth,” Phys. Rev. Mater., vol. 2, no. 3, p. 33402, 2018, doi: 10.1103/PhysRevMaterials.2.033402.

[70] P. Wu and Y. Liang, “Lattice Phase Field Model for Nanomaterials,” Mater. MDPI, 2021.

[71] A. Roy, E. S. Nani, A. Lahiri, and M. P. Gururajan, “Phase field modelling of interfacial anisotropy driven faceting of precipitates,” pp. 1–25.

[72] T. A. A and F. H, “An extended Cahn ± Hilliard model for interfaces with cubic anisotropy,” Philosphical Mag. A, 2001.

[73] E. S. Nani and M. P. Gururajan, “On the incorporation of cubic and hexagonal interfacial energy anisotropy in phase field models using higher order tensor terms,” pp. 1–14, 2022.

[74] D. Segets, L. M. Tomalino, J. Gradl, and W. Peukert, “Real-time monitoring of the nucleation and growth of zno nanoparticles using an optical hyper-rayleigh scattering method,” J. Phys. Chem. C, vol. 113, no. 28, pp. 11995–12001, 2009, doi:

10.1021/jp9009965.

[75] I. Whittall, A. M. Mcdonagh, M. G. Humphrey, and M. Samoc, “Organometallic Complexes in Nonlinear Optics I :,” Adv. Organomet. Chem., vol. 42, pp. 291–362, 1998.

[76] W. Yoshimune, A. Kuwaki, T. Kusano, T. Matsunaga, and H. Nakamura, “In Situ Small-Angle X-ray Scattering Studies on the Growth Mechanism of Anisotropic Platinum Nanoparticles,” ACS Omega, vol. 6, no. 16, pp. 10866–10874, 2021, doi: 10.1021/acsomega.1c00608.

[77] S. Sokolov et al., “Nucleation and Growth of Gold Nanoparticles Studied via in situ Small,” ACS Nano, vol. 4, no. 2, 2010.

[78] M. S. León-Velázquez, R. Irizarry, and M. E. Castro-Rosario, “Nucleation and growth of silver sulfide nanoparticles,” J. Phys. Chem. C, vol. 114, no. 13, pp. 5839–5849, 2010, doi: 10.1021/jp911238a.

[79] E. V. Shevchenko et al., “Study of nucleation and growth in the organometallic synthesis of magnetic alloy nanocrystals: The role of nucleation rate in size control of CoPt3 nanocrystals,” J. Am. Chem. Soc., vol. 125, no. 30, pp. 9090–9101, 2003, doi: 10.1021/ja029937l.

[80] J. W. L. Eccles, U. Bangert, M. Bromfield, P. Christian, A. J. Harvey, and P. Thomas, “UV-Vis plasmon studies of metal nanoparticles,” J. Phys. Conf. Ser., vol. 241, p. 012090, 2010, doi: 10.1088/1742-6596/241/1/012090.

[81] P. A. C. Ã, R. Wang, and R. Sharma, “Ultramicroscopy In situ environmental TEM studies of dynamic changes in cerium-based oxides nanoparticles during redox processes,” vol. 108, pp. 1432–1440, 2008, doi: 10.1016/j.ultramic.2008.05.015.

[82] B. Lee et al., “Statistical Characterization of the Morphologies of Nanoparticles through Machine Learning Based Electron Microscopy Image Analysis,” ACS Nano, vol. 14, no. 12, pp. 17125–17133, 2020, doi: 10.1021/acsnano.0c06809.

[83] W. Nur, A. Mazli, and M. A. Ahmad, “Nucleation,” intechopen, pp. 1–10.

[84] G. Coquerel, “Crystallization of molecular systems from solution: Phase diagrams, supersaturation and other basic concepts,” Chem. Soc. Rev., vol. 43, no. 7, pp. 2286–2300, 2014, doi: 10.1039/c3cs60359h.

[85] J. Lee, J. Yang, S. G. Kwon, and T. Hyeon, “Nonclassical nucleation and growth of inorganic nanoparticles,” Nat. Rev. Mater., vol. 1, no. 8, pp. 1–17, 2016, doi: 10.1038/natrevmats.2016.34.

[86] “Classical and Non-Classical Nucleation-5.pdf.”

[87] D. Gebauer and H. Cölfen, Prenucleation clusters and non-classical nucleation, vol. 6, no. 6. 2011. doi: 10.1016/j.nantod.2011.10.005.

[88] D. Gebauer, P. Raiteri, J. D. Gale, and H. Cölfen, “On classical and non-classical views on nucleation,” Am. J. Sci., vol. 318, no. 9, pp. 969–988, 2018, doi: 10.2475/09.2018.05.

[89] L. Gránásy et al., “Phase field theory of crystal nucleation and polycrystalline growth: A review,” J. Mater. Res., vol. 21, no. 2, pp. 309–319, 2006, doi: 10.1557/jmr.2006.0011.

[90] and S. M. Nguyen T. K. Thanh, N. Maclean, “Mechanism of nucleation and rowth of nanoparticles in solution.” pp. 7610–7628, 2014. doi: https://doi.org/10.1021/cr400544s.

[91] M. Herbst and E. Hofmann, “Nucleation and Growth Kinetics of ZnO Nanoparticles Studied by in Situ Micro fl uidic SAXS/WAXS/UV − Vis Experiments,” ACS, 2019, doi: 10.1021/acs.langmuir.9b01149.

[92] P. Montero De Hijes, J. R. Espinosa, E. Sanz, and C. Vega, “Interfacial free energy of a liquid-solid interface: Its change with curvature,” J. Chem. Phys., vol. 151, no. 14, 2019, doi: 10.1063/1.5121026.

[93] J. F. Galloway, J. Park, K. H. Lee, D. Wirtz, and P. C. Searson, “Exploiting Nucleation and Growth in the Synthesis and Electrical Passivation of CdSe Quantum Dots Exploiting Nucleation and Growth in the Synthesis and Electrical Passivation of CdSe Quantum Dots,” no. February 2015, 2009, doi: 10.1166/sam.2009.1014.

[94] V. Gerbreders et al., “Hydrothermal synthesis of ZnO nanostructures with controllable

morphology change," CrystEngComm, vol. 22, no. 8, pp. 1346–1358, 2020, doi: 10.1039/c9ce01556f.

[95] Z. Fang, Y. Wang, D. Xu, Y. Tan, and X. Liu, "Blue luminescent center in ZnO films deposited on silicon substrates," Opt. Mater. (Amst)., vol. 26, no. 3, pp. 239–242, 2004, doi: 10.1016/j.optmat.2003.11.027.

[96] A. F. Abdulrahman, S. M. Ahmed, and N. M. Ahmed, "Enhancement of ZnO Nanorods Properties Using Modified Chemical Bath Deposition Method : E ff ect of Precursor Concentration," MDPI Cryst., 2020.

[97] J. Tian, J. Hu, S. Li, and F. Zhang, "Improved seedless hydrothermal synthesis of dense and ultralong ZnO nanowires My IOPscience Improved seedless hydrothermal synthesis of dense and ultralong ZnO nanowires This article has been downloaded from IOPscience . Please scroll down to see the full," no. June, 2011, doi: 10.1088/0957-4484/22/24/245601.

[98] N. Rana, A. K. Gathania, and S. Chand, "Structural and Optical Properties of ZnO Nanoparticles," Opt. InfoBase Conf. Pap., vol. 539, pp. 174–178, 2014.

[99] W. Wu, W. Kung, and J. Ting, "Effect of pH Values on the Morphology of Zinc Oxide Nanostructuresand their Photoluminescence Spectra," vol. 703, no. 27660, pp. 699–703, 2011, doi: 10.1111/j.1551-2916.2010.04146.x.

[100] A. K. Ã. Singh, V. Viswanath, and V. C. Janu, "Synthesis , effect of capping agents , structural , optical and photoluminescence properties of ZnO nanoparticles," J. Lumin., vol. 129, pp. 874–878, 2009, doi: 10.1016/j.jlumin.2009.03.027.

[101] H.-S. K. Kwong-Lung Ching*, Guijun Li, Yeuk-Lung Ho, "The Role of Polarity and Surface Energy in the Growth Mechanism of ZnO from Nanorods to Nanotubes," R. Soc. Chem., 2015, doi: 10.1039/C5CE02164B.

[102] A. G. Vega-Poot, G. Rodríguez-Gattorno, O. E. Soberanis-Domínguez, R. T. Patiño-Díaz, M. Espinosa-Pesqueira, and G. Oskam, "The nucleation kinetics of ZnO nanoparticles from ZnCl2 in ethanol solutions," Nanoscale, vol. 2, no. 12, pp. 2710–2717, 2010, doi: 10.1039/c0nr00439a.

[103] S. J. Ruuth, “Implicit-explicit methods for reaction-diffusion problems,” J. Math. Biol., vol. 34, no. 3, pp. 148–176, 1995.

[104] A. V. Shapovalov and V. V. Obukhov, “Some aspects of nonlinearity and self-organization in biosystems on examples of localized excitations in the DNA molecule and generalized fisher-KPP model,” Symmetry (Basel)., vol. 10, no. 3, 2018, doi: 10.3390/SYM10030053.

[105] Ninla Elmawati Falabiba, “A Comparison Study of Chebyshev Spectral Collocation Based Methods for Solving Nonlinear Second Order Evolution Equations,” 2019.

[106] C. Lizandara-Pueyo, M. W. E. Van Den Berg, A. De Toni, T. Goes, and S. Polarz, “Nucleation and growth of ZnO in organic solvents - An in situ study,” J. Am. Chem. Soc., vol. 130, no. 49, pp. 16601–16610, 2008, doi: 10.1021/ja804071h.

[107] A. Redinger and S. Siebentritt, “Optical Properties and Electronic Structure of Amorphous Germanium,” phys. stat. sol, vol. 627, pp. 363–386, 1966, doi: 10.1002/9781118437865.ch16.

[108] J. Tauc, “OPTICAL PROPERTIES AND ELECTRONIC STRUCTURE OF AMORPHOUS Ge AND Si,” Mater. Res. Bull., vol. 34, no. 2, pp. 78–86, 1968.

[109] A. Escobedo-Morales, I. I. Ruiz-López, M. de L. Ruiz-Peralta, L. Tepech-Carrillo, M. Sánchez-Cantú, and J. E. Moreno-Orea, “Automated method for the determination of the band gap energy of pure and mixed powder samples using diffuse reflectance spectroscopy,” Heliyon, vol. 5, no. 4, pp. 1–19, 2019, doi: 10.1016/j.heliyon.2019.e01505.

[110] S. Repp and E. Erdem, “Controlling the exciton energy of zinc oxide (ZnO) quantum dots by changing the confinement conditions,” Spectrochim. Acta - Part A Mol. Biomol. Spectrosc., vol. 152, pp. 637–644, 2016, doi: 10.1016/j.saa.2015.01.110.

[111] D. V. andSusana F. de Á. Fernando Rodríguez-Mas , Juan Carlos Ferrer, José Luis Alonso, “A Comparative Study of Theoretical Methods to Estimate Semiconductor Nanoparticles’ Size,” Cryst. MDPI, 2020, doi: 10.3390/cryst10030226.

[112] S. Meng, A. Zhang, Z. Guo, and Q. Wang, “Phase-field-lattice Boltzmann simulation of

dendrite motion using an immersed boundary method," Comput. Mater. Sci., vol. 184, no. June, p. 109784, 2020, doi: 10.1016/j.commatsci.2020.109784.

[113] S. Sakane et al., "Multi-GPUs parallel computation of dendrite growth in forced convection using the phase-field-lattice Boltzmann model," J. Cryst. Growth, vol. 474, no. November 2016, pp. 154–159, 2017, doi: 10.1016/j.jcrysgro.2016.11.103.

[114] X. Yang and J. Zhao, "Efficient linear schemes for the nonlocal Cahn–Hilliard equation of phase field models," Comput. Phys. Commun., vol. 235, pp. 234–245, 2019, doi: 10.1016/j.cpc.2018.08.012.

[115] S. B. Biner, Programming Phase-Field Modeling. Springer, 2017. doi: 10.1007/978-3-319-41196-5.

[116] T. Long, S. Yin, K. Takabatake, P. Zhnag, and T. Sato, "Synthesis and characterization of zno nanorods and nanodisks from zinc chloride aqueous solution," Nanoscale Res. Lett., vol. 4, no. 3, pp. 247–253, 2009, doi: 10.1007/s11671-008-9233-2.

[117] M. M. J. van Rijt et al., "Counter-ion influence on the mechanism of HMTA-mediated ZnO formation," CrystEngComm, vol. 22, no. 35, pp. 5854–5861, 2020, doi: 10.1039/d0ce00847h.

[118] N. Babayevska et al., "ZnO size and shape effect on antibacterial activity and cytotoxicity profile," Sci. Rep., vol. 12, no. 1, pp. 1–13, 2022, doi: 10.1038/s41598-022-12134-3.

[119] A. Panwar and K. L. Yadav, "A novel one-pot synthesis of hierarchical europium doped ZnO nanoflowers," Mater. Lett., vol. 142, no. March, pp. 30–34, 2015, doi: 10.1016/j.matlet.2014.11.143.

[120] J. Li, D. Yang, and X. Zhu, "Effects of aging time and annealing temperature on structural and optical properties of sol-gel ZnO thin films," AIP Adv., vol. 7, no. 6, pp. 1–7, 2017, doi: 10.1063/1.4985753.

[121] C. Chevalier-César, M. Capochichi-Gnambodoe, and Y. Leprince-Wang, "Growth mechanism studies of ZnO nanowire arrays via hydrothermal method," Appl. Phys. A

Mater. Sci. Process., vol. 115, no. 3, pp. 953–960, 2014, doi: 10.1007/s00339-013-7908-8.

[122] S. Thota, T. Dutta, and J. Kumar, “On the sol-gel synthesis and thermal, structural, and magnetic studies of transition metal (Ni, Co, Mn) containing ZnO powders,” J. Phys. Condens. Matter, vol. 18, no. 8, pp. 2473–2486, 2006, doi: 10.1088/0953-8984/18/8/012.

[123] Q. Li, V. Kumar, Y. Li, H. Zhang, T. J. Marks, and R. P. H. Chang, “Fabrication of ZnO nanorods and nanotubes in aqueous solutions,” Chem. Mater., vol. 17, no. 5, pp. 1001–1006, 2005, doi: 10.1021/cm048144q.

[124] V. Strano et al., “Double role of HMTA in ZnO nanorods grown by chemical bath deposition,” J. Phys. Chem. C, vol. 118, no. 48, pp. 28189–28195, 2014, doi: 10.1021/jp507496a.

[125] R. Wahab, Y. S. Kim, K. Lee, and H. S. Shin, “Fabrication and growth mechanism of hexagonal zinc oxide nanorods via solution process,” J. Mater. Sci., vol. 45, no. 11, pp. 2967–2973, 2010, doi: 10.1007/s10853-010-4294-x.

[126] S. Del Gobbo, J. Poolwong, and V. D. Elia, “In-Suspension Growth of ZnO Nanorods with Tunable Length and Diameter Using Polymorphic Seeds,” 2019, doi: 10.1021/acs.cgd.9b01226.

[127] R. Chaudhari, D. Landge, and C. J. Bhongale, “A new insight into the adsorption-dissolution growth mechanism of zinc oxide hollow hexagonal nanotowers,” RSC Advances, vol. 9, no. 36. pp. 20728–20732, 2019. doi: 10.1039/c9ra03499d.

[128] M. Guo, P. Diao, X. Wang, and S. Cai, “The effect of hydrothermal growth temperature on preparation and photoelectrochemical performance of ZnO nanorod array films,” J. Solid State Chem., vol. 178, no. 10, pp. 3210–3215, 2005, doi: 10.1016/j.jssc.2005.07.013.

[129] H. O. W. To, S. An, and O. Business, “Absorption of below-bandgap light in semiconductors,” 2018, doi: 10.1155/2018/8607247.

[130] J. H. Tian et al., “Improved seedless hydrothermal synthesis of dense and ultralong ZnO nanowires,” Nanotechnology, vol. 22, no. 24, 2011, doi: 10.1088/0957-4484/22/24/245601.

[131] Z. Han, S. Li, J. Chu, and Y. Chen, “Controlled growth of well-aligned ZnO nanowire arrays using the improved hydrothermal method,” J. Semicond., vol. 34, no. 6, 2013, doi: 10.1088/1674-4926/34/6/063002.

[132] H. F. Wilson, C. Tang, and A. S. Barnard, “Morphology of zinc oxide nanoparticles and nanowires: Role of surface and edge energies,” J. Phys. Chem. C, vol. 120, no. 17, pp. 9498–9505, 2016, doi: 10.1021/acs.jpcc.6b01479.

[133] T. Demes et al., “Mechanisms involved in the hydrothermal growth of ultra-thin and high aspect ratio ZnO nanowires,” Appl. Surf. Sci., vol. 410, pp. 423–431, 2017, doi: 10.1016/j.apsusc.2017.03.086.

[134] R. P. Chauhan, D. Gehlawat, and A. Kaur, “Ion beam fluence induced variation in optical band-gap of ZnO nanowires,” J. Exp. Nanosci., vol. 9, no. 8, pp. 871–876, 2014, doi: 10.1080/17458080.2012.736639.

[135] C. Y. Chen, M. W. Chen, J. J. Ke, C. A. Lin, J. R. D. Retamal, and J. H. He, “Surface effects on optical and electrical properties of ZnO nanostructures,” Pure Appl. Chem., vol. 82, no. 11, pp. 2055–2073, 2010, doi: 10.1351/PAC-CON-09-12-05.

[136] W. Pong and C. Chen, “Anomalous blueshift in emission spectra of ZnO nanorods with sizes beyond quantum confinement regime beyond quantum confinement regime,” Appl. Phys. Lett., vol. 241905, no. October 2005, pp. 98–101, 2006, doi: 10.1063/1.2211047.

[137] Y. H. Yang, X. Y. Chen, Y. Feng, and G. W. Yang, “Physical Mechanism of Blue-Shift of UV Luminescence of a Single Pencil-Like,” Nano Lett., vol. 7, pp. 3879–3883, 2007, doi: 10.1021/nl071849h.

[138] E. Tosi, D. Comedi, and G. Zampieri, “Applied Surface Science Band bending at the ZnO (0001) -Zn surface produced by electropositive , electronegative and atmospheric adsorbates,” Appl. Surf. Sci., vol. 495, no. June, p. 143592, 2019, doi: 10.1016/j.apsusc.2019.143592.

[139] Y. Y. Tay, T. T. Tan, M. H. Liang, F. Boey, and S. Li, “Specific defects, surface band bending and characteristic green emissions of ZnO,” Phys. Chem. Chem. Phys., vol. 12, no.

23, pp. 6008–6013, 2010, doi: 10.1039/b926427b.

[140] M. Caglar, S. Ilican, Y. Caglar, and F. Yakuphanoglu, “Electrical conductivity and optical properties of ZnO nanostructured thin film,” Appl. Surf. Sci., vol. 255, no. 8, pp. 4491–4496, 2009, doi: 10.1016/j.apsusc.2008.11.055.

[141] M. Kadota, T. Miura, and M. Minakata, “Piezoelectric and optical properties of ZnO films deposited by an electron-cyclotron-resonance sputtering system,” J. Cryst. Growth, vol. 237–239, no. 1 4 I, pp. 523–527, 2002, doi: 10.1016/S0022-0248(01)01958-3.

[142] M. Shim and P. Guyot-Sionnest, “n-Type colloidal semiconductor nanocrystals,” Nature, vol. 407, no. 6807, pp. 981–983, 2000, doi: 10.1038/35039577.

[143] D. C. Look, C. Coşkun, B. Claflin, and G. C. Farlow, “Electrical and optical properties of defects and impurities in ZnO,” Phys. B Condens. Matter, vol. 340–342, pp. 32–38, 2003, doi: 10.1016/j.physb.2003.09.188.

[144] P. Sharma, S. K. Tiwari, and P. B. Barman, “Abnormal red shift in photoluminescence emission of ZnO nanowires,” J. Lumin., vol. 251, no. August, p. 119231, 2022, doi: 10.1016/j.jlumin.2022.119231.

[145] J. B. Coulter and D. P. Birnie, “Assessing Tauc Plot Slope Quantification: ZnO Thin Films as a Model System,” Phys. Status Solidi Basic Res., vol. 255, no. 3, pp. 1–7, 2018, doi: 10.1002/pssb.201700393.

[146] A. Janotti and C. G. Van De Walle, “Oxygen vacancies in ZnO,” Appl. Phys. Lett., vol. 87, no. 12, pp. 1–3, 2005, doi: 10.1063/1.2053360.

[147] A. Samavati et al., “Influence of ZnO nanostructure configuration on tailoring the optical bandgap: Theory and experiment,” Materials Science and Engineering B: Solid-State Materials for Advanced Technology, vol. 263. 2021. doi: 10.1016/j.mseb.2020.114811.

[148] Z. Zhang and J. T. Yates, “Band bending in semiconductors: Chemical and physical consequences at surfaces and interfaces,” Chem. Rev., vol. 112, no. 10, pp. 5520–5551, 2012, doi: 10.1021/cr3000626.

[149] C. Y. Chen et al., “Probing surface band bending of surface-engineered metal oxide nanowires,” ACS Nano, vol. 6, no. 11, pp. 9366–9372, 2012, doi: 10.1021/nn205097e.

[150] Q. Zhang, C. S. Dandeneau, X. Zhou, and C. Cao, “ZnO nanostructures for dye-sensitized solar cells,” Adv. Mater., vol. 21, no. 41, pp. 4087–4108, 2009, doi: 10.1002/adma.200803827.

[151] M. Sakar, S. Balakumar, P. Saravanan, and S. Bharathkumar, “Compliments of confinements: Substitution and dimension induced magnetic origin and band-bending mediated photocatalytic enhancements in Bi1-xDyxFeO3 particulate and fiber nanostructures,” Nanoscale, vol. 7, no. 24, pp. 10667–10679, 2015, doi: 10.1039/c5nr01079a.

[152] N. Kondal and S. K. Tiwari, “Origin of polychromatic emission and defect distribution within annealed ZnO nanoparticles,” Mater. Res. Bull., vol. 88, pp. 156–165, 2017, doi: 10.1016/j.materresbull.2016.12.033.

[153] S.-L. Zhang, Raman Spectroscopy and its Application in Nanostructures Description of the cover. 2012.

[154] A. B. Djurišić and Y. H. Leung, “Optical properties of ZnO nanostructures,” Small, vol. 2, no. 8–9, pp. 944–961, 2006, doi: 10.1002/smll.200600134.

[155] X. Zhang, Y. Liu, and S. Chen, “A novel method for measuring distribution of orientation of one-dimensional ZnO using resonance Raman spectroscopy,” J. Raman Spectrosc., vol. 36, no. 12, pp. 1101–1105, 2005, doi: 10.1002/jrs.1413.

[156] Y. Gao and P. Yin, “Origin of asymmetric broadening of Raman peak profiles in Si nanocrystals,” Sci. Rep., vol. 7, no. 4, pp. 7–10, 2017, doi: 10.1038/srep43602.

[157] K. H. Khoo, A. T. Zayak, H. Kwak, and J. R. Chelikowsky, “First-principles study of confinement effects on the raman spectra of Si nanocrystals,” Phys. Rev. Lett., vol. 105, no. 11, pp. 1–4, 2010, doi: 10.1103/PhysRevLett.105.115504.

[158] S. Sahoo, G. L. Sharma, and R. S. Katiyar, “Raman spectroscopy to probe residual stress in

ZnO nanowire," J. Raman Spectrosc., vol. 43, no. 1, pp. 72–75, 2012, doi: 10.1002/jrs.3004.

[159] F. Güell et al., "Raman and photoluminescence properties of ZnO nanowires grown by a catalyst-free vapor-transport process using ZnO nanoparticle seeds," Phys. Status Solidi Basic Res., vol. 253, no. 5, pp. 883–888, 2016, doi: 10.1002/pssb.201552651.

[160] I. Calizo et al., "Micro-Raman spectroscopic characterization of ZnO quantum dots, nanocrystals and nanowires," Quantum Dots, Part. Nanoclusters IV, vol. 6481, p. 64810N, 2007, doi: 10.1117/12.713648.

[161] S. K. Tripathi, M. Rani, and N. Singh, "ZnO:Ag and TZO:Ag plasmonic nanocomposite for enhanced dye sensitized solar cell performance," Electrochim. Acta, vol. 167, pp. 179–186, 2015, doi: 10.1016/j.electacta.2015.02.245.